Unraveling the coupled ocean-atmosphere system in the Indian Ocean using paired $\delta^{18}O$ and Sr/Ca records from a coral core originating from Cocos (Keeling) Island

Name	Malou ten Have
Student number	3471802
Master	Earth, Life and Climate
Supervisors	Prof. Gert-Jan Reichart and Dr. Rick Hennekam
Date	12 August, 2015
University	Utrecht University
Institution	NIOZ Royal Netherlands Institute for Sea Research

Abstract

This thesis researches the coupling of the ocean and atmosphere systems in the eastern Indian Ocean at the key location of Cocos (Keeling) Island, by studying the link between SST's, atmospheric convection, precipitation patterns, and cyclones. Which known ocean-atmosphere systems influence the climate around Cocos (Keeling) island and which other climate forcing factors are active in this region? The study uses $\delta^{18}O$ and Sr/Ca isotopes from a continuous coral core (Darwin Long) to reconstruct past SST and $\delta^{18}O_{SW}$ for the time period 1871 to 2009 AD. Spectral analysis is used to research periodicities of dominant cycles.

The data shows that climate variability at Cocos (Keeling) island is mainly influenced by annual seasonal variability. Also the eleven year sunspot cycle is thought to be of major influence at this site. The coupled ocean-atmosphere systems ENSO and IOD seem to be of minor influence in this region, but are possibly expressed during short events. There might also be a PDO signal present in the data records, but this should be studied in further research. Furthermore, there are four very distinct events present in our $\delta^{18}O$ and Sr/Ca records indicating SST cooling of 2-4°C, occurring around the years 1883, 1910-1915, 1946 and 1965-1970 AD. The cause of these events are different, but mainly related to minima in solar activity and possible ENSO and/or IOD influences. The 1883 event could be caused by the volcanic eruption of the Krakatoa. Finally, SST's gradually increase from around 1975 to around 2000 AD. However, a similar shift in influences of different ocean-atmosphere systems found around the Chagos Archipelago due to crossing of a SST threshold value, is not recognized in the Cocos (Keeling) region.

Key words: Recent palaeoclimate; corals; Sr/Ca; $\delta^{18}O$; ocean-atmosphere systems; Indian Ocean; Cocos (Keeling) island

Universiteit Utrecht

NIOZ

Table of Contents

Chapter 1 Introduction

The Indian Ocean is one of the major ocean basins in the world, covering approximately 20 percent of Earth's water surface. Nevertheless, this major basin has barely been studied relative to other large oceanic basins. This is exemplified by the relatively late discovery of its internal mode of coupled ocean-atmospheric variability, i.e. the Indian Ocean Dipole (IOD; Saji et al., 1999). The Indian Ocean is bordered by the African, Eurasian, and Australian continents, being potentially thus an important component of the global weather and climate system. For instance, the Indian Ocean triggers one of the most important coupled ocean-atmosphere phenomena, the Asian monsoonal system, which influences a vast amount of the global population. The Fifth Assessment Report of the Intergovernmental Panel on Climate Change states that the current global warming, and associated climate change, has an extensive effect on climate components in both atmosphere and ocean, such as sea surface temperatures (SST's) and cyclones (IPCC, 2013). To research the impact of climate change, comprehensive knowledge about the current climate system is needed. However, instrumental measurements of the Indian Ocean – and especially its eastern part – are scarce and generally limited to the last few decades. Hence, in order to fully comprehend the influence of the Indian Ocean on climatic conditions in the surrounding landmasses, it is vital to extend our instrumental records using high-resolution proxy records.

For this reason, this thesis studies the coupling of the ocean and atmosphere systems in the eastern Indian Ocean, at the key location of Cocos (Keeling) Island (Figure 1.1). Our aim is to study the link between SST's, atmospheric convection, precipitation patterns, and cyclones in the eastern Indian Ocean. The main research question of the thesis is: which known ocean-atmosphere systems influence the climate around Cocos (Keeling) island? Additionally, we want to know which other climate forcing factors are active in this region during the time period of 1871-2009. There are two prominent coupled ocean-atmosphere systems known to cause inter-annual variability of the climate in the Indian Ocean, the El Niño Southern Oscillation (ENSO) and the Indian Ocean Dipole (IOD). However, it is uncertain to what degree these two ocean-atmosphere phenomena influence the region bordering the Indian Ocean and if and how these systems are coupled. Cocos (Keeling) island is a vital region to study the ocean-atmosphere linkage, because this is an area with strong atmospheric convection, residing in the pathway where most of the Pacific water (~75 percent) enters the Indian Ocean through the Indonesian Throughflow (ITF; Sebille et al., 2014). Therefore, this area is not only atmospherically linked to processes originating from the Pacific Ocean (ENSO) but also tightly linked via an oceanic "bridge" through the ITF. This is thus a key area to study the coupling of oceanic and atmospheric conditions, potentially influenced by both IOD and ENSO.

High-resolution coral-based studies from the Chagos Archipelago (Pfeiffer et al., 2006, Pfeiffer et al., 2009, Tim et al., 2005), roughly 2000 kilometers west to Cocos (Keeling) island and south from the Maladives, indicated that temporal variations in precipitation were associated with shifts and variations in the ITCZ, showing alternations of relatively wet and dry periods lasting around 15-20 years. However, since around 1970 variations are dominated by inter-annual variations coupled to ENSO. This shift is thought to be caused by Indian Ocean warming, where SST comes near a critical threshold of 28.5°C. At this threshold the lower atmosphere is charged with moist static energy before deep convection reaches the tropopause (Graham & Barnett, 1987; Sud et al., 1999; Zhang, 1993). Small variations in SST can have large impact on moisture availability and tropical convection (Zhang, 1993). Consequently, after 1970 small variations in SST (0.5-1°C) induced by El Niño may raise SST's above this threshold and induce positive rainfall anomalies. It is interesting whether these relationships and change in forcing can also be recognized at Cocos (Keeling) island, and the eastern Indian Ocean as a whole. However, at present, there are principally no eastern Indian Ocean counterparts of the Chagos coral records, and the many other western Indian Ocean coral records (e.g. Madagascar, Rodrigues, La Reunion, Seychelles, Mayotte, and Mauritius). This study aims to fill

this void by the use of a highly resolved (bi-monthly resolution) coral record from Cocos (Keeling) Island. The ocean-atmosphere relationship is studied using a paired Sr/Ca-$\delta^{18}O$ approach. The Strontium/Calcium ratio (Sr/Ca) is a robust SST proxy for coral records, which is thought to be not influenced by other climate variables (Alibert & McCulloch, 1997; Beck et al., 1992; Corrège, 2006; Moreau et al. 2015; Nurhati et al., 2009). The $^{18}O/^{16}O$ ratio ($\delta^{18}O$) record is both influenced by SST, sea surface salinity (SSS) and the hydrological balance (the relative proportion between evaporation and precipitation) (McConnaughey, 1989; Zinke et al., 2004). A paired Sr/Ca-$\delta^{18}O$ approach can thus be used to calculate the $\delta^{18}O$ value of the surrounding seawater ($\delta^{18}O_{SW}$), which is possibly linked to SSS and precipitation/evaporation (cyclone activity) in the region.

A continuous coral core (Darwin Long) was drilled from a *Porites* spp. coral colony near Cocos (Keeling) island, -12.087N/96.875E (see Figure 1.1), dating back from 2009 AD to 1809 AD. During the WOTRO-EKP project in 2011 a Sr/Ca record was reconstructed from the whole core. This study uses the same coral samples to construct a high resolution (bimonthly-monthly) $\delta^{18}O$ record from 1871 to 2009 AD. The records of Sr/Ca, $\delta^{18}O$ and $\delta^{18}O_{SW}$ are studied with respect to changes in metadata records such as SST, precipitation, salinity and IOD and ENSO variabilities. Relationships are studied by researching correlations between datasets and spectral analysis is carried out on the reconstructed SST, $\delta^{18}O$ and $\delta^{18}O_{SW}$ records to observe dominant periodicities. Furthermore, known extreme cyclone events are tried to link to the climatic proxy records and metadata records to study if these events are triggered by a coupled ocean-atmosphere system. According to Beck et al. (1992) heavy rainfall events can cause short-term depletions of $\delta^{18}O$ in the surface ocean waters and these events can cause deviations from the observed relation between Sr/Ca and $\delta^{18}O$. Also we briefly look at the $\delta^{13}C$ data record and the spectral green to blue (G/B) ratio recovered from Spectral Luminescence Scanning (SLS) to see whether the same patterns and frequencies can be distinguished.

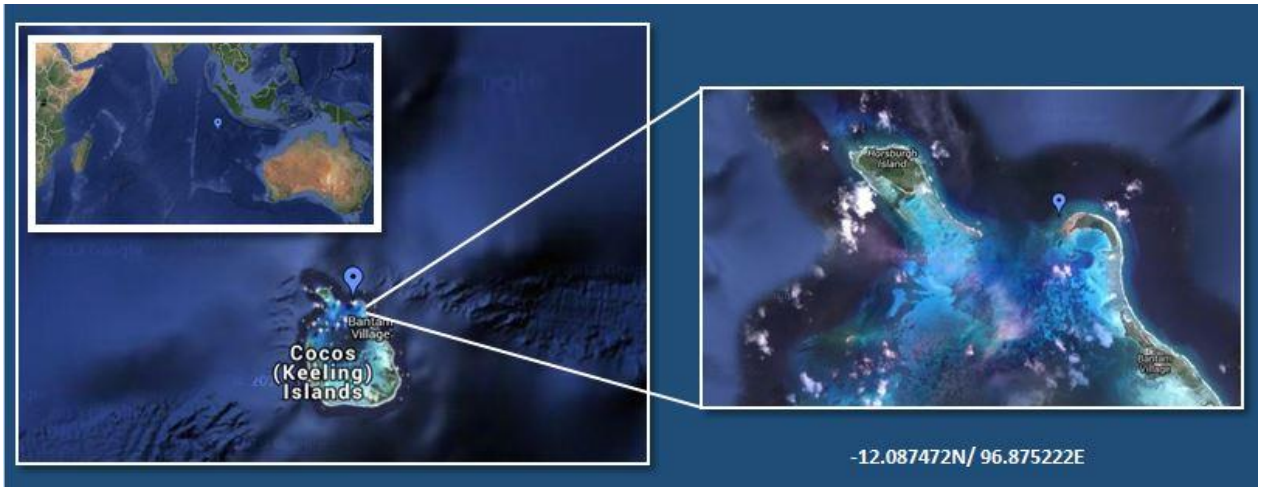

Figure 1.1. Location of Cocos (Keeling) island and exact location of the coral core Darwin Long.

Chapter 2 Background

2.1. Regional and local climatology

2.1.1. Mean climate and ocean basin characteristics

The Indian Ocean basin belongs to the three largest ocean basins of the world, together with the Pacific and Atlantic basins. The ocean is bounded in the north by the Eurasian continent, in the west by the African continent, and in the east by the Australian continent. Heat differences between the Eurasian continent and the ocean drive the strongest monsoon on Earth: the Asian monsoon. The monsoonal winds create seasonal variations in the ocean currents in the ocean basin. The ocean currents existing in the Indian Ocean basin are displayed below in Figure 2.1. The region of Cocos (Keeling) island is mainly influenced by the Indonesian Throughflow (ITF), which transports Pacific Ocean waters to the Indian Ocean resulting in an exchange between the two different ocean basins. The outflow of the ITF varies seasonally with maximum outflow in June/July and minimum outflow in February. It also varies on an interannual timescale linked to ENSO and other forcing factors (Schott et al. 2009). The ITF feeds the Southern Equatorial Current (SEC), which subsequently flows from the eastern part of the Indian Ocean to the western part.

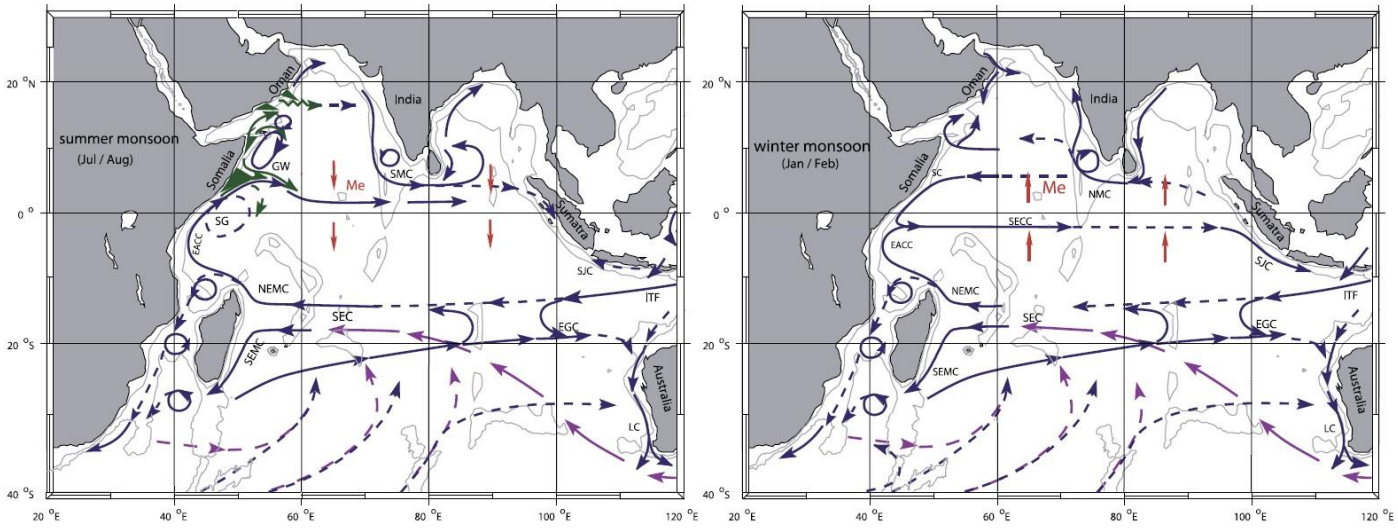

Figure 2.1. Visualization of the ocean currents in the Indian Ocean during the summer monsoon (left) and winter monsoon (right). The ocean currents are: South Equatorial Current (SEC), South Equatorial Countercurrent (SECC), Northeast and Southeast Madagascar Current (NEMC and SEMC), East African Coastal Current (EACC), Somali Current (SC), Southern Gyre (SG), Great Whirl (GW), Southwest and Northeast Monsoon Currents (SMC and NMC), South Java Current (SJC), East Gyral Current (EGC), Leeuwin Current (LC) and the Indonesian Throughflow (ITF). Furthermore, green are upwelling wedges; red are directions of meridional Ekman transports; purple are subsurface flow of supergyre. Depth contours are displayed for 1000 and 3000 m depth (grey). From Schott et al. (2009).

The Intertropical Convergence Zone (ITCZ) shifts over the Indian Ocean basin due to the seasonal shift in maximal solar heating, resulting in a zone of high convection with high cloud cover and precipitation (Figure 2.2). The ITCZ also marks the rising edge of the Hadley cells that extends from the equator towards 30° S/N. The easterly trade winds are located in the Hadley cell traveling from the descending limb (high pressure) towards the rising limb/ITCZ (low pressure). Contrasting to the equatorial Pacific and Atlantic, easterly trade winds do not prevail in the Indian Ocean basin and are only present during the late winter/early spring. In the Indian Ocean annual mean winds are weak and westerly, resulting in a flat thermocline and little or no upwelling in the eastern equatorial Indian Ocean (Schott et al.

2009). According to Grove (2012) precipitation patterns are similar to SST patterns in the ocean, suggesting a strong coupling between the two.

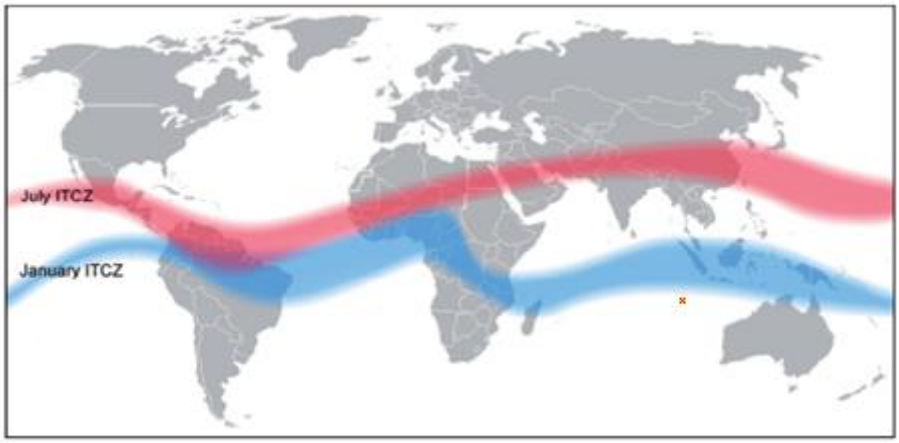

Figure 2.2. The position of the Intertropical Convergence Zone is austral summer/January (blue) and austral winter/July (red). The position of Cocos (Keeling) island is marked on the map. From Grove (2012), edited.

Besides the shifting of the ITCZ, there are several types of intra-seasonal climatic cycles active in the Indian Ocean, including Madden-Julian Oscillations (MJOs) that propagate to the east (Schott et al. 2009). This study focuses on interannual climate variability, so it will not discuss these variabilities into detail. However, this study tries to link extreme events as cyclones to the reconstructed climatic proxy records ($\delta^{18}O$ and Sr/Ca) and research if these events are linked to interactions between the ocean and the atmosphere. See Section 2.1.2 for further information about cyclones affecting the Cocos region.

Earth's climate is changing globally (IPCC, 2013) and this climate change is also apparent in the Indian Ocean. SST has warmed in the Indian Ocean with 0.5°C over the past 50 years (Schott et al. 2009). The Indian Ocean does not warm uniform, but there are regional differences that can be explained by ocean dynamics. With global warming, the ITF will weaken forced by a weaker Pacific Walker circulation (Vecchi and Soden, 2007).

2.1.2. Ocean-atmosphere systems influencing Indian Ocean region

The ENSO is an ocean-atmosphere variability that originates in the Pacific Ocean. The cycle of the ENSO, that occurs every 2 to 7 years, consists of a fluctuation between unusually warm (El Niño) and cold (La Niña) conditions (McPhaden et al. 2006). The occurrence of the ENSO cycle is linked to fluctuations in the Southern Oscillation, the tropical pressure pattern located in the tropical Indian and Pacific Oceans that is related to the strength of the Pacific trade winds (McPhaden et al. 2006). In a normal state in the Pacific Ocean, colder temperatures in the eastern part of the basin drive stronger easterly trade winds, shallowing the thermocline and increasing upwelling, this results in further cooling of the SSTs in the east (Cane, 2005). This coupled process between the ocean and the atmosphere is known as the Bjerknes feedback. During El Niño, this positive feedback is reversed: the east starts to warm due to deepening of the thermocline, warming depresses the SST difference between east and west and decreases the strength of the trade winds, this reduces upwelling and transport of colder waters (Cane, 2005; McPhaden et al., 2006). The El Niño ends due to a negative feedback of equatorial wave-induced cooling, when strong enough this feedback may initiate a La Niña event (McPhaden et al. 2006). Although the ENSO originates in the Pacific Ocean, it influences the climate globally through atmospheric teleconnections. The changes in convection during El Niño alters atmospheric circulation remotely in tropics and extratropics through atmospheric wave adjustments, the atmospheric bridge (Schott et al., 2009). The ENSO can have dramatic global effects, which was

the case during for example the exceptionally large El Niño of 1997-1998. The ENSO also affects the frequency, intensity and distribution of tropical storms (McPhaden et al. 2006). During the positive mode of the ENSO (El Niño) the Indian Ocean also warms, peaking in the boreal spring (March-May), this is occurring one season after the maximum warming in the Pacific Ocean (Grove, 2012). Much of this warming in the Indian Ocean basin originates from changes in surface heat fluxes, such as wind-induced latent heat and cloud-induced solar radiation fluxes (Grove, 2012). In Figure 2.3 global SST changes are shown for a positive ENSO event. Besides the surface heat fluxes, ocean dynamics play an active role in increasing SST in the western Indian Ocean. The wind stress from the atmospheric bridge between the Indian and Pacific Ocean forces downwelling Rossby waves in the southeast Indian Ocean propagating to the southwest, where they deepen the thermocline and warm local SST (Xie et al. 2002; Grove, 2012).

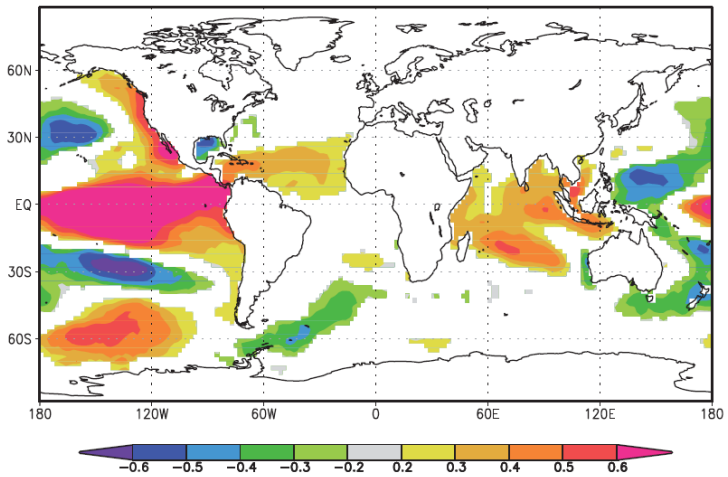

Figure 2.3. Correlation of global SST (ERSSTv.3) with Nino 3.4 index during the season JFMA. From Grove (2012).

Only two decades ago a coupled ocean-atmosphere phenomenon originating in the Indian Ocean is established by the study of Saji et al. (1999), the Indian Ocean Dipole (IOD). The IOD occurs every 2-5 years and is recognized as an east-west SST anomaly in the Indian Ocean (Saji et al., 1999; Singh, 2008). In the positive (negative) mode of the IOD the southeastern Indian Ocean has cool (warm) sea surface temperatures (SST) anomalies and simultaneously the southwestern Indian Ocean is warm (cool) (Ash & Matyas, 2012). The strength of the SST dipole mode is tightly coupled to the strength of zonal wind anomalies over the equator (Saji et al., 1999). In the eastern equatorial Indian Ocean (EEIO) mean annual winds are weak and westerly, the thermocline is flat and there is almost no upwelling. Despite these facts, there is a Bjerknes feedback active in the Indian Ocean induced by strong seasonal variability of monsoonal winds during the summer and fall (Schott et al. 2009). During summer, easterly winds along the equator force a shallow thermocline and upwelling in the EEIO, activating Bjerknes feedback and the IOD. The IOD is thereafter rapidly terminated by intense monsoonal forcing weakening southeasterly winds in the EEIO (Schott et al., 2009). The significant SST anomalies of the IOD appear in June, intensify in the following months and peak in October (Saji et al., 1999). The eastern Indian Ocean cooling during a positive IOD is enhanced by strengthened southeasterly trade winds, this causes enhanced ocean surface evaporation and mixing. Simultaneously, the western Indian Ocean becomes warmer. Warm tropical waters are transported to the western Indian Ocean due to an increased poleward Ekman transport. Also, both equatorward cold air advection and ocean surface evaporation become smaller, causing further warming in the western Indian Ocean. (Ash & Matyas, 2012). See Figure 2.4 for anomalous SST and surface wind anomalies during an IOD event. During an IOD event there is also a rainfall anomaly present over the tropical Indian Ocean: precipitation increases in the west, due to low-level convergence linked to anomalous easterly winds,

and precipitation decreases in the east (Saji et al., 1999; Schott et al. 2009). Recent extreme IOD events occurred in 1961, 1967, 1972, 1982, 1994 and 1997 AD, which can possibly be traced in the reconstructed proxy records of this study.

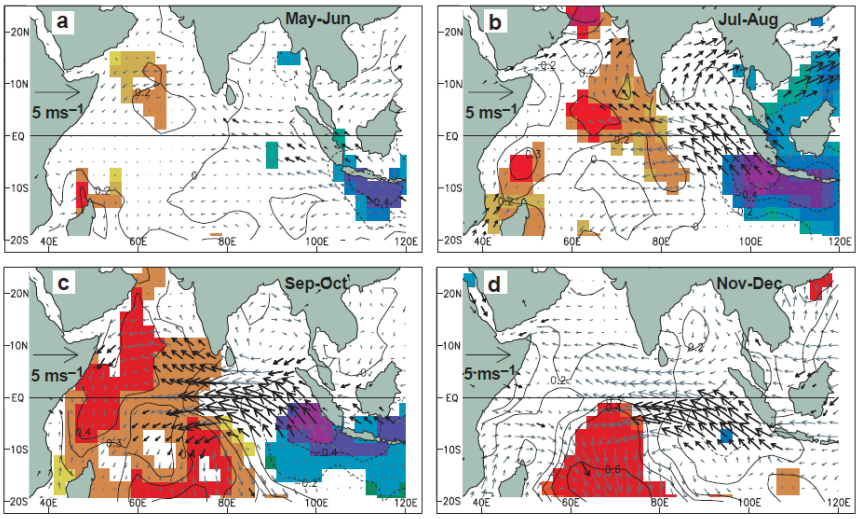

Figure 2.4. Evolution of an IOD event with SST (contours and color shading) and surface wind (arrows) anomalies. The shading and bold arrows indicate SST and surface wind anomalies that exceed 90% significance. a) May-June, b) July-August, c) September-October, d) November-December. From Saji et al. (1999).

Saji et al. (1999) stated that the IOD is occurring independent of the ENSO, but there is also evidence that the IOD and the ENSO show correlation and are somehow linked. An IOD event can be triggered by an ENSO event or can occur independently, when the thermocline off the Sumatran coast is shallow enough to induce Bjerknes feedback and consequently upwelling. Multiple studies show that about half of IOD events occurred independently of an ENSO event (Meyers et al., 2007; Saji et al., 1999; Saji & Yamagata, 2003; Schott et al., 2009). Both events show decadal variation and the correlation between IOD and ENSO also varies on a decadal timescale. The latter is probably caused by the decadal variability of the eastern equatorial thermocline, which might be linked to variations in the strength of the ITF. The correlation between IOD and ENSO is highest when the thermocline is deep and an ENSO event is needed to trigger an IOD (Grove, 2012). Another study links IOD development to the seasonal switch of a neutral/La Niña state to an El Niño state. An IOD event is favored when such a switch occurs in spring/summer, and no IOD will occur when La Niña continues or an El Niño does not develop until fall (Nagura and Konda, 2007).

The PDO is also a coupled ocean-atmosphere system, which influences SST in the Pacific Ocean. During a positive phase of the PDO, low SST's occur in the central midlatitude Pacific and warm SST anomalies occur at the northern and eastern margins and south of 30°N. The cycles of the PDO are on multidecadal timescales, 50-70 years (Minobe, 1997) and on interdecadal timescales, 17-28 years (Meehl and Hu, 2006). The PDO has teleconnections transporting the influence to the Indian Ocean. The Indian Ocean warms during a positive phase of the PDO (Deser et al., 2004), especially the southwestern Indian Ocean warms. Anomalies of the PDO are thought to exceed anomalies related to the ENSO (Krishnan and Sugi, 2003). The PDO also affects rainfall patterns.

2.1.2. Cocos (Keeling) island

The Cocos (Keeling) islands are a group of 27 coral islands consisting of two large coral atolls located in the remote eastern part of the Indian Ocean. The coral core used in this study originates from the southern atoll (see Figure 1.1. for exact location). This region is influenced by a tropical climate with fairly uniform atmospheric temperatures throughout the year. The annual average mean maximum temperature is 29.1°C taken over a period of 63 years (1952-2015), with February/March being the warmest months (average 30°C) and July being the coldest month (28°C) (Bureau of Meteorology climate statistics webpage, 2015). The mean annual precipitation taken over a period of 112 years (1901-2015) is 1977.1 mm, with March/April being the wettest months (>230 mm/month) and September/October being the driest months (<95 mm/month) (Bureau of Meteorology climate statistics webpage, 2015). In Figure 2.5 some climate variables for Cocos (Keeling) island are displayed from 1900 to present. For details about the datasets of displayed in Figure 2.5, see Section 3.3.

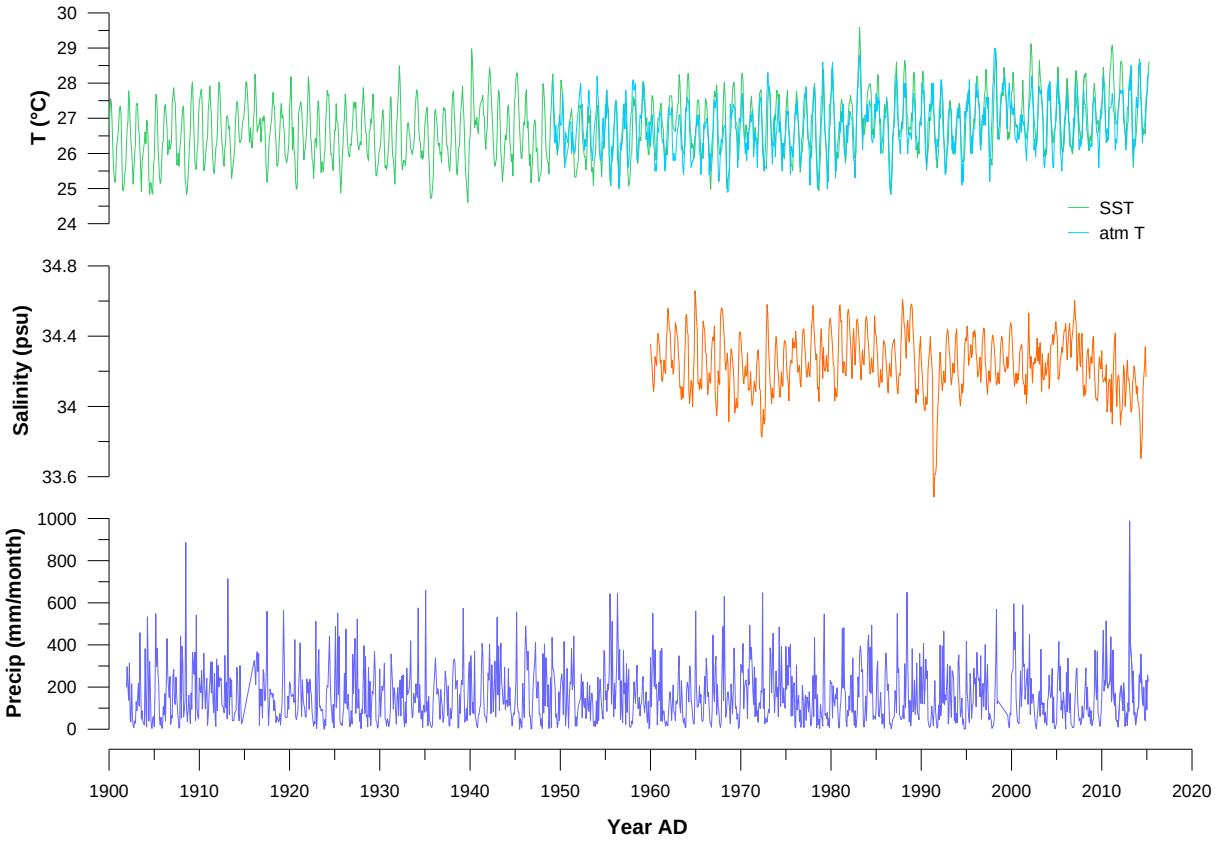

Figure 2.5. Graph of climatic variables at Cocos (Keeling) island from 1900 to present.
In blue is the precipitation in mm/month (GHCN v2); in orange is the salinity in psu (EN4); in green is the SST (NCDC ERSST v3b) and in light blue is the atmospheric monthly mean temperature (GHCN v3).

The region around Cocos (Keeling) island is frequently affected by tropical cyclones. Since 1952 AD a number of 27 cyclones passed the region. On average this is one tropical cyclone causing damage (>90 km/h) every two years and one tropical cyclone causing destructive winds (>125 km/h) every 14 years (Bureau of Meteorology cyclone webpage, 2015). See Figure 2.6 for cyclone trajectories affecting the Cocos region from 1952-2005 AD. The occurrence of cyclones in the Cocos region is centered to the winter/early spring months (Figure 2.7).

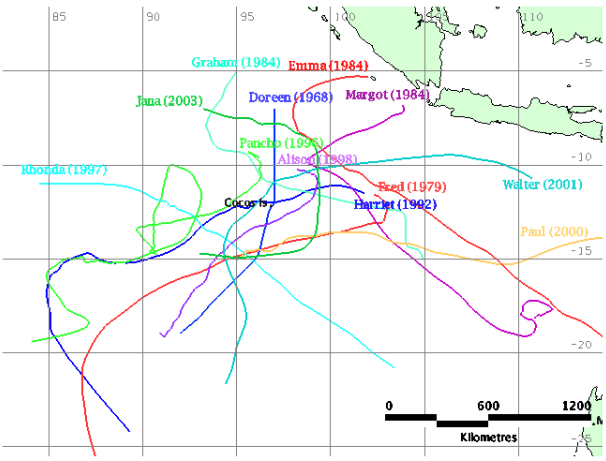

Figure 2.6. Tracks of cyclones (category 2 or stronger) passing the Cocos (Keeling) island region from 1952-2005 AD. From Bureau of Meteorology cyclone webpage (2015).

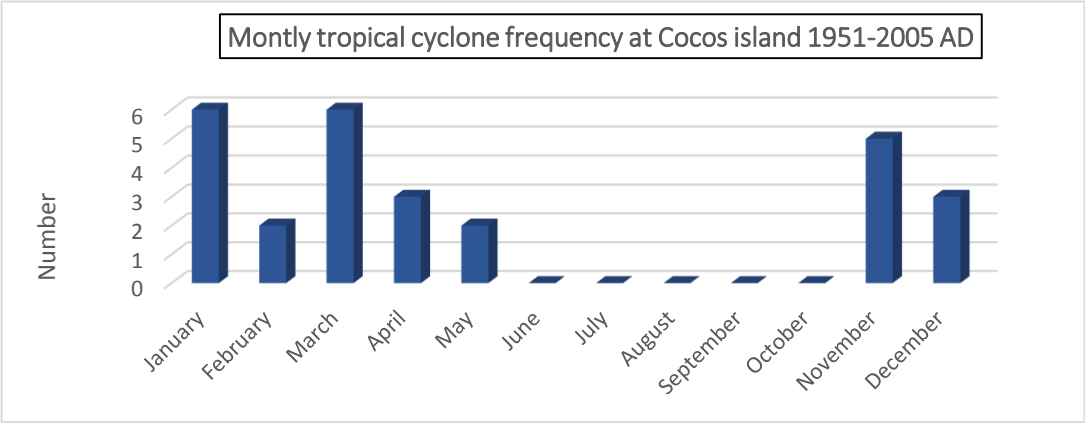

Figure 2.7. Monthly tropical cyclone frequency at Cocos (Keeling) island from 1951-2005 AD. Data from Bureau of Meteorology cyclone webpage (2015).

There are some tropical cyclone events known that have heavily impacted the Cocos (Keeling) islands destroying fauna and settlements. The most severe tropical cyclones of the past recent centuries occurred in: the year 1862; January 28, 1876; February 4, 1893; March 4, 1902; November 27, 1909; January 1986 (called Doreen); February 1992 (called Harriet) (Bureau of Meteorology cyclone webpage, 2015).

2.2. Corals as climate proxy

2.2.1. Poritadae *Porites*

Corals are known to be excellent climate archives for reconstruction of the past hundreds of years (max. ~400 years). Climate changes are recorded in the aragonite structure as physical, isotopic and geochemical evidence. Seasonal variability results in banding of the coral structure, comparable to tree rings, allowing to easily determine age and individual years in coral cores. One year consists of a high density band and a low density band, the accretion of these density bands is influenced by environmental factors, such as sun hour, light transparency, nutrient exposure, partial pressures and temperature (Grove, 2012).

The coral species used in this study, Poritadae *Porites* spp. (Figure 2.8), belongs to the order Scleractinian corals, which are also known as stony corals. These corals are a symbiotic relationship

between cnidarian invertebrates and intracellular dinoflagellate algae of the genus Symbiodinium, Zooxanthellae (Grove, 2012). Photosynthetically fixed carbon from the algae can provide the coral host often with sufficient energy for metabolism, speeding up the calcification process and thus enhancing coral growth (Muller-Parker & D'Elia, 1997). In return, the algae receives inorganic nutrients which the coral produces during metabolism and is protected from threats such as UV radiation (Muller-Parker & D'Elia, 1997). The coral *Porites* spp. can live for centuries and creates giant structures. The coral has a spherical or hemispherical shape when small and a dome shape when large, this may exceed 5 meters in diameter.

Figure 2.8. A giant structure of the coral *Porites* species. From Grove (2012), photograph taken by Dr. Jens Zinke.

2.2.2. Stable oxygen isotope composition

The $CaCO_3$ shell of marine organisms is formed by the aggregation of Ca^{2+} and HCO_3^- ions from seawater. The isotopic composition of the $CaCO_3$ shell therefore resembles the isotopic composition of the surrounding ocean water. Epstein et al. (1951, 1953) determined a relationship between temperature and relative ^{18}O abundances in calcium carbonate in marine shells. They found that in marine surface waters the relative ^{18}O in marine waters increases with increasing temperature and salinity. The relationship proposed by Epstein et al. (1953) between temperature and isotopic oxygen composition is:

$$T(℃) = 16.5 - 4.3\delta + 0.14\delta$$

, where δ is the difference of the $^{18}O/^{16}O$ ratio ($\delta^{18}O$) between the sample and the reference gas.

Weber & Woodhead (1972) state that the oxygen isotopes in the aragonite of scleractinian reef building corals are not in isotopic equilibrium with the surrounding marine waters. The relationship proposed by Epstein et al. (1951, 1953) is only applicable under isotopic equilibrium conditions and therefore not suitable for palaeoclimatic research based on corals. A disequilibrium in isotopic values between the coral carbonate and the surrounding seawater can be caused by chemical/kinetic factors or by metabolic effects (McConnaughey, 1989; Weber & Woodhead, 1970). For the formation of skeletal carbonate the coral forms calcium carbonate inorganically from dissolved bicarbonate (HCO_3^-) in seawater, but it also uses respiratory CO_2 as a source of carbon and oxygen (Weber & Woodhead, 1970). During cellular respiration coral polyps produce carbon dioxide and water. Zooxanthellae that are present in coral tissue use the carbon dioxide and water in the process of photosynthesis. The products of photosynthesis are sugars, lipids and oxygen, these products are then used by the coral

polyp to grow and carry out cellular respiration (Muller-Parker & D'Elia, 1997; NOS webpage, 2015). The additional use of the respiratory CO_2 in carbonate formation causes that both elements of carbon and oxygen are enriched in the lighter isotopes compared to the elements in inorganically formed carbonate (Weber & Woodhead, 1970; 1972). This is because of oxygen isotope fractionation in respiration (Dole, 1956). The presence of Zooxanthellae in coral tissue cause therefore that the $\delta^{18}O$ value of coral carbonate is lower (more negative) compared to the shells of many other marine organisms.

The oxygen isotopic composition of the coral structure provides information on SST, sea surface salinity and the hydrological balance (McConnaughey, 1989; Zinke et al., 2004). Pairing of a $\delta^{18}O$ record with a geochemical SST proxy such as Sr/Ca (see Section 2.2.3.) gives a more accurate indication of past hydrological changes (Pfeiffer et al., 2006; Zinke et al., 2004).

2.2.3. Strontium/Calcium isotope composition

Corals incorporate strontium and calcium into their aragonite structure. In the coral aragonite ($CaCO_3$) Sr^{2+} ions substitute for Ca^{2+} ions, dependent on temperature. The Sr/Ca ratio has an inverse correlation to SST, more strontium is incorporated at lower temperatures. The Sr/Ca ratio is thought to be the most robust SST proxy for corals (Alibert & McCulloch, 1997; Beck et al., 1992; Corrège, 2006; Moreau et al. 2015; Nurhati et al., 2009). Sr/Ca is a more robust SST proxy than $\delta^{18}O$, since the Sr/Ca composition of the ocean is fairly uniform, due to the long residence time of Strontium and Calcium in the oceans, therefore Sr/Ca remains constant over timescale of about 105 years (Beck et al. 1992).

Chapter 3 Methodology

3.1. Coral sampling and measurement

The coral core Darwin Long was drilled in February 2010 at the southern atoll of the Cocos (Keeling) islands (Figure 1.1). The exact coordinates of the drilling location are -12.087472°N/96.875222°E. The coral colony is the scleractinian coral *Porites* spp. and the water depth was 5.8 meters. The core has a total length of 194.5 cm and was drilled vertically into the apex of the colony using a pneumatic drill equipped with a diamond head drill bit with an inner diameter of 40mm. As preparation before subsequent analyses the core was soaked in fresh water for 24 hours and sliced into 7 mm thick slabs. These slaps were subsequently rinsed with sodium hypochlorite (NaOCL, 10-13% reactive chloride, Sigma-Aldrich Company) for 24 hours to remove organic matter. Pictures of the coral core Darwin Long are attached in Appendix 1.

Next, the coral core was X-rayed (See Appendix 2) and scanned using Spectral Luminescence Scanning (SLS; See appendix 3) in order to reveal density and luminescence bands to construct a first chronology and determine a suitable transect for the samples to be taken. The core Darwin Long spans a period of 200 years and dates back to the year 1809 AD. The individual samples were taken by drilling small holes over a transect in the coral using dental drill with a diameter of 0.9 mm (Horico H164 009). The intervals between the samples are 1.25 – 1.5 mm and the transect is taken along the main growth axis of the coral. Since the growth rate of the coral is established at 1.1 cm a year, the resolution of the samples is monthly to bi-monthly.

Sr/Ca and Mg/Ca measurements were already done previously in 2011 as part of another project (WOTRO-EKP). All the samples (1227 in total) were analyzed for Sr/Ca and Mg/Ca by ICP-OES (SPECTRO CIROS SOP) at the University of Kiel. The samples were powdered and approximately 1mg per sample was dissolved with nitric acid (HNO_3, 2%) and further diluted to a solution of 8 ppm Ca. The scale of detection of ICP-OES was for Strontium set to 317nm, for Magnesium to 279nm and for Calcium to 407nm. The samples were measured against the standards JCp-1 (RSDSr=0.09%, RSDMg=0.20%), BermudaKoralle (RSDSr=0.10%, RSDMg=0.19%) and Mayot5a (RSDSr=0.08%, RSDMg=0.35%). The standard JCp-1 is a specific coral standard and was used to compare and verify the results of different measurements. The repeated analysis of this standard indicated that the analytical error of the ICP-OES device of the University of Kiel was <0.15% with an analytical precision of ± 0.01 mmol/mol (RSD=0.15%).

This study uses the same samples, as used for the trace element analyses, to do the $\delta^{18}O$ measurements. The samples were analyzed using a carbonate preparation device, Kiel IV, coupled to a Finnigan MAT 253 mass spectrometer at the NIOZ research institute located on Texel, the Netherlands. Of each sample 20-40µg powdered material was reacted with phosphoric acid (H_3PO^4) at a temperature of around 70°C in the carbonate preparation device. The aragonite samples react with the phosphoric acid producing CO_2 gas, the stable isotopic composition of the gas was measured by the mass spectrometer. Two standards were measured along the samples: the international standard NBS-19 and VICS. The standard VICS has a target value of -5.44‰ for $\delta^{18}O$. This makes the VICS standard suitable for these coral measurements since the $\delta^{18}O$ values of coral cores ranges on average around -4 to -5‰. The standard deviation based on multiple analyses (N=94) of the international standard NBS-19 was ± 0.08‰ for $\delta^{18}O$, while for the VICS standard (N=137) the standard deviation was ± 0.09‰ for $\delta^{18}O$. The reconstructed δ18O record is reported relative to the Vienna Peedee belemnite (VPDB). In total 819 samples were analyzed to create the $\delta^{18}O$ record that extends back to midyear 1871 AD. Some of the 819 samples were unfortunately too small to do (multiple) analyses on, so the exact number of data points in the reconstructed $\delta^{18}O$ record is 871.

Together with the $\delta^{18}O$ measurements also $\delta^{13}C$ values of the coral samples were measured using the mass spectrometer (see above). The VICS standard has a target value of 1.35‰ for $\delta^{13}C$ and the international NBS-19 standard has a target value of 1.95‰ for $\delta^{13}C$. The standard deviation based on multiple analyses (N=93) of the international standard NBS-19 was ± 0.04‰ for $\delta^{13}C$, while for the VICS standard (N=144) the standard deviation was ± 0.17‰ for $\delta^{13}C$.

The G/B ratio data was recovered with SLS using the Avaatech XRF core-scanner at the NIOZ research institute located on Texel, the Netherlands. In the core-scanner two long-wave UV-A tubes in the 350-450 nm range were placed as light source. The emission of the light is recorded by a Line Scan Camera. The emission light is split into three wavelength ranges (Red, Green and Blue) by a Dichroic RGB beam splitter prims and recorded by separate filters (Grove et al., 2010).

3.2. Coral chronology

An age model was constructed during the WOTRO-EKP project, based on the Sr/Ca isotope record. The seasonal cycle present in this record was used by assigning the lowest Sr/Ca value of each cycle to the warmest month of that particular year. This warmest month of each year was determined with a gridded ERSST dataset version ERSST.v2 (Smith and Reynolds, 2004) with a window of 95°-97°E; 12°-14°S and an extent till 1854 AD. This dataset consists mainly on historical SST measurements done by ships-of-opportunity, therefore the dataset becomes less reliable prior to 1940 due to sparseness of data. Despite this disadvantage, the age model uses the ERSST dataset to link low Sr/Ca values to the warmest month per year till 1858 AD. Prior to 1858, March was selected as the warmest month on average. Since the variability of the occurrence of the warmest month varies by 1-2 months, the estimated age uncertainty is 1-2 months each year prior to 1858 AD. A monthly time series was subsequently reconstructed by interpolating linearly between the Sr/Ca anchor points using the Analyseries software package (Paillard et al., 1996).

3.3. Metadata

To determine relationships between atmospheric and oceanic conditions, this study will make use of some climate datasets. Most datasets are obtained from the Climate Explorer database provided by the Royal Dutch Meteorological Institute (KNMI; climexp.knmi.nl). Datasets of the following climate phenomena are used in this study and shortly described below: atmospheric mean temperature, local precipitation, local (AIMS) and regional (NCDC, ERSST) SST, salinity, IOD and the ENSO. For references to the exact sources of the datasets, see the reference list.

Atmospheric mean temperature
The monthly atmospheric mean temperature dataset is obtained from the Global Historical Climatology Network (GHCN) version 3, developed by National Oceanic and Atmospheric Administration (NOAA). The dataset originates from measurements at a station on Cocos (Keeling) island: -12.18°N/96.82°E at a height of 3 meters above ground (WMO station code 96996). The dataset covers the period of March 1949 till April 2015.

ENSO
The dataset used to visualize the ENSO is the monthly Nino3.4 index. This Nino3.4 index describes the average SST anomalies over the region 5°N-5°S/170°-120°W. The National Climatic Center (NCC) assigns a warm period to anomalies above 0.8°C and cool periods below -0.8°C (Bureau of Meteorology, About ENSO outlooks). The SST anomalies that are used in the Nino3.4 index are acquired from the ERSST by NCDC v3b. The dataset covers the time period from 1971 to 2000.

Indian Ocean Dipole
The IOD state is represented by the Dipole Mode Index (DMI): the SST difference between the Western equatorial Indian Ocean and the Southeastern equatorial Indian Ocean. For the SST difference between both sides of the Indian Ocean basin, the Extended Reconstructed SST (ERSST) is used. The dataset covers the period of 1854 till present in a monthly resolution.

Local precipitation
The precipitation dataset is obtained from the Global Historical Climatology Network (GHCN) version 2, developed by National Oceanic and Atmospheric Administration (NOAA). The dataset originates from measurements at a station on Cocos (Keeling) island, same station used to measure atmospheric mean temperature see above (WMO station code 96996). The dataset covers the period of December 1901 till March 2015.

Local SST
Local SST data has been purchased from the Australian Institute of Marine Sciences (AIMS). The SST was measured by in-situ data loggers deployed onto the reef. This study used data from six different locations at the Cocos islands. The data loggers instantaneously record the SST every 30 minutes. For more info and details see Table 3.1 and Figure 3.2.

PDO index
The PDO index record is constructed by JISAO (Joint Institute for the Study of Atmosphere and Ocean) from the University of Washington. The data covers the period of 1900-present. The record is based on different SST datasets. From 1900-1981 the record is based on UKMO Historical SST, from 1982-2001 on Reynolds Optimally Interpolated SST (v.1) and from 2002 to present on Reynolds Optimally Interpolated SST (v.2). For more details and extra information on this data record, see Mantua et al. (1997) and Zhang et al. (1997).

Regional SST
A regional SST dataset is obtained from the National Climatic Data Center (NCDC), now called the National Centers for Environmental Information (NCEI) from NOAA. The data is an Extended Reconstructed SST (ERSST) that uses in-situ SST data and improved statistical methods in order to make it possible to make an extended reconstruction when there is sparse data available. Data is available from January 1854 till present. In the early years there is only sparse data so the analyzed signal is damped before 1880, after the 1880 the strength of the signal become more constant over time.

Salinity
The salinity dataset is part of the Met Office Hadley Centre Observations dataset version EN4: quality controlled subsurface ocean temperature and salinity profiles and objective analyses. The dataset is composed of salinity profile data obtained from the WOD09, GTSPP, Argo, and ASBO collections (Good et al. 2013). The data was compared to identify and remove duplicates and a succession of quality control procedures was carried out. The salinity data is acquired from a specific cut-out region around Cocos island: 94.5°-97.5°E/-13.5°-10.5°N. The data covers the period from 1900-2014, but before 1960 AD the dataset seems to be unreliable, because salinity stays almost constant. Therefore, we only used salinity data from 1960 to present.

Sunspot cycle
In order to visualize the sunspot cycle, we obtained a monthly reconstructed solar constant expressed in Total Solar Irradiance (TSI) form Climate Explorer (KNMI). TSI resembles Watt received per square meter surface. The record is constructed using a magnetic flux transport model and comparing the model simulations to geomagnetic activity and cosmogenic isotope records (Lean, 2000; Wang et al., 2005). The TSI data represents a global data record and covers the time period from 1882 to 2009 AD.

3.4. Reconstructing SST and $\delta^{18}O_{sw}$ proxy records

In order to reconstruct the palaeoclimatic records of SST and SSS the paired coral isotopic records of $\delta^{18}O$ and Sr/Ca are used. The coral oxygen isotope composition is both influenced by SST changes and the oxygen isotope composition of the surrounding seawater ($\delta^{18}O_{SW}$) (Epstein et al., 1953; Weber & Woodhead, 1972; Moreau et al. 2015). The $\delta^{18}O_{SW}$ is linearly related to SSS (Fairbanks et al. 1997), since $\delta^{18}O_{SW}$ and SSS are affected by the same processes: the precipitation/evaporation ratio and vertical and horizontal advections (Moreau et al. 2015). The Sr/Ca ratio present in the coral aragonite is a robust and reliable proxy for SST (Beck et al., 1992, Moreau et al. 2015 and Corrège 2006). Therefore SST and SSS changes trough time can be reconstructed by combining Sr/Ca ratios and $\delta^{18}O$ data.

3.4.1. Reconstructing SST from Sr/Ca record

First step is to determine the SST from the Sr/Ca record, the required equation is summarized below:

(1) $\Delta SST = \Delta(Sr/Ca_{(coral)}) / \{\partial(Sr/Ca_{(coral)}) / \partial SST\}$ (Ren et al. 2002)

The term $\{\partial(Sr/Ca_{(coral)}) / \partial SST\}$ is a constant and indicates the rate of change of Sr/Ca with respect to temperature change. This term can be determined by a calibration of the Sr/Ca record to an instrumental/satellite SST record. This study uses Ordinary least Square regression (OLS) in the calibration. Different data can be used to make the calibration between Sr/Ca and SST. Three different calibrations are made using different datasets and/or methods. The best calibration can be made by evaluating the different calibrations and selecting the best correlation for further calculations. Two different SST datasets are used, one local instrumental dataset (AIMS) and a regional satellite ERSST dataset. Instrumental local SST data is recovered from the Australian Institute of Marine Science (AIMS) for six different sites near/around Cocos (Keeling) island, for information see Table 3.1 and Figure 3.1. It is important to use local derived SST data for the SST calibration, since the local settings are comparable and influencing the local SST (Corrège, 2006). In Figure 3.2 the SST data from the different AIMS stations is plotted, together with a composite record that is constructed by averaging all the data. The composite SST AIMS data is compared to the Sr/Ca record.

Name location	ID on map	Depth	Longitude/Latitude	Resolution	Period covered
North point	1	10	96.755/-12.084	monthly	Febr 2006-Jan 2007
Horsburgh	2	10	96.842/-12.070	monthly	Mar 2005-Dec 2006
Cabbage Patch	3	10	96.843/-12.095	monthly	Sep 2003-Nov 2004 Mar 2006-Apr 2009
100th site	4	3	96.871/-12.107	monthly	Jan 2005-Dec 2005 Jan 2007-Febr 2007
Pulu Chepolok	5	10	96.922/-12.136	monthly	Apr 2002-Jan 2004
Banyak Coral	6	10	96.817/-11.830	monthly	Apr 2002-Jan 2004 Mar 2007-May 2008
Composite dataset				*monthly*	*Apr 2002-Apr 2009*

Table 3.1. Information AIMS SST loggers for different locations around Cocos (Keeling) island. *The ID on map correlates to the location on the map in figure 3.1. The last row represents the composite record from the six different locations, reconstructed by combining and averaging the SST values.*

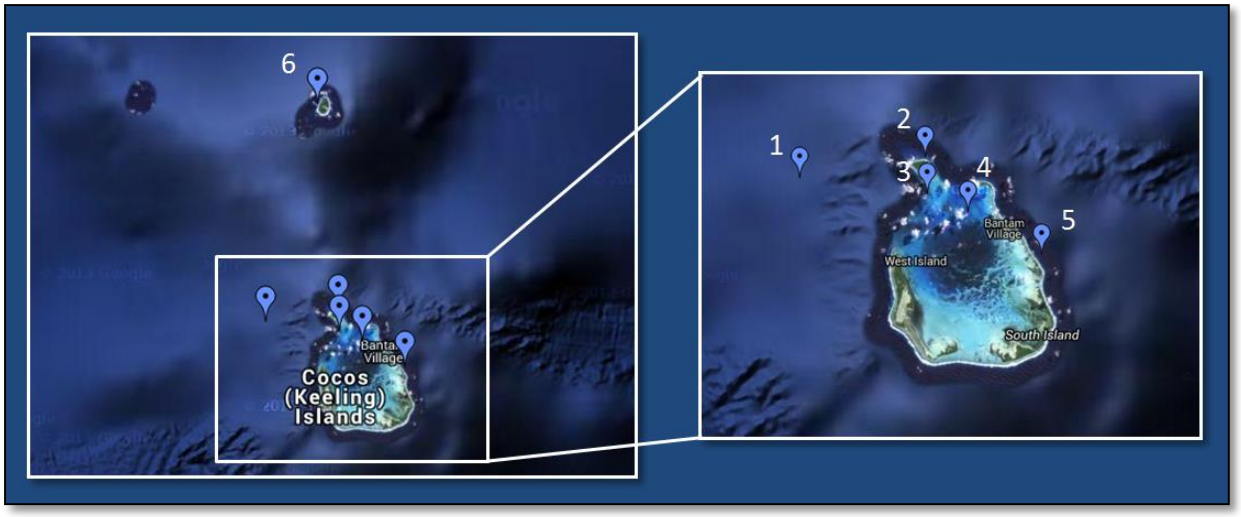

Figure 3.1. Locations of the AIMST SST loggers around Cocos (Keeling) island. *See table 3.1 to link the ID on the map (number) to the different AIMS locations.*

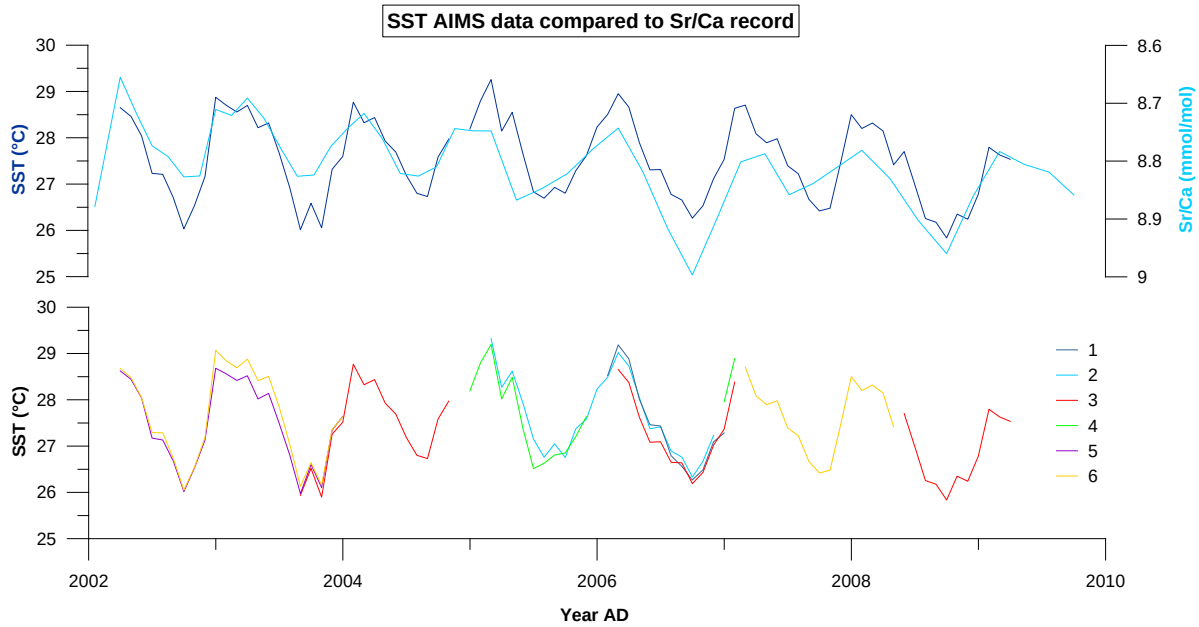

Figure 3.2. Plot of the SST AIMS data compared to the Sr/Ca record. *The upper graph shows the composite SST AIMS record, reconstructed by averaging the data compared to the Sr/Ca record. In the lower graph the individual SST AIMS data are shown, basis for the composite records. The numbers in the legend correspond to the ID in table 1 and figure 1.*

The different correlations for calibration are presented in Figure 3.3 and the regression equations are summarized in Table 3.2. The first calibration is based on the complete SST composite record of AIMS and the Sr/Ca record. A second calibration is done by using only minimum and maximum values of the AIMS SST dataset and the Sr/Ca record, instead of using all data points. This method is chosen, because the use of only minimum and maximum values should reduce spreading around the regression line, resulting in a better correlation. The minima and maxima of both records do not perfectly match in time, this is caused by the error (1-2 months) in the age model of Sr/Ca. Also a calibration is made based on a regional ERSST satellite dataset (NCDC ERSST, v3b). It is very important to compare the local SST dataset with a regional SST dataset to see if the two data records have a good correlation. This step is important to determine if the local dataset has the ability to represent

regional climate variability (Corrège, 2006). The correlation between the two different SST datasets, local and regional, is also displayed in Figure 3.3.

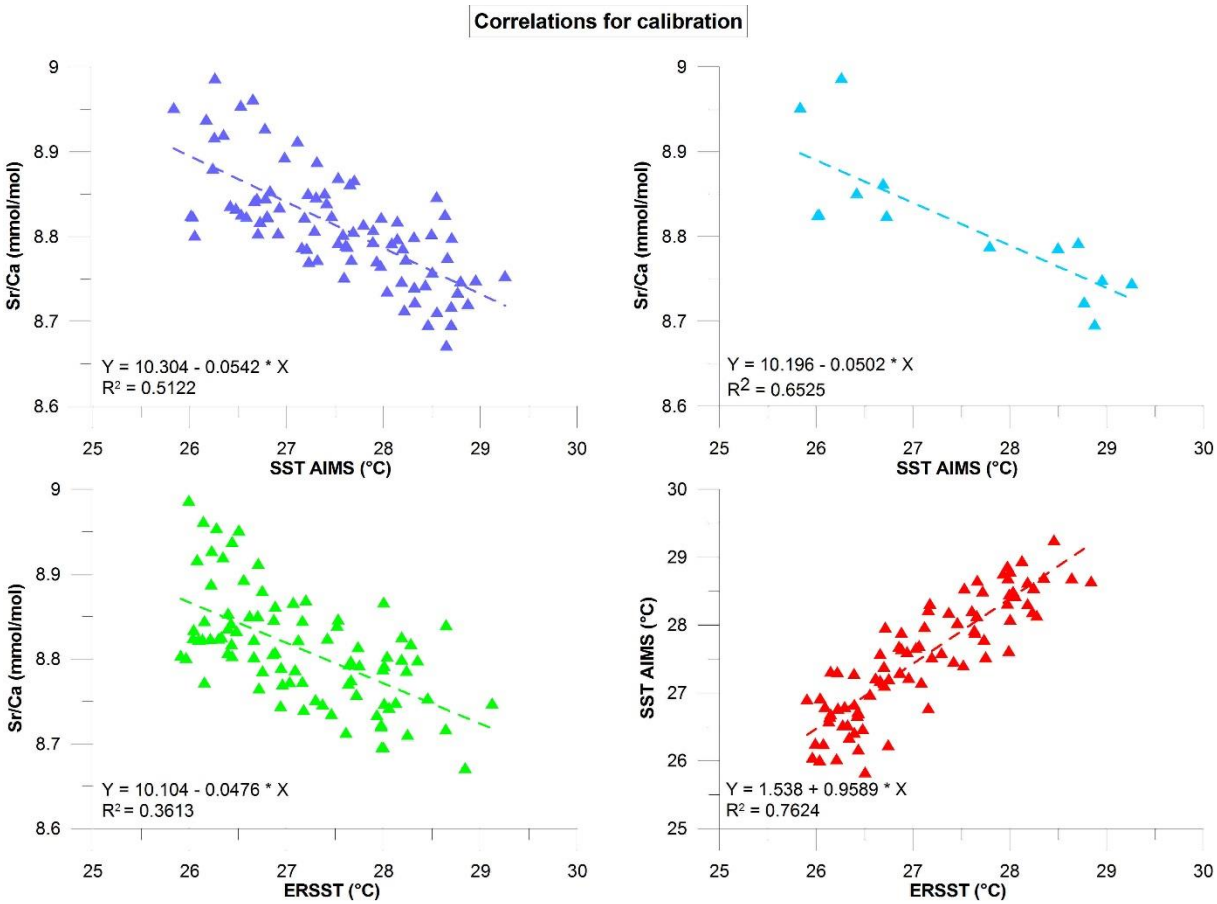

Figure 3.3. Correlations to determine the regression equations for calibration and comparison local (AIMS) to regional (ERSST) temperature variability.

The regression equation and R^2 value determining the correlation are displayed in the chart. Upper-left: correlation between the SST composite AIMS record and the Sr/Ca record. Upper-right: the correlation between the minima and maxima of the SST composite AIMS record and the minima and maxima of the Sr/Ca record. Lower-left: correlation between the ERSST record and Sr/Ca. Lower-right: correlation between the ERSST record and the SST composite AIMS record.

Dataset	Regression equation	R^2
Sr/Ca record Cocos (Keeling) island		
Composite local SST loggers AIMS – all data	Sr/Ca = 10.304 – 0.0542 · SST	0.5122
Composite local SST loggers AIMS – Min/Max	**Sr/Ca = 10.196 – 0.0502 · SST**	**0.6525**
NCDC ERSST v3b	Sr/Ca = 10.104 – 0.0476 · SST	0.3613
Comparing SST datasets		
NCDC ERSST & Composite local SST loggers AIMS	SST AIMS = 1.538 + 0.9589 · ERSST	0.7624

Table 3.2. Linear regression equations and correlation coefficients for the Sr/Ca record from Cocos (Keeling) island and local and regional SST datasets.

The slope $\{\partial(Sr/Ca_{(coral)}) / \partial SST\}$ is generally found to range between -0.04 to -0.08 ‰/°C in coral species (as well as particular coral species *Porites)* (Corrège, 2006; Cahyarini et al. 2008), agreeing with the slopes found in the calibration functions of this study (see Table 3.2). The calibration using only the minima and maxima of both the composite SST AIMS record and the Sr/Ca record, presents the best

calibration, as shown by the highest coefficient of determination (R^2). Therefore this calibration will be used for further calculations.
The correlation between the two different SST datasets, local AIMS and the regional ERSST, shows a strong correlation ($R^2 \approx 0.76$). This indicates that the local SST signal is highly influenced by more regional processes influencing SST. Using the local AIMS SST data for calibration will therefore not limit us to only local processes, but it will also be possible to distinguish regional processes.

3.4.2. Reconstructing $\delta^{18}O_{sw}$

Now the Sr/Ca-SST relationship is determined, the contribution of SST on the $\delta^{18}O$ record can be calculated ($\Delta\ \delta^{18}O_{SST}$). Since the oxygen isotopic composition of corals are both determined by SST changes and by changes in the $\delta^{18}O$ of the seawater, the $\delta^{18}O_{sw}$ can in turn be computed by using the following formulae:

(2) $\Delta\ \delta^{18}O_{coral} = \Delta\ \delta^{18}O_{SST} + \Delta\ \delta^{18}O_{SW}$

There are multiple different methods to calculate the $\delta^{18}O_{SST}$. This study will calculate the $\delta^{18}O_{SST}$ and the $\delta^{18}O_{SW}$ using two different methods that are both specially developed for corals: an advanced method originating from the study of Ren et al. (2002) and a more simplified method using an equation established by Weber & Woodhead (1972). Since the method of Weber & Woodhead (1972) is a largely simplified method by not considering $\delta^{18}O_{SW}$ variations, it is only used as a separate method to check the results found by the Ren et al. (2002) method. The method of Ren et al. (2002) uses a resampled monthly age model in the calculations, while the method of Weber & Woodhead (1972) uses the original age model. Therefore the method of Weber & Woodhead (1972) is also used to check whether resampling of the age model will result in deviations.

The widely used method that was proposed by Grossman & Ku (1986) is not evaluated here, since this method is only established for other aragonite fossils as foraminifera and mollusks. The established relationship cannot be used in this study on corals, since the process of aragonite precipitation in corals is fundamentally different from other aragonite fossils. The coral-algae symbiont causes deviation from the general fractionation process, amongst others by using metabolic carbon dioxide in aragonite precipitation. Therefore the oxygen composition of the coral aragonite is not in equilibrium with the $\delta^{18}O$ of the surrounding seawater (see Section 2.2.2.).

3.4.2.1. Method 1: Ren et al. (2002)

This method is based on a method proposed by the study of Ren et al. (2002). This method needs a monthly $\delta^{18}O$ record, so the first step is to resample the raw $\delta^{18}O$ record to a monthly resolution using the Analyseries software package (Paillard et al., 1996). The further calculations are executed with instantaneous changes, so the calculated $\delta^{18}O_{SST}$ and $\delta^{18}O_{SW}$ are anomalies.

The calculations can be made by using central Equation 1. This equation can be written differently and more detailed as:

(3) $\Delta\delta^{18}O_{(coral)} = (\partial\delta^{18}O_{(coral)}/\ \partial SST) \cdot \Delta SST + (\partial\delta^{18}O_{(coral)}/\ (\partial\delta^{18}O_{(SW)}) \cdot \Delta\delta^{18}O_{SW}$ (Ren et al. 2002)

The terms $\{\partial\delta 18O_{(coral)}/\partial SST\}$ and $\{\partial\delta 18O_{(coral)}/\partial\delta 18O_{SW}\}$ are partial derivatives and give the rate of change of $\delta^{18}O_{(coral)}$ with a change of SST and $\delta^{18}O_{SW}$, when the other variable is constant (Ren et al. 2002).

To calculate $\delta^{18}O_{SST}$ Equation 3 can be rewritten to:

(4) $\Delta\ \delta^{18}O_{SST} = \Delta(Sr/Ca_{(coral)}) \cdot (\partial\delta^{18}O_{(coral)}/\ \partial SST) / (\partial(Sr/Ca_{(coral)}) / \partial SST)$ (Nurhati et al. 2009)

This equation also contains two partial derivatives: { $\partial\delta^{18}O_{(coral)}/\ \partial$SST} and { $\partial(Sr/Ca_{(coral)}) / \partial$SST}. The first derivative gives the rate of change of $\delta^{18}O_{(coral)}$ with a change of SST, when the other variable is constant (Ren et al. 2002). Published estimates of the partial derivative {$\partial\delta^{18}O_{(coral)}/\partial$SST} vary between the values −0.15 and −0.22‰/°C (Weber & Woodhead, 1972; Wellington et al., 1996; Juillet-Leclerc & Schmidt, 2001 and Suzuki et al., 2005). In this study the average value of -0.18‰/°C is used for the {∂δ18O$_{(coral)}$/∂SST} term. The second derivative is already determined by the Sr/Ca-SST calibration in Section 3.3.1 and is established at -0.0502 mmol/mol/°C. Finally, by extracting the $\delta^{18}O_{SST}$ value from $\delta^{18}O_{coral}$ the $\delta^{18}O_{SW}$ can be calculated according to Equation 1.

3.4.2.2. Method 2: Weber & Woodhead (1972)

In the study of Weber & Woodhead (1972) a relationship is proposed between SST and $\delta^{18}O$ of the coral. Oxygen fractionation and incorporation in the skeletal tissue is different for corals than for other calcium carbonate organisms, because of the coral-algae symbiont. Additionally, in their study they found that the relation between SST and $\delta^{18}O$ is species specific. The proportion of seawater bicarbonate and metabolic carbon dioxide that defines the skeletal aragonite composition of the coral is constant per species, but differs between different species. This study defined the different SST-$\delta^{18}O$ relationships per species. The determined relation for the coral *Porites* Poritidae is described by the following equation:

(5) $SST = 11.21 - 3.31 \cdot \delta^{18}O$ (Weber & Woodhead, 1972)

This equation is determined by analyzing 421 different specimens at 26 different sites all over the world. The SST can as a first step be calculated by using the Sr/Ca-SST calibration of the previous section. This method uses the original, non-resampled, age model.

A very important note should be placed by the fact that the study of Weber & Woodhead (1972) does not take $\delta^{18}O_{SW}$ variability into account. This study is interested in separating the $\delta^{18}O$ of the coral into a signal of $\delta^{18}O$ caused by SST variations and a signal caused by $\delta^{18}O$ seawater variations. This is impossible when $\delta^{18}O$ seawater is considered to be constant over time. The $\delta^{18}O$ indicated in Equation 5 can both be $\delta^{18}O_{SST}$ or $\delta^{18}O_{coral}$. The calculations in this study regard the $\delta^{18}O$ term in the equation as $\delta^{18}O_{SST}$, making it possible to calculate $\delta^{18}O_{SW}$. However, when the $\delta^{18}O$ in Equation 5 actually presents $\delta^{18}O$ of the skeletal aragonite, then the difference between the measured skeletal $\delta^{18}O$ value in this study and the $\delta^{18}O$ value calculated using this equation represents differences and uncertainties in the $\delta^{18}O$ of the coral. This difference can be caused by errors in measurement or errors in the Sr/Ca-SST calibration. This large simplification makes this method not suitable for the calculations done in this study. However, it is useful to check the results of the calculations following the Ren et al. (2002) method by another method. Not the exact values can be compared, but no large differences between the methods should be present.

3.5. Spectral analyses

Spectral analysis will be used to determine cyclicities in order to investigate whether the ocean- and atmosphere systems are coupled. When different datasets show same cyclicities, it is likely that they are influenced by same processes and possibly are coupled. Spectral analysis will be carried out using the Analyseries software package (Paillard et al., 1996) and Past software (Hammer et al., 2001).

Several different spectral analyses will be done, focusing on power spectra through REDFIT analysis and Wavelet transforms.

REDFIT analysis (Schulz & Mudelsee, 2002) can be applied to filter cycles from a time series dataset. This analysis filters the cycles out of the data and plots the result in a graph with power against frequency. The power indicates how strong the appearance of the cycle is and the frequency signifies the length of the cycle, the period. REDFIT analysis also makes it possible to do some statistics on the present cycles, to see whether the cycles are significant. Another advantage of this mode of spectral analysis is that it is computed particularly for unevenly sampled palaeoclimatic timeseries so it eliminates red-noise by avoiding interpolation.

Wavelet analysis enables to distinguish non-stationary cycles: cycles that do not have constant amplitudes or frequencies. Wavelet transforms create an image with time against the length of the cycle. The colors indicate the strength or amplitude of the present cycle. This makes it possible to see how cycles change over time and to see whether trends are present.

Chapter 4 Results

4.1. Stable oxygen isotope record and Sr/Ca record

The $\delta^{18}O$ record of the coral core Darwin Long is displayed in Figure 4.1 (red curve). The blue curve in Figure 4.1 is the Sr/Ca record that was reconstructed in project WOTRO-EKP in 2011. The average $\delta^{18}O$ value of the reconstructed record is -4.65‰ with a standard deviation of 0.228‰. The range of the entire $\delta^{18}O$ dataset is between the -3.39 and -5.20‰, so the largest variations in the $\delta^{18}O$ dataset over a period of approximately 140 years is maximum -1.81‰. The average value of the Sr/Ca record is 8.883 mmol/mol with a standard deviation of 0.075 mmol/mol. Yearly averaged records are reconstructed for both $\delta^{18}O$ and Sr/Ca by averaging the data per year, see dark red and dark blue curves in Figure 4.1. The number of samples taken per year varies between 2 and 11, with an average of 6 samples per year, which might influence the reconstructed annual record.

Despite the fact that the records stay relatively constant over time, both $\delta^{18}O$ and Sr/Ca curves show distinct variations on a very short timescale, which relate to seasonal variability. These variations in the $\delta^{18}O$ record are on average around the 0.5‰. There are some clear $\delta^{18}O$ excursions of multiple data points, and multiple years, towards more positive $\delta^{18}O$ values, especially around 1910 and 1965. Similarly, positive $\delta^{18}O$ excursions occur around the years 1883 and 1946, but these are less clear and consist of fewer data points (i.e. less years). The $\delta^{18}O$ record shows also some data points deviating towards more negative values. However these consist generally of only 1 or 2 years (e.g. 1930).
The Sr/Ca record also shows variations towards higher values (i.e. lower temperatures) with approximately the same timing as the positive excursions in $\delta^{18}O$. The most pronounced excursions in the Sr/Ca record occur around 1883, 1946 and 1968. Other times with more positive $\delta^{18}O$ values, around 1910 and 1977, can also be recognized in the Sr/Ca record as slightly higher values.

There are some inconsistencies between the $\delta^{18}O$ and Sr/Ca records, particularly around 1883, 1910, 1946 and 1965-1970. The 1883 event is recorded in both records, but is especially strong in Sr/Ca. The 1910 event is primarily recorded in the $\delta^{18}O$ record, indicated by more positive values lasting almost five years. The shorter 1946 event is recorded in both records but is more pronounced in the Sr/Ca record. Finally the event occurring around 1965-1970 starts with a very distinct positive peak in $\delta^{18}O$ values exceeding the value -3.4‰. Then $\delta^{18}O$ values restore to slightly more negative values around -4‰, which is still relatively positive. At the same time, the Sr/Ca record also shows higher values. The events are marked in Figure 4.1 by grey rectangles.
Final observation is a decadal trend in $\delta^{18}O$ and Sr/Ca towards more negative/lower values starting around 1970 to present. This trend is clearly visible in both records, but more distinct in the Sr/Ca record.

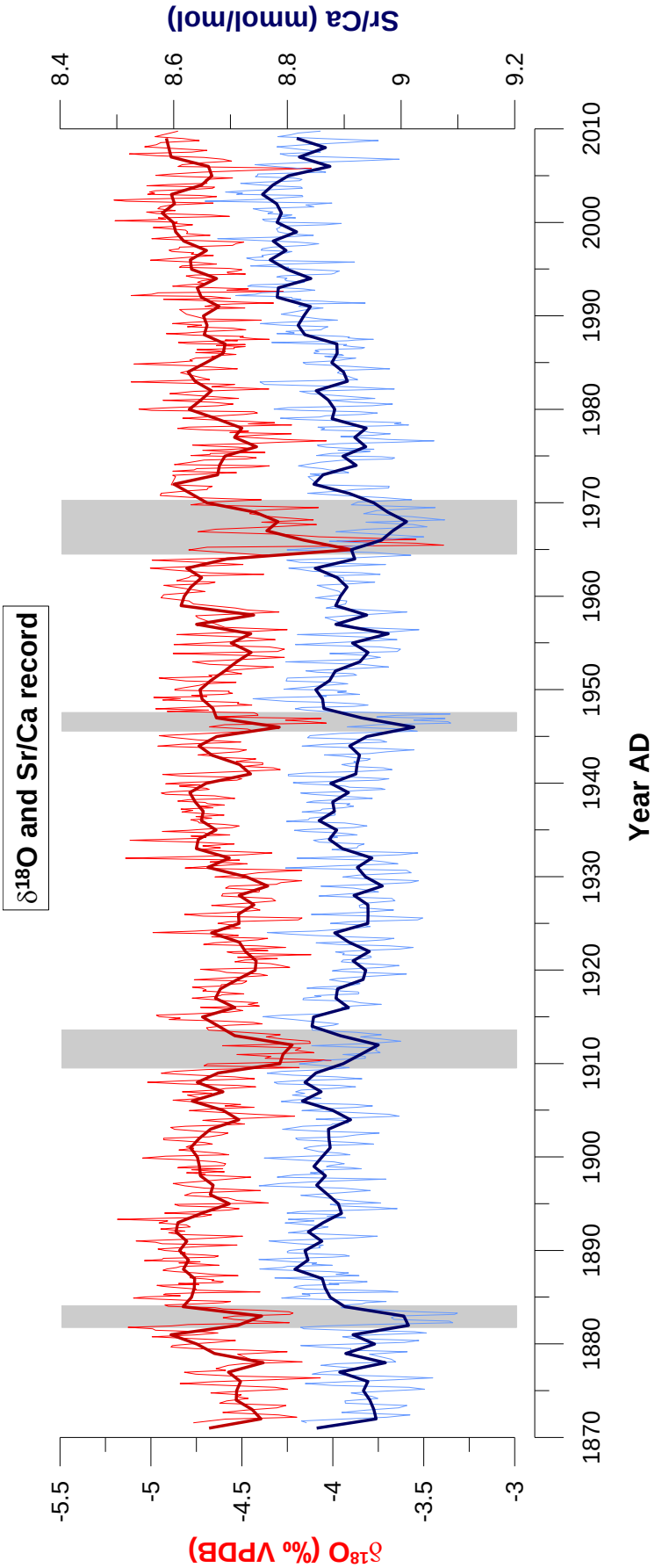

Figure 4.1. The Sr/Ca and $\delta^{18}O$ record of the coral core Darwin Long.
The red record represents the $\delta^{18}O$ record: bright red is the complete reconstructed record; dark red is the yearly averaged record. Values are expressed in per mil, VPDB. The blue record represents the Sr/Ca record: light blue is the complete record reconstructed during project WOTRO-EKP; dark blue is the yearly averaged record. The grey rectangles indicate deviating events.

4.2. Stable carbon isotope record ($\delta^{13}C$)

In Figure 4.2 the data record of $\delta^{13}C$ is displayed (green) together with the $\delta^{18}O$ record, to allow direct comparison between the two. The $\delta^{13}C$ record (light green) also shows variability on a small timescale, which represents annual seasonality. Where the records of $\delta^{18}O$ and Sr/Ca stay relatively constant over time, the $\delta^{13}C$ record shows much stronger variability with amplitudes of around 1.5-2‰. The four pronounced events that can be easily recognized in the $\delta^{18}O$ and Sr/Ca records (Figure 4.1) are also marked in the $\delta^{13}C$ records in Figure 4.2. The $\delta^{13}C$ record shows also positive peaks matching the timing of the four designated events. However, these events are not distinct in the $\delta^{13}C$ record, since the $\delta^{13}C$ record is entirely composed of sharp positive/negative peaks.
In the $\delta^{18}O$ and Sr/Ca record we also recognized a small trend towards more negative values beginning around 1970 AD. In the $\delta^{13}C$ record there seems to be a similar trend present towards more negative $\delta^{13}C$ values, but this trend is stronger expressed in the $\delta^{13}C$ data record.

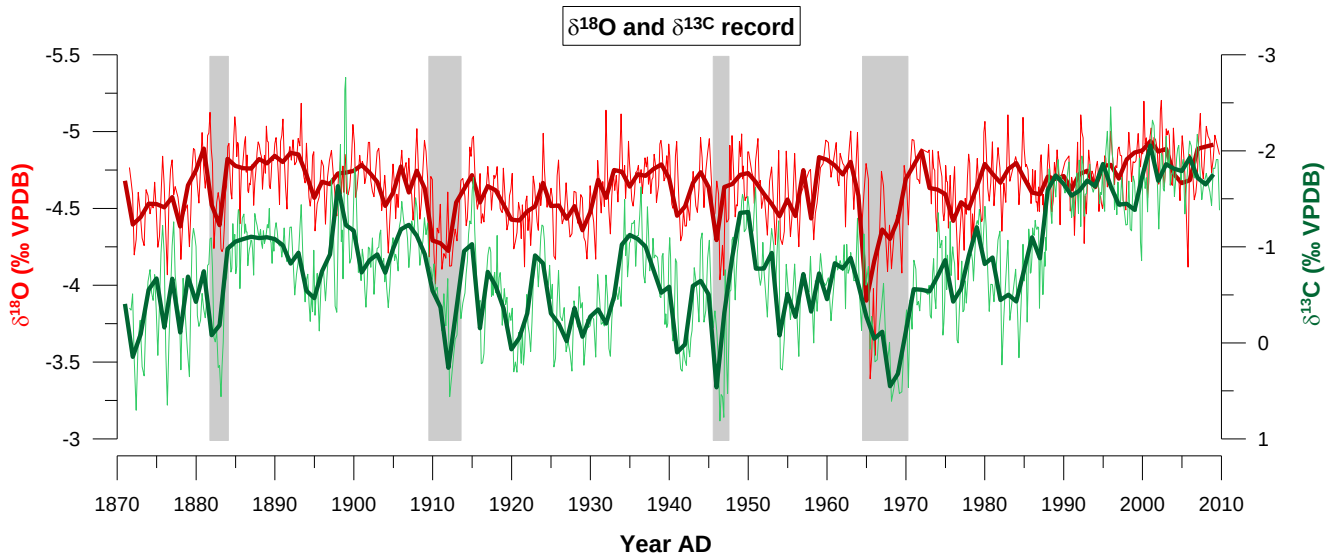

Figure 4.2. The $\delta^{13}C$ and $\delta^{18}O$ record of the coral core Darwin Long.
The red record represents the $\delta^{18}O$ record: bright red is the complete reconstructed record; dark red is the yearly averaged record. Values are expressed in per mil, VPDB. The green record represents the $\delta^{13}C$ record: light green is the complete record; dark green is the yearly averaged record. The grey rectangles indicate deviating events.

4.3. The G/B ratio (Spectral Luminiscence Scanning)

In Figure 4.3 the G/B ratio is shown constructed with Spectral Luminiscence Scanning (SLS). The x-axis represents the position of the scanning device on the coral core in millimeters. The entire core with a length of 194.5 cm was scanned. The most recent part of the coral (around 2009.75) matches with position 0 mm. The end of the coral core, around position 1800 mm, matches the time before 1809 AD and is the part of the coral where banding cannot be easily recognized and is messier in appearance.

The G/B ratio is relatively constant over time with only small fluctuations. The increases towards higher G/B values at the beginning and the end of the record indicate the end of the coral core. The data record reveals a sort of trend from slightly higher G/B values towards slightly lower G/B values over time (towards position 0 mm). Furthermore, there is one very distinct peak present towards lower G/B values around position 143-187 mm. There are some small short-during spikes with higher G/B values, occuring around 740, 826, 964, 1051 and 1256 mm. There is also one small peak to lower G/B values which occurs around 1311-1384 mm.

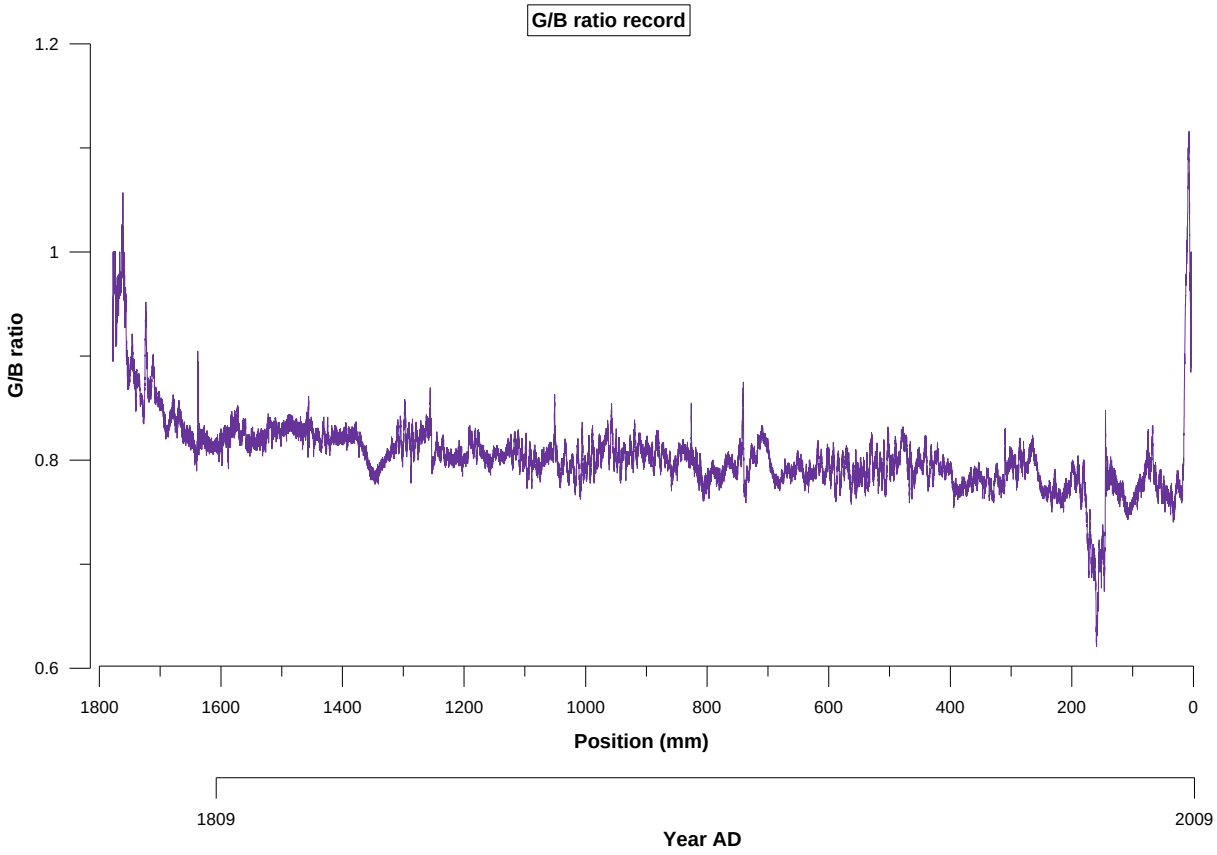

Figure 4.3. The G/B ratio record of the coral core Darwin Long.
The upper x-axis represents the position in the coral core in mm. The lower x-axis represents age: ~5 mm indicates present (2009.750; first sample) and position ~1609 mm refers to the last sample taken with age ~1809 AD.

Chapter 5 Discussion

5.1. Statistical analyses $\delta^{18}O$ record

The correlation between the $\delta^{18}O$ and Sr/Ca measurements is investigated in Figure 5.1. The equation of the fitted linear trend line is presented in the lower left corner of the figure. The R^2 value of the correlation between $\delta^{18}O$ and Sr/Ca is 0.53, meaning that approximately 53% of the variations in $\delta^{18}O$ can be explained by variations in the Sr/Ca record, which is thought to represent SST. Therefore, the $\delta^{18}O$ record represents for a large part SST variability.

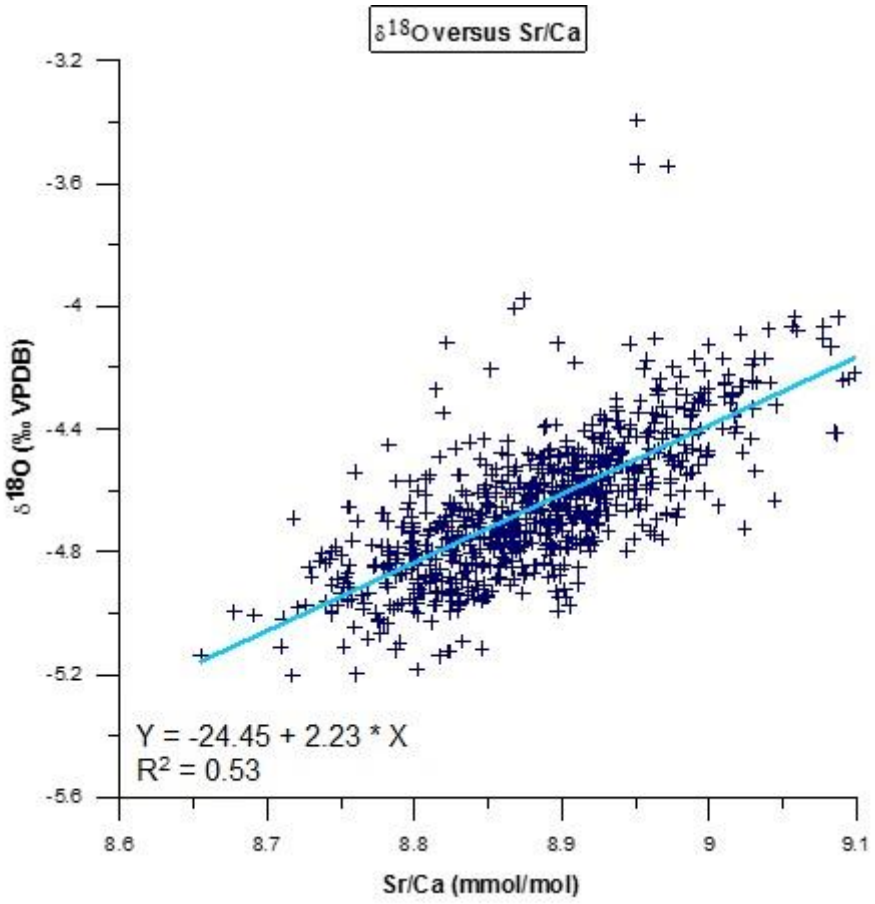

Figure 5.1. The $\delta^{18}O$ record set against the Sr/Ca record.
The correlation between $\delta^{18}O$ and Sr/Ca. A linear trend line is plotted that represents the relationship between the two, the characteristics of the trend line are displayed in the lower left corner. Number of data points in the graph is 781.

A histogram of the $\delta^{18}O$ record was made in order to check the data and to see if the data is normally distributed, see Figure 5.2. The black line in the graph is a normal distribution fit and corresponds nicely with the $\delta^{18}O$ data, consequently it can be concluded the data is normally distributed. Looking in more detail to the histogram, it is evident that the slopes of the histogram are not perfectly equal. The side towards more negative values (left side) has a steep slope, while the side towards more positive values (right side) has a more gradual and distributed slope (with a steep slope around the value -4.5‰). More negative $\delta^{18}O$ values indicate higher SST. The mean variation between more negative and more positive values in the $\delta^{18}O$ record is mainly caused by seasonal variations. More negative values of $\delta^{18}O$ indicate warmer SST and are therefore interpreted to represent summer data. For that

reason, data on the left side in the histogram is considered as summer data and data on the right side as winter data. Consequently it can be concluded that $\delta^{18}O$ values from winter months (colder) show more spreading than $\delta^{18}O$ values from summer (warmer) months. It is also possible that there is some sort of bi-stability present in the data records: two normal distributed histograms that largely overlap, might show an almost similar histogram image.

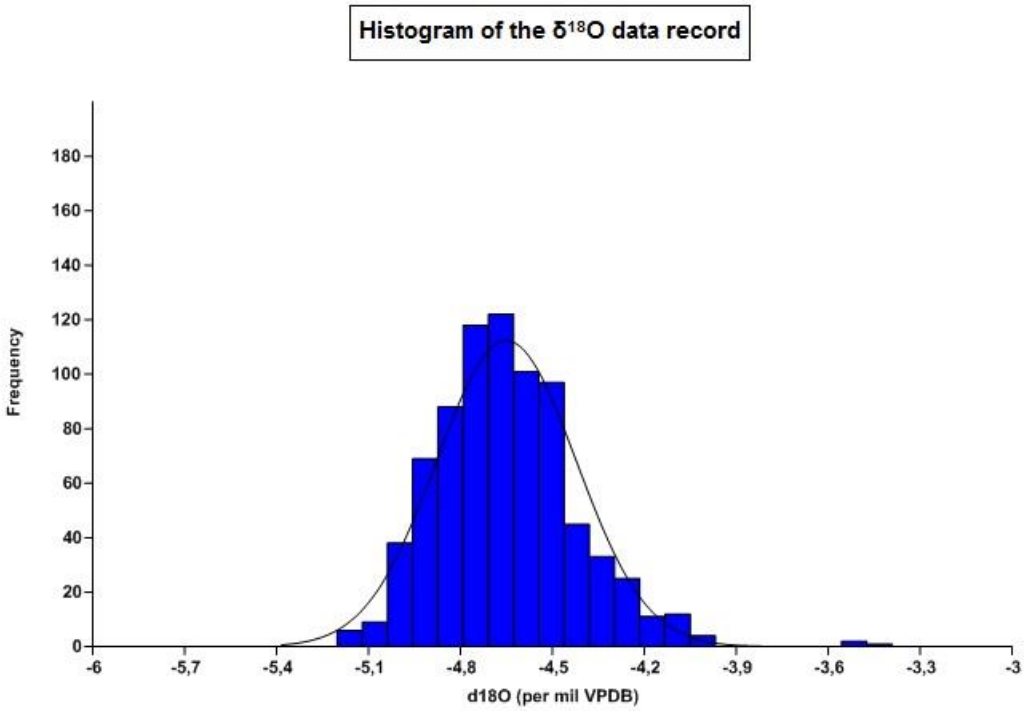

Figure 5.2. Histogram of the $\delta^{18}O$ data record. The black line is a normal distribution fit.

5.2. Reconstruction of SST

Sea surface temperatures can be calculated from the Sr/Ca record (see Methods section 3.4.1). Figure 5.3 displays the calculated SST's from coral core Darwin Long. The lower panel is the local reconstructed SST record by the use of the regression equation: Sr/Ca = 10.196 – 0.0502 · SST. The Sr/Ca data was evenly resampled to a monthly resolution, to permit a monthly comparison of the SST record derived by corals to instrumental SST records.

The intervals relating to positive excursions in $\delta^{18}O$ and higher values of Sr/Ca, are also visible in the displayed SST record (Figure 5.3). At the beginning of the record, around 1870-1885, the temperatures seem to be a bit lower compared to the rest of the record. Then from 1935 to 1970 it looks like there are some cycles present with temperatures fluctuating between higher and lower values in around ten years. Three of these cycles can be distinguished.

The last 60 years of the coral derived SST record (light blue) is compared to the ERSST dataset (purple) and SST AIMS Composite (red) records in the upper panel of Figure 5.3 (see also Section 3.3.). Within this smaller time frame it is visible that the small scale variations are seasonal variations represented by a cycle of a year. The more regional ERSST signal shows less amplitude SST variations than the reconstructed SST, which could be due to the fact that local SST changes more than regional signals (R^2=0.33 over this 60 year time interval). During periods where the local reconstructed SST varies more, for example the periods ~1950-1960 and ~1962-1974, the ERSST also shows larger variations. On the other hand, small periods where amplitude variations are small, around 1960, 1975 and 1990, ERSST and local reconstructed SST match good. The overall coherence between the two records also becomes better after around 1985. For the last few years of the record local SST is available from

AIMS temperature loggers. The timing of the variations match nicely between the reconstructed SST and the AIMS SST data (R^2=0.51), but the amplitude variations of the reconstructed SST are larger. For example, around 2006 is a sharp peak towards lower SSTs that is not present in the local AIMS SST data.

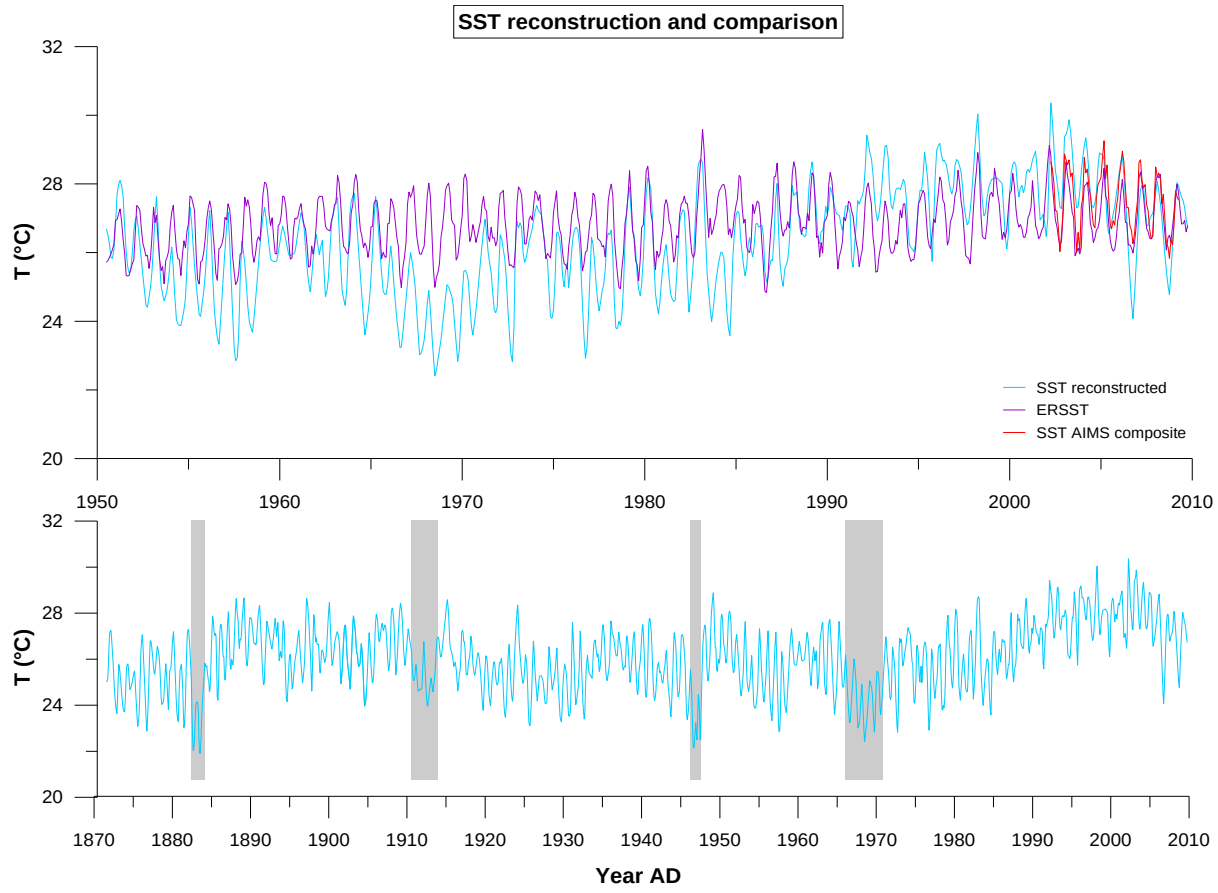

Figure 5.3. A reconstruction of the SST and comparison to other SST datasets.
Lower panel of the graph represents the reconstruction of the SST using the Sr/Ca record and the regression equation that defines the relationship: Sr/Ca = 10.196 – 0.0502 · SST. The Sr/Ca record which is resampled to an evenly monthly distribution is used for calculations. The grey rectangles indicate distinct events designated in Chapter 4. The upper panel shows in light blue the same SST reconstruction as the lower panel, but only from 1950 to 2009, plotted together with the ERSST and SST AIMS composite SST records.

Absolute SST reconstructions yield a large error. Therefore it could be better to reconstruct relative SST, which is not influenced by large uncertainties in the Sr/Ca-SST calibration (Nurhati et al., 2011). Relative SST is calculated by subtracting the average annual seasonal cycle (time period 1961-1990). In Figure 5.4 the Sr/Ca-derived SST anomaly is plotted together with the ERSST anomaly.
Comparing the anomalies of the Sr/Ca-derived SST and ERSST was thought to improve the correlation by reducing the error. The comparison of the anomalies is displayed in Figure 5.4. The time period of 1950 to 2010 is plotted, since the ERSST data becomes less reliable with increasing age. The correlation between the two records is not very significant between 1950 and 2010 (R^2=0.17) and shows some clear deviations. The correlation of the anomalies is even smaller than the comparison of absolute temperatures, see above, which is striking and unexpected. First clear deviation between the two records is the much larger amplitude in the Sr/Ca-derived SST than the amplitude of the ERSST. Furthermore, the local temperature was almost 3 °C higher than the regional temperature anomaly around 1990-2005. The cooling around 1965-1970, indicated as the fourth event, is present in the local temperature, but not in the regional ERSST record.

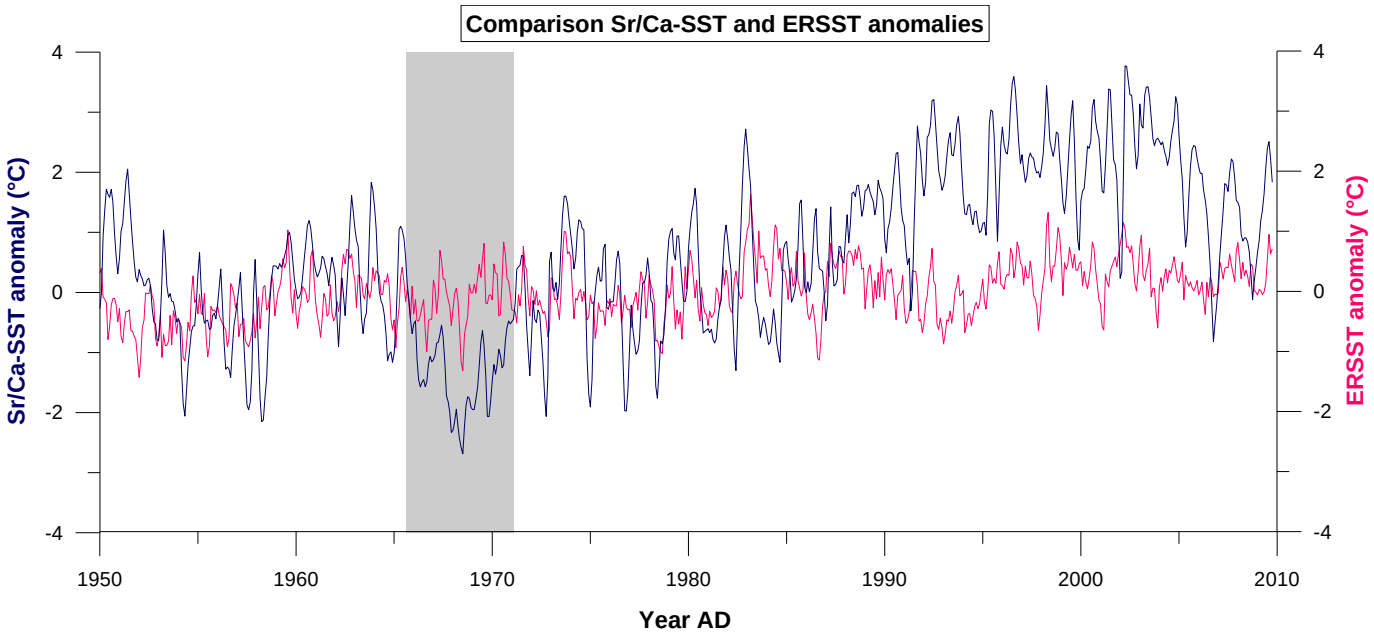

Figure 5.4. A comparison of the Sr/Ca-derived SST (blue) and ERSST (pink) anomalies.

5.3. Reconstruction of $\delta^{18}O_{SW}$

The $\delta^{18}O$ composition of the surrounding seawater ($\delta^{18}O_{SW}$) can be reconstructed by using a paired $\delta^{18}O$ and Sr/Ca approach (see also Methods section 3.4.2). We calculated the $\delta^{18}O_{SW}$ using two different methods in order to double check our results; a method based on the study of Ren et al. (2002) and the method of Weber & Woodhead (1972). Both reconstructions are shown in Figure 5.5. The calculation based on the method of Ren et al. (2002) is thought to represent the more accurate $\delta^{18}O_{SW}$ value. The method of Weber & Woodhead (1972) is used to check the results, because it assumes a major simplification by disregarding variations in $\delta^{18}O_{SW}$ (discussed in Section 3.4.2.2.). Comparing both calculations in Figure 5.5, indicates that the $\delta^{18}O_{SW}$ based on either of the two approaches gives similar results. No major discrepancies are demonstrated, supporting the reliability of the calculation based on either of the two methods.

The reconstruction of the $\delta^{18}O$ contributions in the coral core Darwin Long using the method Ren et al. (2002) is displayed in Figure 5.6. Figure 5.6A is the final reconstruction of $\delta^{18}O_{SW}$ and Figure 5.6B shows the instantaneous changes of $\delta^{18}O_{coral}$, $\delta^{18}O_{SST}$ and $\delta^{18}O_{SW}$. The most striking features presented in Figure 5.6A are the relatively high amplitude variations from 1870-1885, a (small) positive excursion around 1910, a very strong positive excursion around 1965 and relatively small amplitude variations near the end of the record starting from around 1985. The very strong excursion near 1965 is present both in SST and in $\delta^{18}O_{SW}$, but is much more pronounced in the $\delta^{18}O_{SW}$ record so salinity variations might play a very big role in this event.

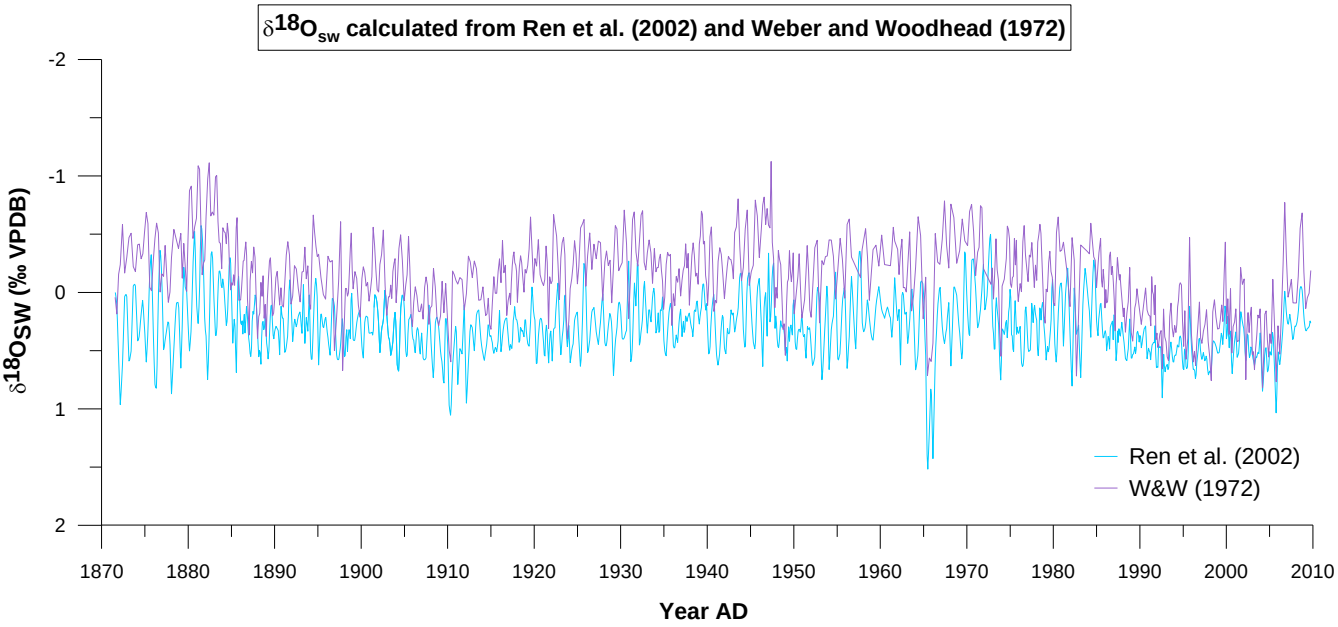

Figure 5.5. Reconstruction of $\delta^{18}O_{SW}$ using the method of Ren et al. (2002) and the method of Weber & Woodhead (1972).

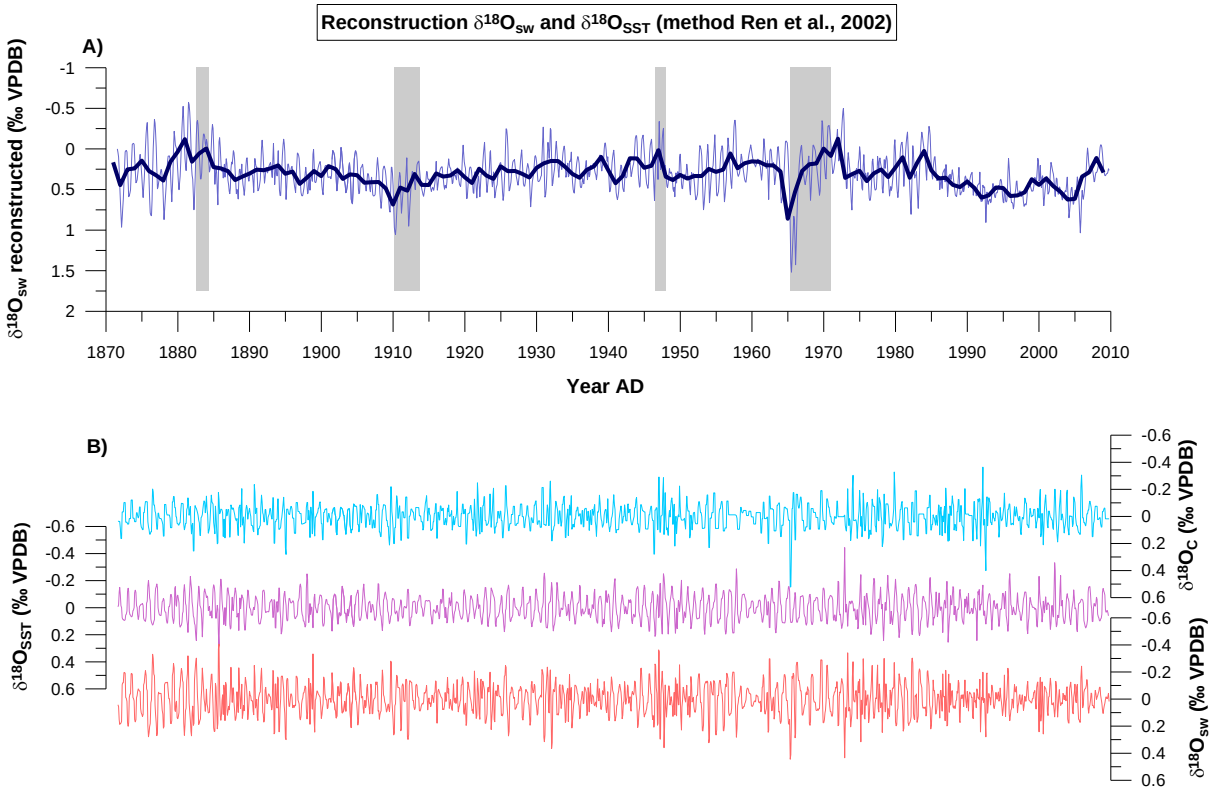

Figure 5.6. Reconstruction of $\delta^{18}O_{SW}$ and instantaneous changes of $\delta^{18}O_{coral}$, $\delta^{18}O_{SST}$ and $\delta^{18}O_{SW}$.
A) Reconstruction of the $\delta^{18}O_{SW}$. Dark blue line is yearly average. The grey rectangles indicate distinct events designated in Chapter 4. B) The light blue curve represents the instantaneous change of $\delta^{18}O$ in the coral aragonite. The purple curve is the instantaneous $\delta^{18}O$ variation caused by fluctuations in SST. The pink curve is the instantaneous difference in $\delta^{18}O$ originating from differences in oxygen composition of the surrounding seawater.

5.4. Spectral analysis Sr/Ca and oxygen isotope records

5.4.1. Power spectra

To identify present cycles in the Sr/Ca and oxygen isotope records, REDFIT analyses is carried out to make power spectra. On the x-axis the frequency of the cycle is displayed and on the y-axis the power/strength of the cycle is shown. To assess the significance or likeliness of the identified frequency the 95% significance level is plotted. The numbers in the graph indicate the length of the period of the corresponding peak in years.

Figure 5.7, 5.8 and 5.9 are the power spectra of the ENSO, IOD and PDO records. These power spectra are made to establish the cyclicity of these phenomena and to use this knowledge in the next step of identifying and interpreting cyclicities in our data records of Sr/Ca, $\delta^{18}O$ and $\delta^{18}O_{SW}$. The periods found in the power spectra are compared to the established cyclicities in literature. The timeframe of both IOD and ENSO records are taken similarly to our reconstructed data records, covering the period of around 1871-2009. The timeframe of the PDO record is from 1900 to 2009.

The four most prominent cycles that can be distinguished in the power spectrum of the ENSO (Figure 5.7) have the periods of 5.76, 3.54, 2.88 and 2.34 years. So the periodicity of the ENSO cycle varies roughly between 2 and 6 years. According to literature the ENSO has a period varying between 2-7 years (McPhaden et al., 2006). So the periods found in the power spectrum matches quite well with the literature, but in the power spectrum the smaller period cycles are more pronounced.

The periodicity of the IOD is harder to distinguish, since the power spectrum shows less prominent peaks. The only relatively sharp peak present that crosses the 95% significance line, has a period of 1.89 years (frequency of 0.53). There are some other smaller peaks present, which have periods around the annual cycle (~0.7-1.2 year) or half the annual cycle, seasonal (~0.5 year). Since the periodicity of the IOD is not very clear it will be hard to distinguish the IOD in our data records. Also, the most prominent period peak that is present in the power spectrum of the IOD is roughly similar to a period of the ENSO of around 2 years, which is just established. According to literature the period of the IOD varies between around 2-5 years. This is quite different from this power spectrum that indicates smaller periods.

The PDO index record shows a cyclicity more on the decadal timescale. The longest period present has a length of 36.67 years, but since this cycle fits exactly three times in this time period it is likely that it represent resonant frequency instead of a true cycle. Other periods present have a length of 18.33 years, 9.17 years and 5.79 years. There is also a very small peak that just crosses the 95% confidence interval at a period of 1 year, but the power is not very strong. According to literature the PDO has cycles on multidecadal timescales, 50-70 years (Minobe, 1997) and on interdecadal timescales, 17-28 years (Meehl and Hu, 2006). The power spectrum does not show the longer multidecadal cycle periods of PDO and only two interdecadal periods of around 36 (which is doubted) and 18 years. Furthermore, there are some multiannual periods present with lengths of around 9 and 6 years. Thus the periods of the PDO are smaller in the power spectrum than established by literature.

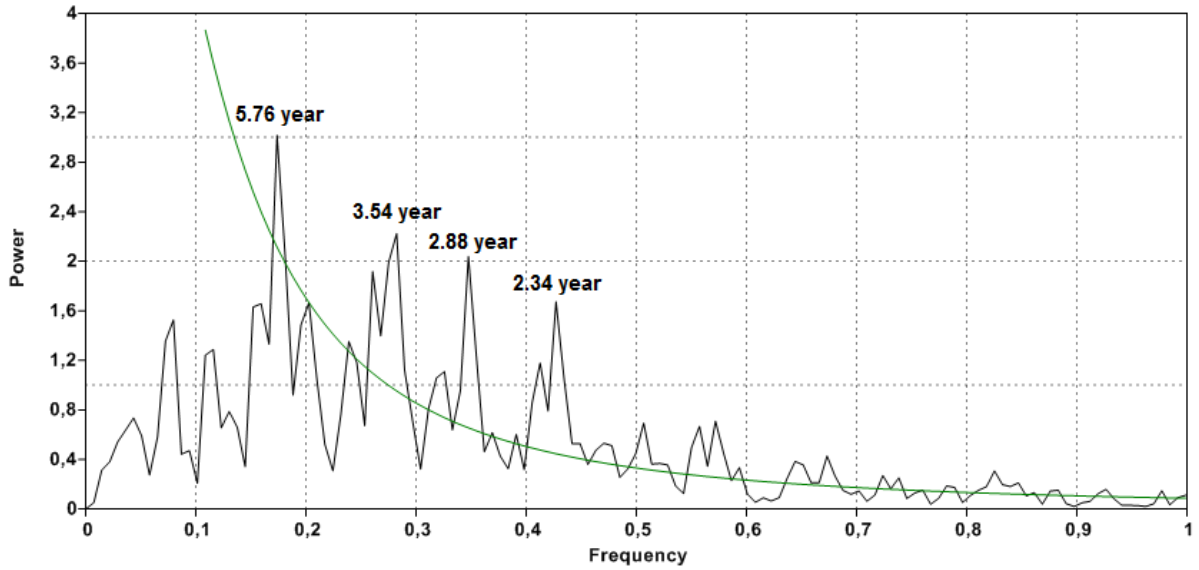

Figure 5.7. Spectral REDFIT analyses of the ENSO Nino 3.4 metadata record. On the x-axis, the frequency of the cycle is displayed and on the y-axis the power or strength of the cycle is displayed. The green line is the 95% confidence level.

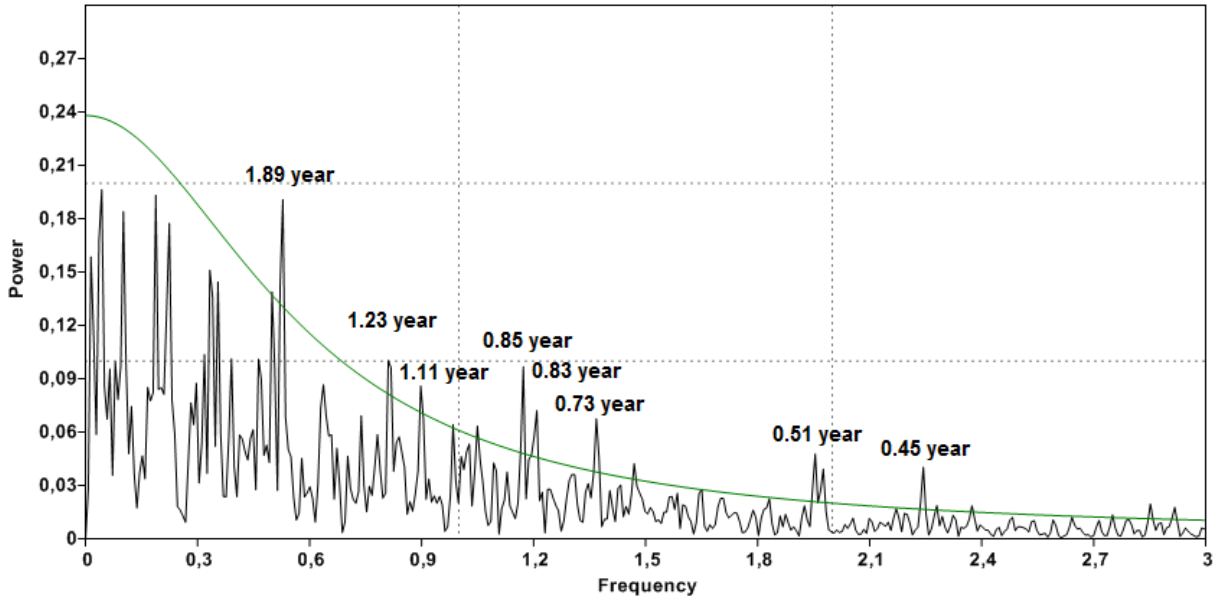

Figure 5.8. Spectral REDFIT analyses of the IOD DMI record. On the x-axis, the frequency of the cycle is displayed and on the y-axis the power or strength of the cycle is displayed. The green line is the 95% confidence level.

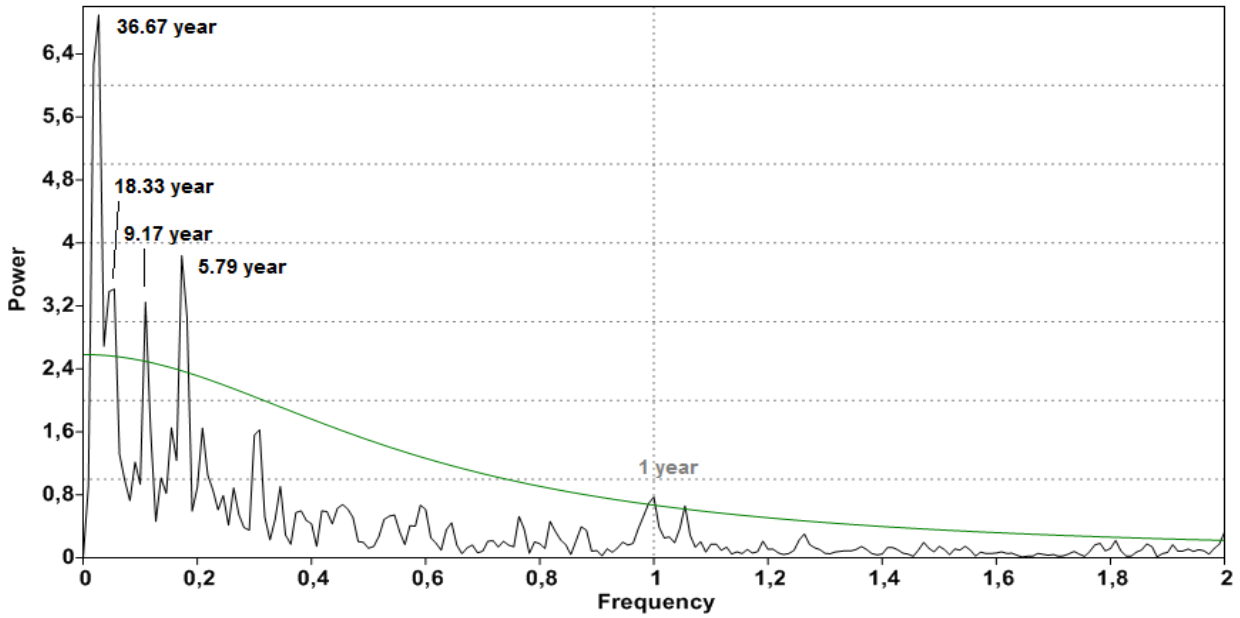

Figure 5.9. Spectral REDFIT analyses of the PDO index record. On the x-axis, the frequency of the cycle is displayed and on the y-axis the power or strength of the cycle is displayed. The green line is the 95% confidence level.

Next, the power spectra of our data records are made to see whether there is some form of periodicity present in our records and whether we can relate these periods to known climate phenomena. The power spectrum of the original (not resampled) Sr/Ca record is shown in Figure 5.10. There is one very prominent peak present with a period of 1 year, this peak represents logically the seasonal cycle that is very clearly visible in the data record. Besides, there are two other peaks present with periods of 46 and 10.6 years. Since the annual seasonal cycle is so prominent in the power spectrum, we also made a power spectrum of the yearly data record, see Figure 5.11. The same two cycles are present in this figure, but the 46 year cycle does not exceed the 95% significance line and the 10.6 year cycle only touches the 95% significance line. Thus the Sr/Ca record mainly shows cyclicity from the annual seasonal cycle, with perhaps some influence of a 10.6 year cycle but which is not very strong. The period of 10.6 years might be explained by the sunspot cycle. The strength of the sun varies with sun storms occurring in a cyclical manner, this influences Earth's climate with a dominant cycle of around eleven years. The influence of the sunspot cycle can also be traced in the upper ocean influencing SST (Cayan and Dettinger, 1997).

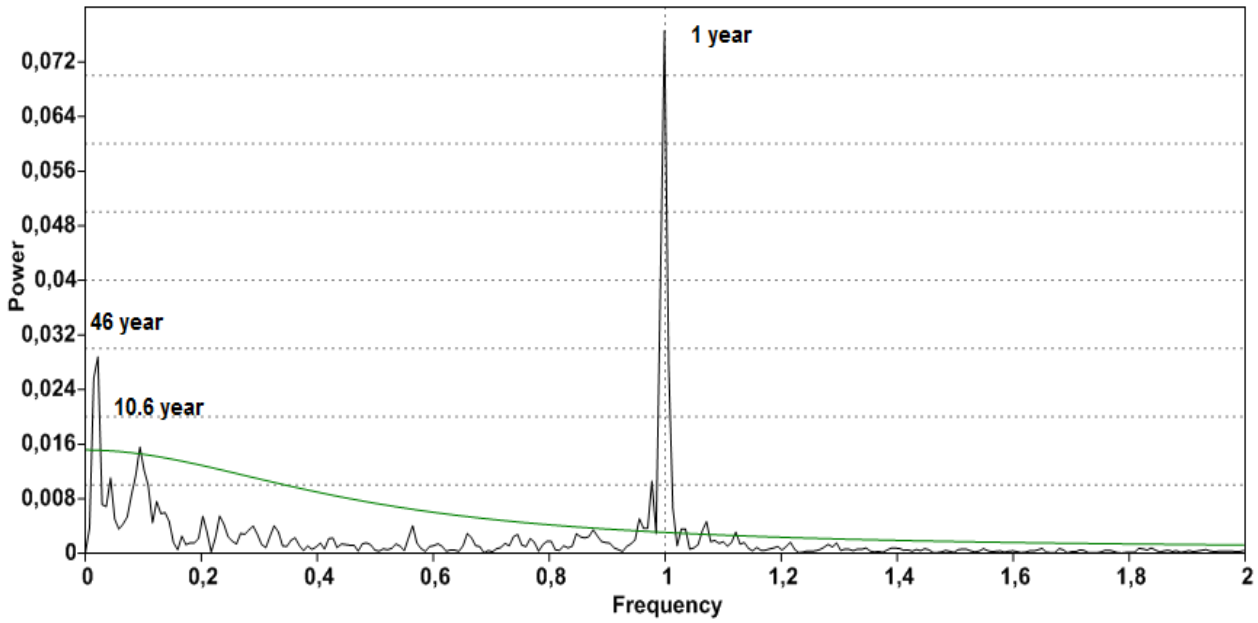

Figure 5.10. Spectral REDFIT analyses of the Sr/Ca record (not resampled). On the x-axis, the frequency of the cycle is displayed and on the y-axis the power or strength of the cycle is displayed. The green line is the 95% confidence level.

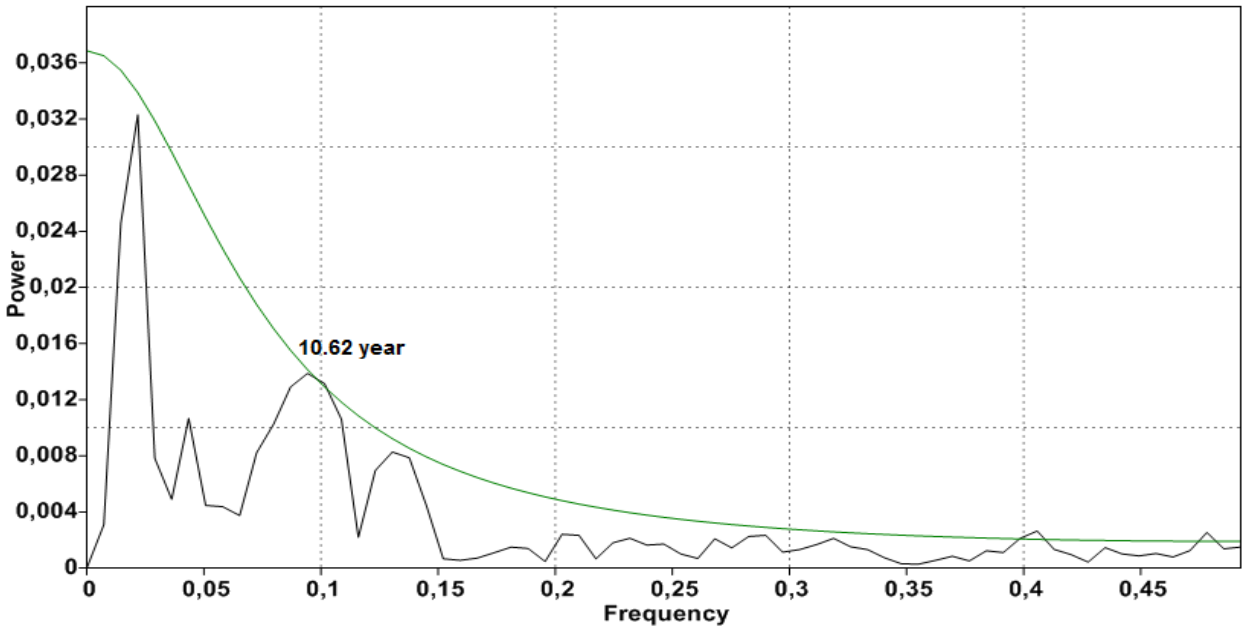

Figure 5.11. Spectral REDFIT analyses of the yearly Sr/Ca record. On the x-axis, the frequency of the cycle is displayed and on the y-axis the power or strength of the cycle is displayed. The green line is the 95% confidence level.

The power spectrum of the $\delta^{18}O$ record (Figure 5.12) shows the exact same periods as the Sr/Ca record. Only difference is that the annual cycle is a little bit less strong and that the 10.6 year cycle is larger in strength in the power spectrum of $\delta^{18}O$ compared to Sr/Ca. For this data we also made a power spectrum of the yearly data, see Figure 5.13. Again the 46 year cycle does not exceed the 95% significance line. However, there are two cycles around 10.6 year that do cross the significance line: 11.50 and 9.20 years. The 11.50 years cycle is most likely the 11 year sunspot cycle and the 9.20 years cycle matches closely to the 9.17 years cycle in the PDO power spectrum (Figure 5.9). The 9.20 year

cycle could also be the sunspot cycle, since the eleven year sunspot cycle actually shows periods between 9 and 14 years. In Figure 5.13 also a new small peak appears with period 3.94 years that just exceeds the 95% significance line. The power of this possible cycle is very small, so it is not very likely that is represents a significant cycle, but it is possible that is reflects the ENSO (or maybe IOD) variability.

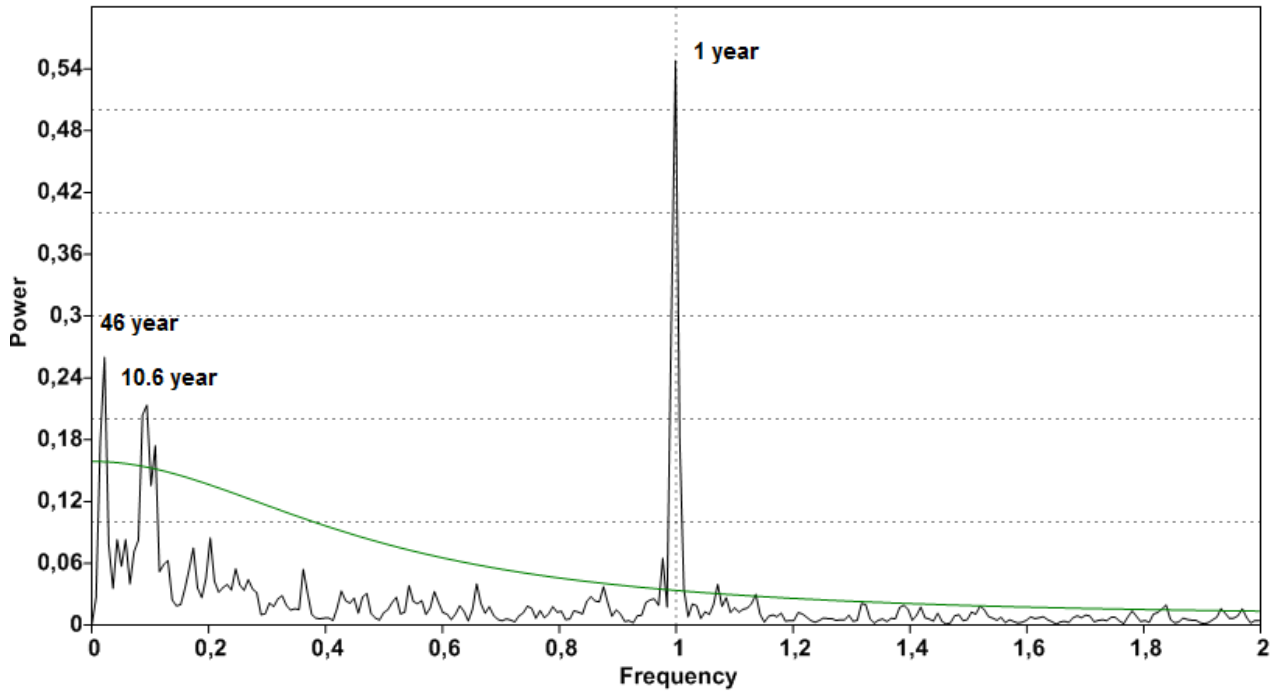

Figure 5.12. Spectral REDFIT analyses of the $\delta^{18}O$ record (not resampled). On the x-axis, the frequency of the cycle is displayed and on the y-axis the power or strength of the cycle is displayed. The green line is the 95% confidence level.

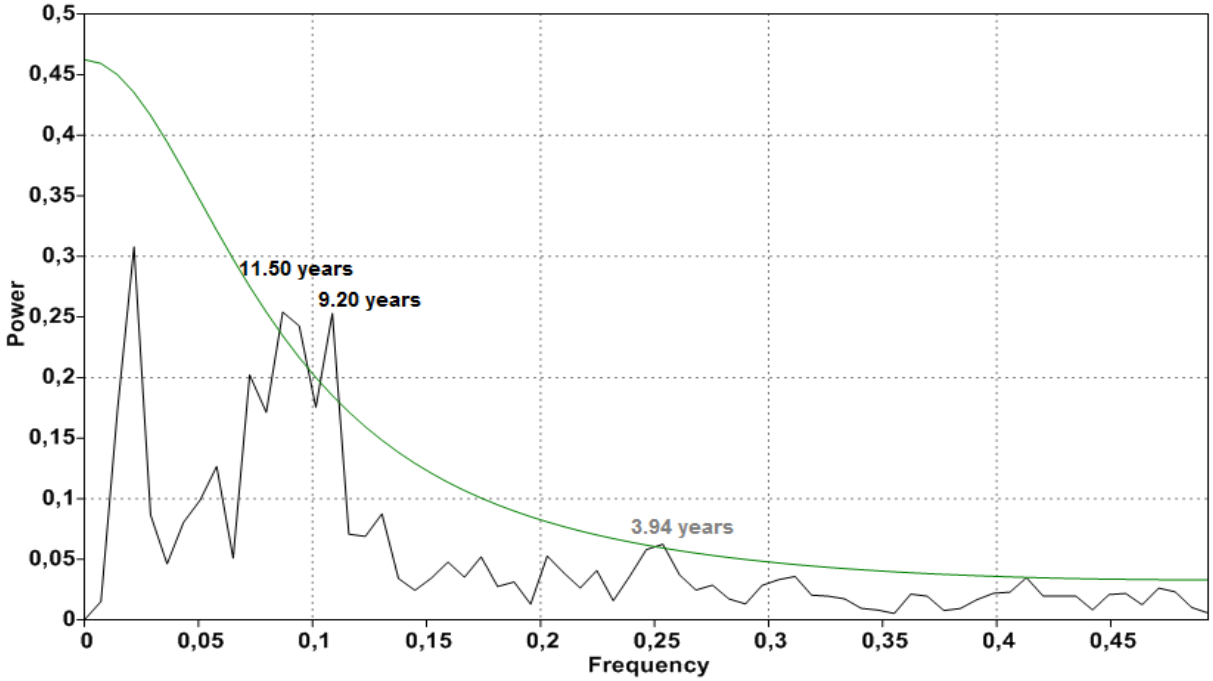

Figure 5.13. Spectral REDFIT analyses of the yearly $\delta^{18}O$ record. On the x-axis, the frequency of the cycle is displayed and on the y-axis the power or strength of the cycle is displayed. The green line is the 95% confidence level.

The power spectrum of $\delta^{18}O_{SW}$ is shown in Figure 5.14 and shows around the same periods of the power spectra of $\delta^{18}O$ and Sr/Ca. However, there are some small differences. So is the annual cycle extremely strong in this $\delta^{18}O_{SW}$ record with a power of 0.9. The other two periods that are present have smaller power compared to previous power spectra: these two periods do not exceed the 95% confidence level. The period of these cycles are 46 and 12.5 years. The latter being a bit longer than the periods of 10.6 years found in the $\delta^{18}O$ and Sr/Ca records. Also for $\delta^{18}O_{SW}$ a power spectrum of the yearly record is plotted, see Figure 5.15. The periods that cross the 95% confidence interval have lengths of 12.5 and 3.45 years. The 12.5 year cycle might be the sunspot cycle, but the length is somewhat larger. The 3.45 year period is possibly ENSO variability.

Finally, a power spectrum is made from $\delta^{18}O_{SW}$ data for the months March till June. It is chosen to make a separate power spectrum for these months, since the peaks of the $\delta^{18}O_{SW}$ record towards more positive values occur during these months and the most spread in data values is present towards more positive values. It might be possible that the variation in more positive values occur due to some processes acting during these months. The power spectrum is shown in Figure 5.16 and it is very clear that there is only an annual cycle present with periods varying between 0.93 and 1.25 years. The other data records showed annual cycles with only one peak, precisely at 1.00 years. In this seasonal record the annual cycle shows more variation.

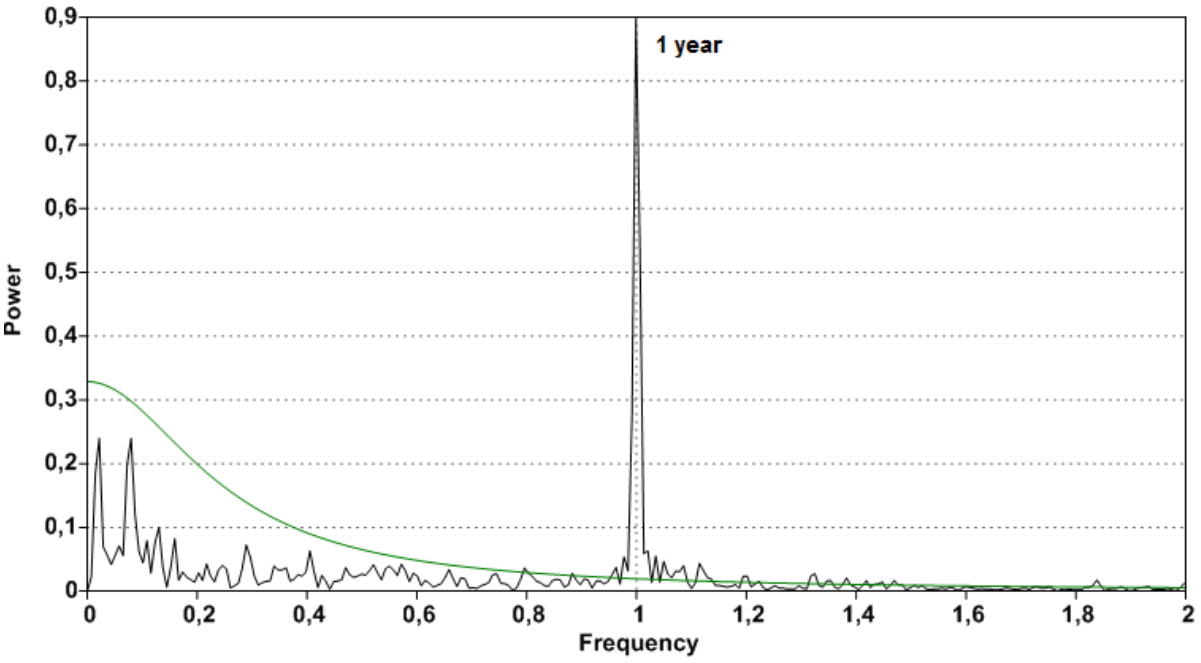

Figure 5.14. Spectral REDFIT analyses of the $\delta^{18}O_{SW}$ record. On the x-axis, the frequency of the cycle is displayed and on the y-axis the power or strength of the cycle is displayed. The green line is the 95% confidence level.

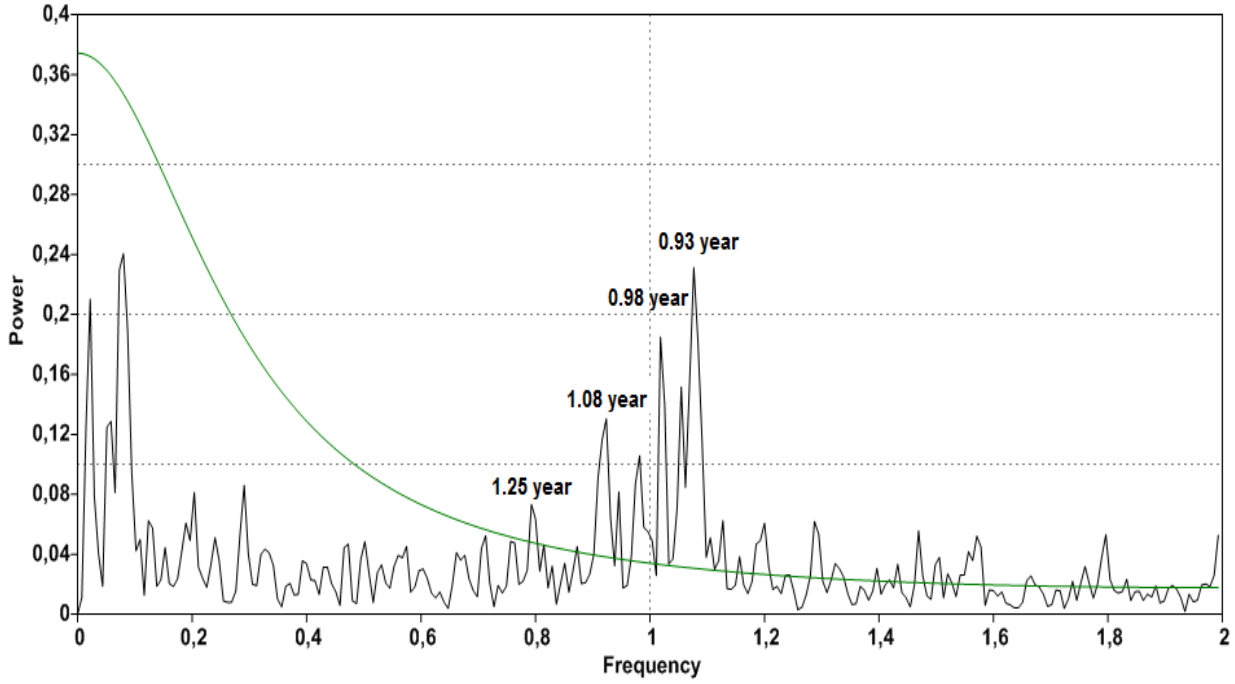

Figure 5.15. Spectral REDFIT analyses of the yearly $\delta^{18}O_{sw}$ record. On the x-axis, the frequency of the cycle is displayed and on the y-axis the power or strength of the cycle is displayed. The green line is the 95% confidence level.

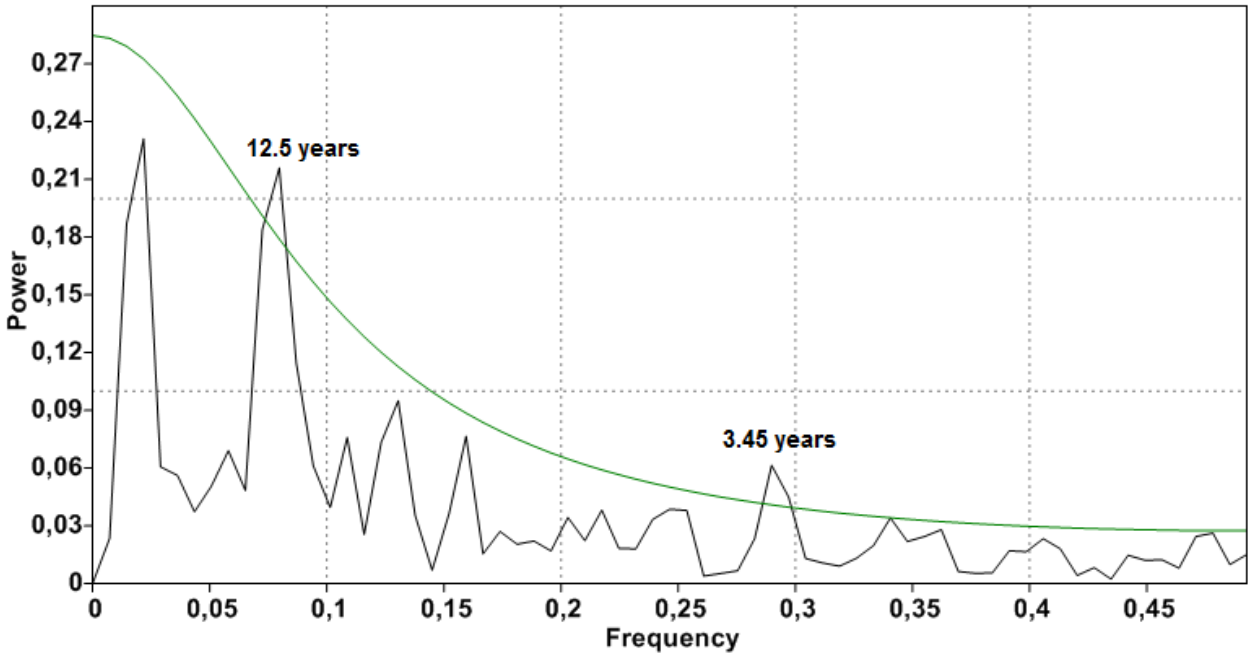

Figure 5.16. Spectral REDFIT analyses of the seasonal $\delta^{18}O_{sw}$ record (MAMJ). On the x-axis, the frequency of the cycle is displayed and on the y-axis the power or strength of the cycle is displayed. The green line is the 95% confidence level.

5.4.2. Wavelet transform and visible trends

In order to study how cyclicities vary in time, wavelet transforms are made for our different data records. Time is displayed on the x-axis and the length of the period is shown on the y-axis. The colors in the wavelet transforms indicate the strength of the period.

Figure 5.17 shows the wavelet transform of the Sr/Ca record. The first cycle that can be identified has a period of around 1 year and is thought to be the annual seasonal cycle. This cycle is moderate and quite consistent in strength over time. At some points in time the cycle is a little bit more pronounced, for example around 1885, 1945 and 1985 AD. The other clear cycle that is present has a period of approximately 10.6 years, which is thought to represent the sunspot cycle. This cycle is also present in the power spectrum of Sr/Ca. The period of this cycle is also constant, but the strength of the cycle varies strongly over time. The cycle is very weak to non-existent in the time period from 1900 to around 1925 AD, while it is relatively strong in the time period of 1945 till around 1970 AD. Beside these two cycles which can be easily distinguished, three possible cycles are identified centered on periods of 3 years, 7.5 years and 20 years. The 3 and 7.5 period cycles are characterized by strong variations in strength. The 3 year cycle is more pronounced around 1885, 1915, 1945 and 1985 AD. The 7.5 year cycle is stronger during the time periods 1910-1920, 1940-1955 and 1965-1975 AD. The variations in strength in the 3 and 7.5 period cycle occur almost simultaneously and they also seem to co-vary at some points with the strength variations of the annual cycle. The ENSO shows cyclicities with periods of around 2, 3, and 5 years, see Figure 5.7, therefore the 3 year cycle could possibly be the ENSO. According to literature the ENSO shows cyclicities with a 2-7 year period (McPhaden et al., 2006), making it possible that the found 7.5 year cycle could also represent ENSO variations. Finally, there is a cycle present with a period of around 20 years. This cycle is very constant in strength, which is weak to moderate. The period of the cycle seems to slightly decrease over time. This 20 year cycle could have different origins. The PDO has an interdecadal period of around 17-28 years (Meehl and Hu, 2006) and the powerspectrum of PDO (Figure 5.9) suggested a period of around 18 years. However, the sunspot cycle has besides the ~11 year period also an interdecadal period of 18-25 years (Cayan and Dettinger, 1997), which could also explain this roughly 20 year period.
The variations in strength in both the 1, 3 and 7.5 year cycle show some correspondence with identified possible events occurring around 1883, 1910-1915, 1946 and 1965-1970 AD. Therefore, it might be possible that the events are caused by certain cycles. In the next paragraph the origin of these events will be further explored.

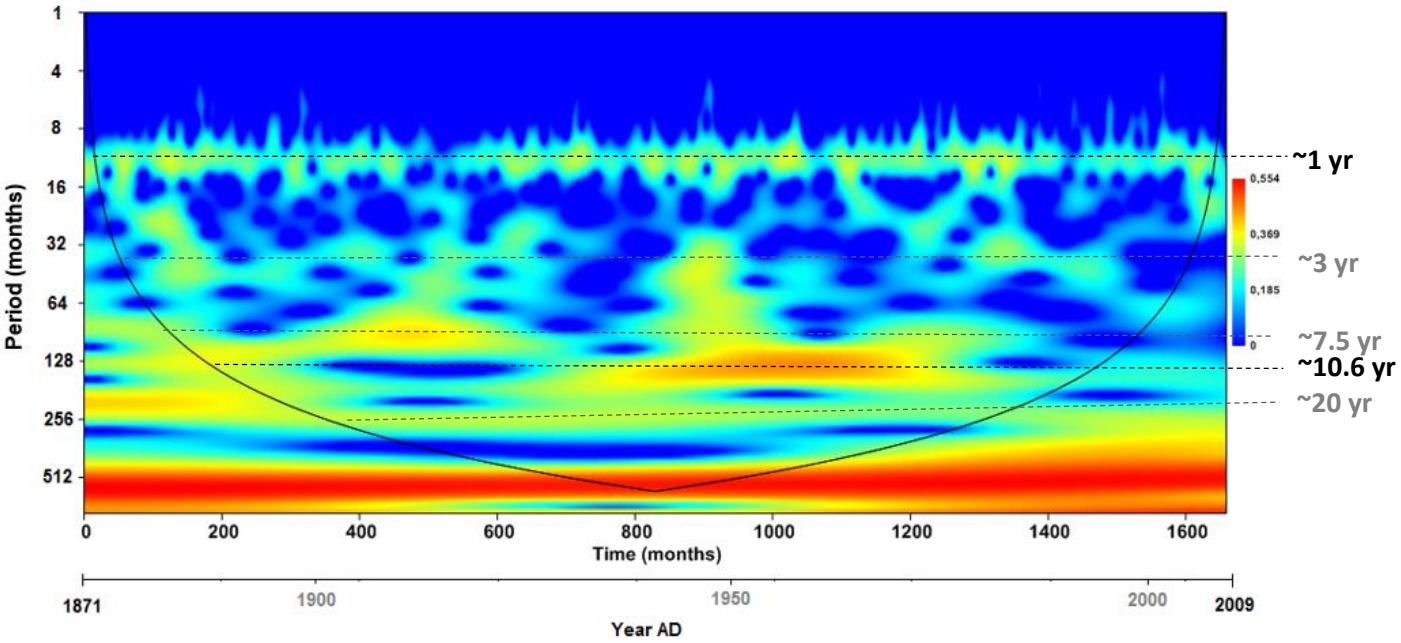

Figure 5.17. Wavelet transform for evenly monthly resampled Sr/Ca record. The x-axes represent time, the upper axis in months (0=1871.583 AD) and the lower axis in years, roughly. The y-axis shows the period of the cycle expressed in months. The dashed lines show identified cycles (black=very certain; grey=probably) with the corresponding period in years listed at the right. The black solid line indicates the cone of influence.

The next wavelet transform that is presented in Figure 5.18 is based on the $\delta^{18}O$ data record of the coral aragonite. This transform reveals the following four cycles, with periods around 1 year, 5 years, 10.6 years and 20 years, which will be separately discussed hereafter.
The one year cycle is again the annual seasonal cycle. The cycle is weaker expressed in the $\delta^{18}O$ record compared to the Sr/Ca record. Also the sunspot cycle of 10.6 year is visible, but this cycle is stronger expressed in the $\delta^{18}O$ record, and especially strong between 1950 and 1980 AD. Next, the 20 year cycle is also stronger in the $\delta^{18}O$ record. But also very striking and interesting is the fact that the period of this cycle is fairly constant from around 1940 to present with a ~20 year period, while the length of the cycle was smaller earlier in the record: it increases from an almost 10 year period (~1910) towards a 20 year period (~1940). Finally, a 5 year cycle can be distinguished, however this cycle is much harder to recognize. This cycle shows strong variations in strength, with relatively high influence around 1885, 1915 and 1945 AD.
There is one other feature that is striking in this wavelet transform: a yellow area at the time of 1965-1970 AD that extends from periods of roughly 1.5 to 5 year (~20-~64 months). This could be an ENSO event, since it shows the same periods and might also explain the identified event around 1965-1970 AD.

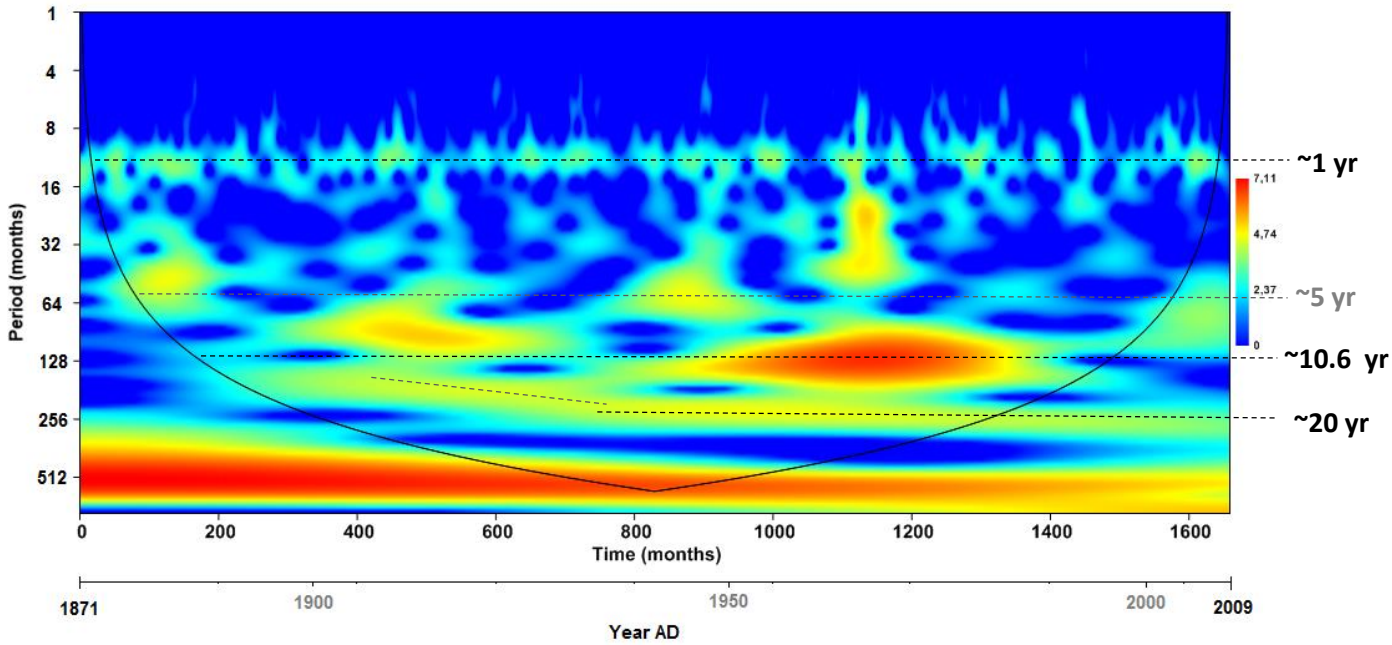

Figure 5.18. Wavelet transform for evenly monthly resampled $\delta^{18}O$ record. The x-axes represent time, the upper axis in months (0=1871.583 AD) and the lower axis in years, roughly. The y-axis shows the period of the cycle expressed in months. The dashed lines show identified cycles (black=very certain; grey=probably) with the corresponding period in years listed at the right. The black solid line indicates the cone of influence.

Also a wavelet transform is made from the $\delta^{18}O_{SW}$ data, since this is thought to correspond to SSS. The previous two wavelets of Sr/Ca and $\delta^{18}O$ looked quite similar, but the wavelet transform of $\delta^{18}O_{SW}$ looks very different, see Figure 5.19. Three cycles can be identified, two of them being very clear and one only poorly expressed. First clear cycle is the annual seasonal cycle. In the other two wavelet transforms, this cycle was quite uniform in strength and the period was closely centered at 1 year. In Figure 5.19 it is visible that the annual cycle in $\delta^{18}O_{SW}$ shows much more variations in strength and that the period of the cycle somewhat disperses towards periods shorter than 1 year. The period is strong in the beginning of the record from around 1871-1885 AD and has some strong variations in the period of 1960-1980 AD. Overall the annual seasonal cycle is much less consistent in the $\delta^{18}O_{SW}$ compared to the Sr/Ca and $\delta^{18}O$ record. Seasonal variations in $\delta^{18}O_{SW}$ are probably caused by the seasonal change of the ITCZ over the Indian Ocean, influencing precipitation patterns.
The other strong cycle present is the 10.6 year sunspot cycle. The period is constant over time, but the strength of the cycle varies. The power of the cycle is weak in the first part of the record, extending till around 1940, afterwards the power becomes very strong.
Around a period of 5 years there is possibly a weak cycle present (mainly light blue). Only around the years 1940 and 1965 the strength increases. Final striking characteristic of this wavelet transform is a yellow/orange/red area around the time of 1965 AD extending from a period length of 1 year to ~11 years. A comparable yellow area was also visible in the wavelet transform of $\delta^{18}O$ (Figure 5.18), however much weaker and less pronounced. This timing matches one of the identified events in the chapter results, so there might be a relationship present.

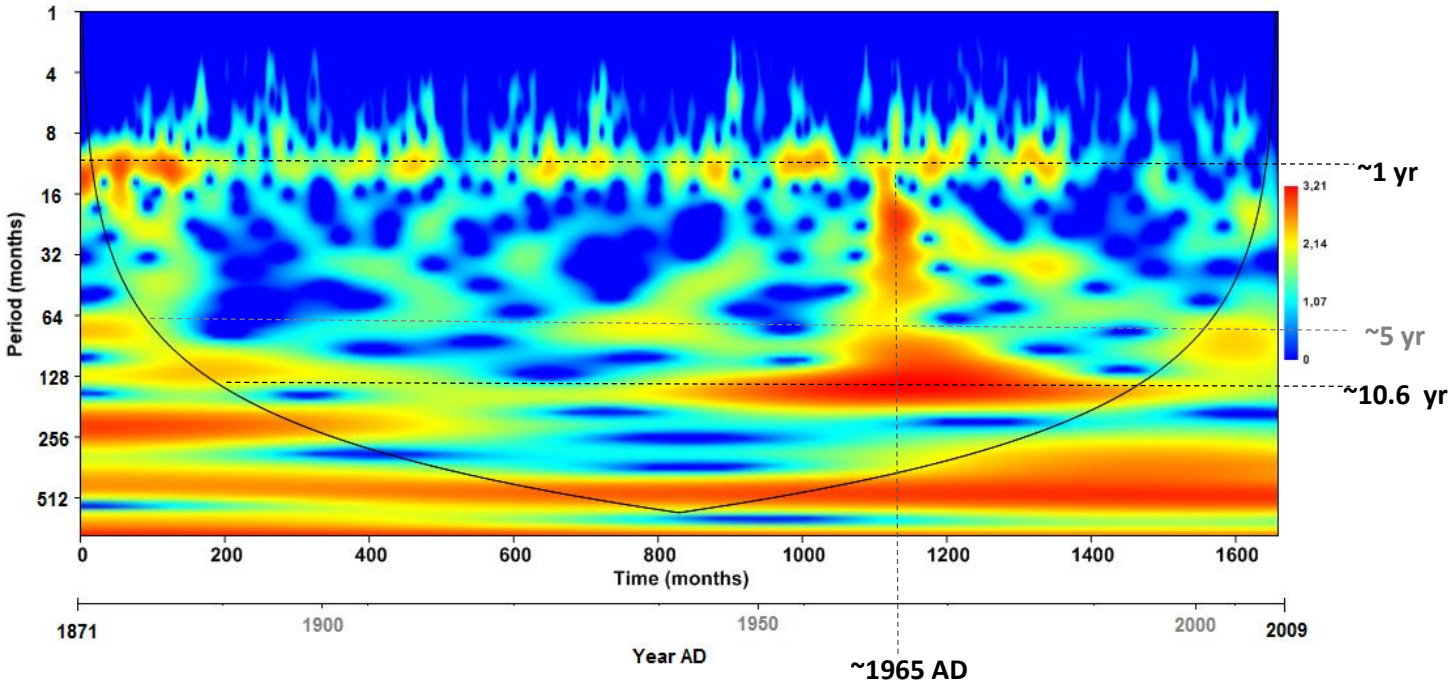

Figure 5.19. Wavelet transform for the calculated $\delta^{18}O_{SW}$ record. The x-axes represent time, the upper axis in months (0=1871.583 AD) and the lower axis in years, roughly. The y-axis shows the period of the cycle expressed in months. The dashed lines show identified cycles (black=very certain; grey=probably) with the corresponding period in years listed at the right. The black solid line indicates the cone of influence.

Periods of most cycles in the wavelet transforms are quite constant over time. Only the 20 year cycle present in the $\delta^{18}O$ record shows a trend with a lengthening of the period: from a nearly 10 year period around 1910 AD towards a 20 year period in 1940 AD. In the Sr/Ca and $\delta^{18}O_{SW}$ records the period of 20 years was constant through time. No other trends considering the length of periods are visible. But, the strength of cycles do vary over time. In all three records the 10.6 year cycle, interpreted as the sunspot cycle, is weakly pronounced in the earlier part of the records and becomes very strong from around 1940 AD onwards. There could be two explanations for this: the sunspot cycle became stronger from around 1940 AD, or the sunspot cycle got more pronounced at the coral site caused by external factors/mechanisms.

5.5. Changes in solar activity

With spectral analysis we found that the sunspot cycle is probably clearly expressed in our data records. This section researches the presence of the sunspot cycle in our data records into more detail. First we obtained a sunspot data record from Climate Explorer: a monthly reconstructed solar constant expressed in Total Solar Irradiance (TSI), which resembles Watt received per square meter surface.

We made a powerspectrum of the TSI data to determine the cyclicity of this dataset, see Figure 5.20. There is one very distinct peak present with a period of 10.58 years. No other peaks are present. This supports the hypothesis that the 10.6 year cycle present in both the powerspectra and the wavelet transforms of the $\delta^{18}O$ and Sr/Ca records represents the sunspot cycle.

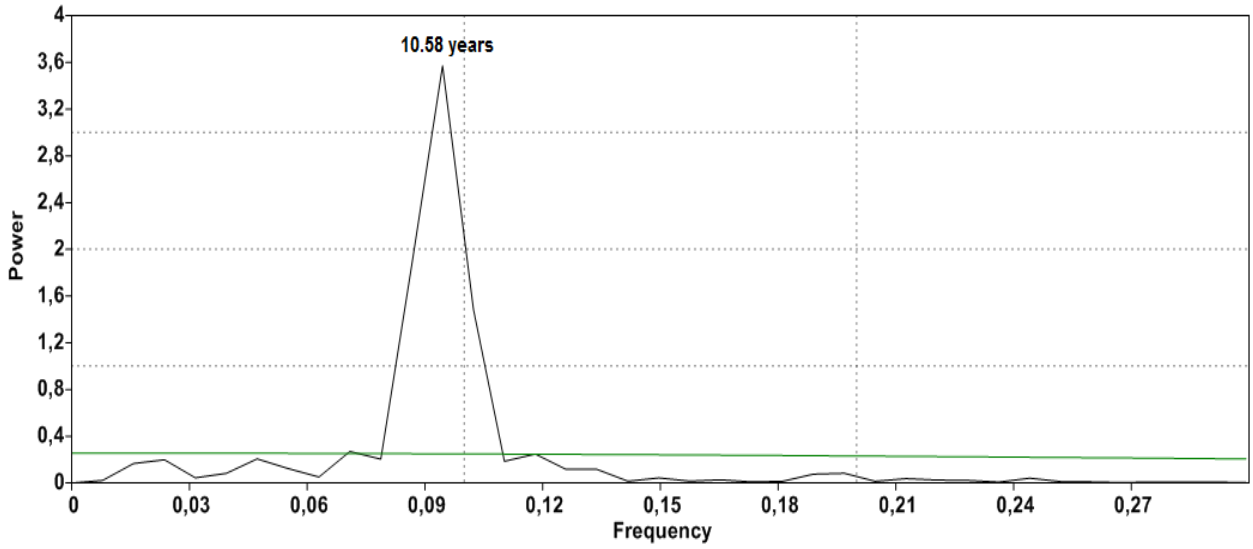

Figure 5.20. Spectral REDFIT analyses of the TSI record. X-axis determines the frequency of the present cycle and the y-axis indicate the power/strength of the present cycle.

Furthermore, the TSI record is compared to our data records of Sr/Ca, $\delta^{18}O$ and $\delta^{18}O_{SW}$, see Figure 5.21. The graph shows that all three records show high correspondence with the TSI record and thus that the sunspot cycle influences the records. The correspondence is highest in the time period of around 1905 AD to around 1985 AD. Before and after these times, multiple variations in the records do not match in sign. Especially the $\delta^{18}O$ and $\delta^{18}O_{SW}$ record show large similarities with the TSI record. The correspondence between the Sr/Ca record and the TSI record is less clear. These observations might lead to the conclusion that the sunspot cycle has a strong influence on the $\delta^{18}O_{SW}$ record and therefore salinity.
As a next step the sunspot cycle was filtered out of the different data records. The period of the cycle that is present in both the power spectra (Section 5.4.1.) and the wavelet transforms (Section 5.4.2) is 10.6 years. The sunspot cycle is filtered out of the data records around frequency 0.94 and with a bandwith of 0.015, this covers the range of a period between 9.17 and 12.66 years. Figure 5.16 shows filtering of the sunspot cycle out of different records and comparisons of the filtered sunspot cycles to the data records. The TSI record is compared to the sunspot cycle filtered out of the $\delta^{18}O$ data and shows high correspondence. In the first part of the record variations occur almost simultaneously in time, but from around 1945 the filtered sunspot cycle starts to lag the TSI record. It is highly possible that the sunspot cycle is recorded in the coral aragonite with a lag, another possibility for the offset are inaccuracies in the age model. Figure 5.22 also shows the Sr/Ca record together with a filtered sunspot cycle out of the Sr/Ca data, and the $\delta^{18}O_{SW}$ record together with a filtered sunspot cycle out of the $\delta^{18}O_{SW}$ data. These plots show that the sunspot cycle is visible in both records.

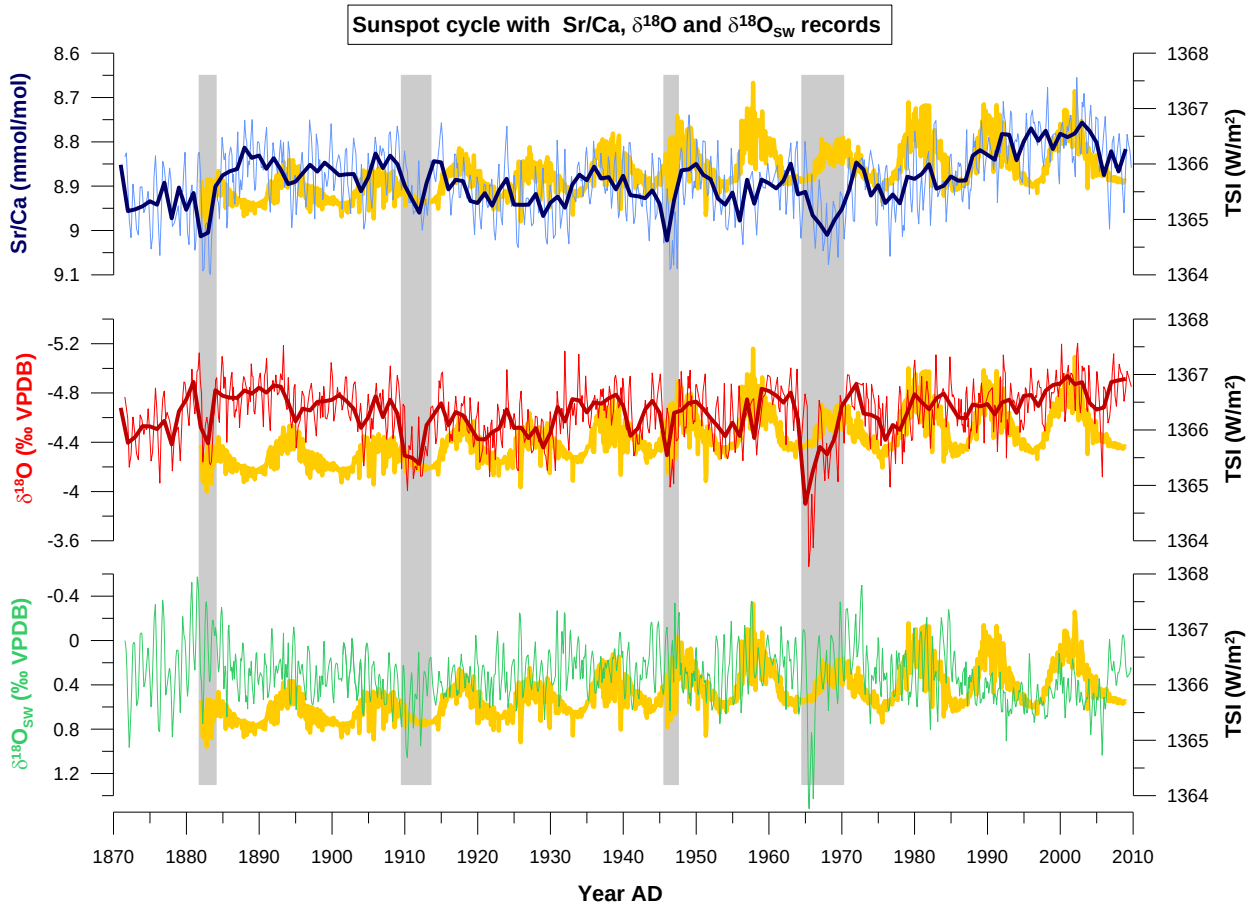

Figure 5.21. Our data records of Sr/Ca (blue), $\delta^{18}O$ (red), $\delta^{18}O_{sw}$ (green) plotted together with the TSI record showing the sunspot cycle.

In the wavelet transforms of the previous section we established that the influence (power) of the sunspot cycle increases from around 1940 AD. Also in Figure 5.22 we see that the amplitude of the filtered sunspot cycle increases from around 1940. In the TSI record we cannot see a clear increase in strength (Wm^2), but we can see a gradual and weak trend in the TSI record. This does not explain the sudden increase in strength from 1940, but possibly the TSI crossed a threshold value turning small increases into large increases.

Evidence seems quite strong that the sunspot cycle is recorded in our isotope proxy data and that the sunspot cycle has a considerable climate effect on the coral site at Cocos (Keeling) island. But the possibility that the cycle represents something else cannot be excluded. The power spectrum of PDO (Figure 5.9) showed that the PDO includes a cycle with a length of 9.17 years. Possibly the PDO had influence on the data records with a period of around 9-10 years. This is however just a possibility and cannot be supported by other evidence. No other climatic cycles or forcing factors are known to have a period of around 11 years and thought to be of influence in the coral data.
Another interesting point and further study area is how the sunspot cycle could influence the isotopic composition of the coral aragonite. With a depth of 5.8 meters is would be surprising that SST's change significantly from changes in the solar cycle.

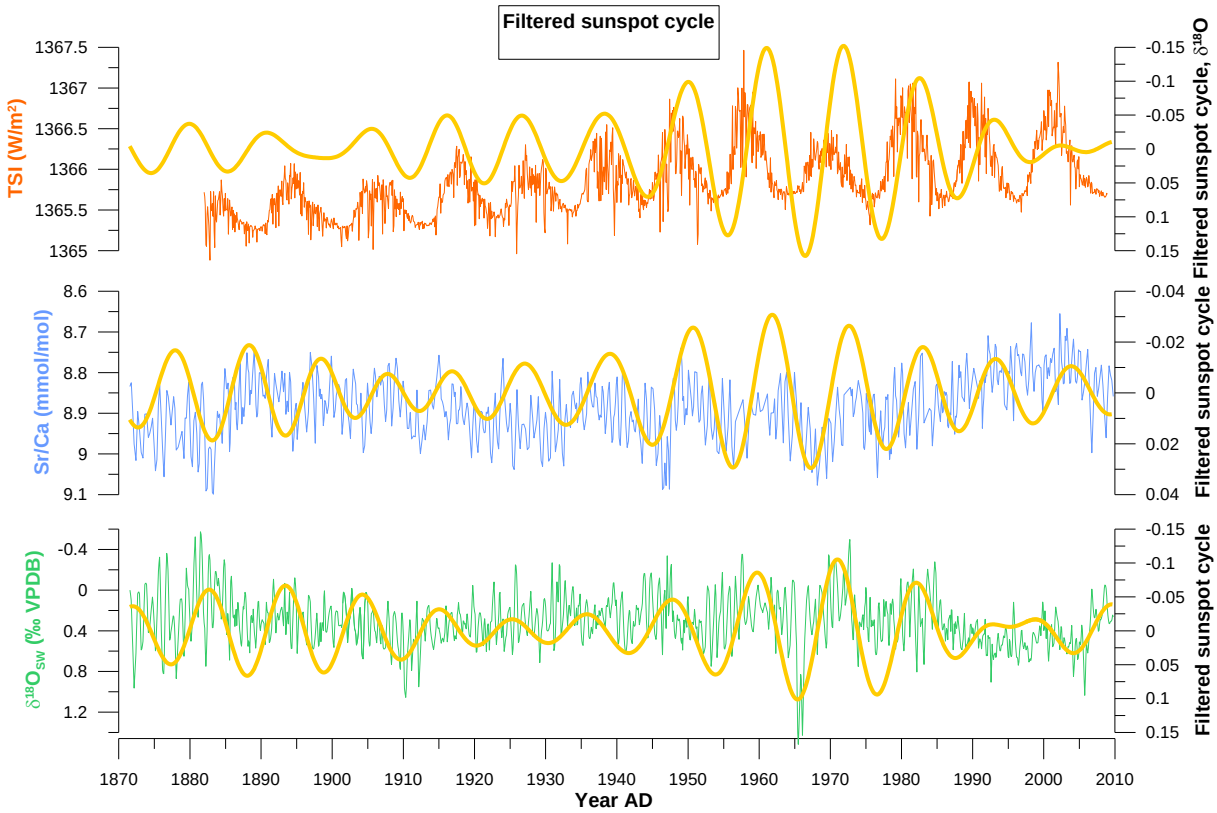

Figure 5.22. Filtering of the sunspot cycle compared to several different data records: TSI, Sr/Ca and $\delta^{18}O_{sw}$. Upper panel is the TSI record plotted together with a filtering of the sunspot cycle out of the $\delta^{18}O$ record. Below, the Sr/Ca and the $\delta^{18}O_{sw}$ record are displayed with a filtered sunspot cycle (out of the Sr/Ca and $\delta^{18}O_{sw}$ data). All sunspot cycles are filtered at a frequency of 0.094 and a window of 0.015.

5.6. Climate event linkage

5.6.1. Interpretation designated events

In the results (Chapter 4) four large peaks of multiple years towards more positive values were identified as events. The $\delta^{18}O$ values of these events were around 0.5-1.0 ‰ more positive and Sr/Ca values were up to 0.2 mmol/mol higher, see Figure 4.1; Results. In this section we try to link these events to climate phenomena and find the cause of these deviating events.

The 1883 event

A sharp peak towards more positive values is present in both the Sr/Ca and $\delta^{18}O$ records. This peak starts around 1882 and lasts till 1884 AD. During this event $\delta^{18}O$ values increase by around 0.5‰ and Sr/Ca values increase by around 0.1 mmol/mol. According to the relation defined by Epstein et al. (1953), for each 4.2°C temperature increase the $\delta^{18}O$ ratio decreases by 1‰. So the temperature decreases around 2°C during this event. This is supported by the defined regression equation between Sr/Ca and SST: Sr/Ca = 10.196 – 0.0502 · SST (see Methods section 3.4.1.).

Figure 5.25 displays the IOD and the ENSO signals. It is clearly visible that there is no clear IOD or ENSO signal present at the time of the first event, so the event must be caused by something else.

Possibly this event can be explained by a non-climatic phenomenon: a natural disaster. During the year 1883 the Indonesian volcano Krakatoa erupted with a giant force sending an enormous amount of fine ash and sulfate aerosols into the atmosphere. This volcano is located between the Indonesian islands Sumatra and Java and is only around 1155 kilometers from Cocos (Keeling) island, see Figure 5.23. The Krakatoa volcanic eruption had a major impact on the climate due to the large amounts of sulfate aerosols ejected into the atmosphere. The eruption column is thought to have extended 40-80

kilometers up into the air and a large tsunami followed (Rampino and Self, 1982). The climatic effect was recorded globally and also caused changes in the global ocean heat content (Gleckler et al., 2006; Rampino and Self, 1982). Figure 5.24 shows the temperature response of the oceans to volcanic forcing carried out by research of Gleckler et al. (2006). In 5.24B can be seen that global ocean temperatures decreased in the upper ocean after 1883 due to volcanic forcing according to computer simulations. Since Krakatoa and Cocos (Keeling) island are located relatively close, the climatic influence could be large at our coral site. There is however one uncertainty about this theory, since the event begins earlier, around 1882, before the volcanic eruption. Therefore it might be possible that there is also another process being active at this time, otherwise the age model contains a large error.

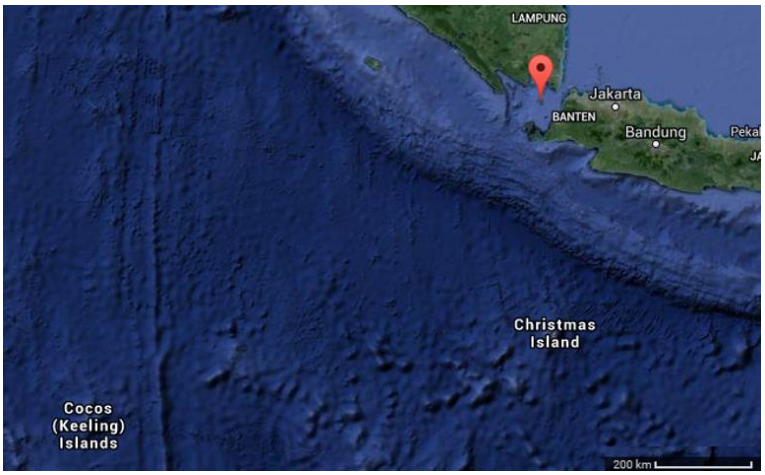

Figure 5.23. Location of the Krakatoa volcano (red mark) relative to Cocos (Keeling) island. Obtained from google maps.

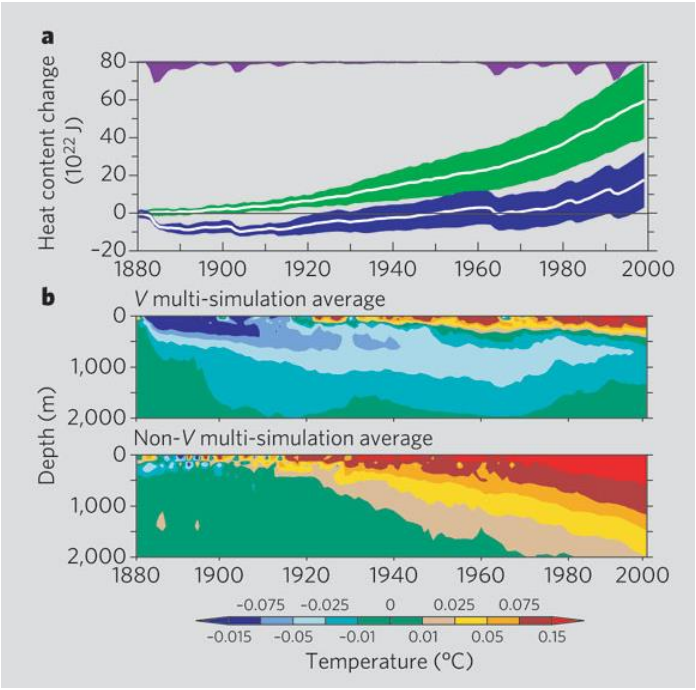

Figure 5.24. Ocean heat content simulations with and without volcanic forcing from 1880 to 2000. A) Change in ocean heat content with (blue) and without (green) volcanic forcing. The purple shading indicates an estimate of the amount of volcanic dust in the stratosphere. B) Global ocean-heat anomalies for two different simulations, with volcanic forcing (V) and without volcanic forcing (non-V). Obtained from Gleckler et al. (2006).

The 1910-1915 event

During this event $\delta^{18}O$ values increased with around 0.5‰ and Sr/Ca values with around 0.1 mmol/mol. Similar to the 1883 event this caused a cooling of around 2°C of the sea surface. The wavelet transform of Sr/Ca (Figure 5.17) showed a relatively strong period of around 7.5 years at this time. According to literature the ENSO varies between 2-7 years (McPhaden et al., 2006), so possibly there is a strong ENSO cycle present around 1910 AD. Figure 5.25 displays the ENSO occurrences and in this graph the ENSO shows a very negative peak around 1910 AD of around -2°C SST. A negative phase of the ENSO represents a La Niña and causes cooling in the eastern part of the Indian Ocean. This is what we also recognize in our $\delta^{18}O$ and Sr/Ca records. The state of the IOD, which is also displayed in Figure 5.25, shows us that around 1910 the IOD is in a negative phase with a value of around -0.75°C SST. This means that the eastern Indian Ocean is warmer than the western Indian Ocean. Simultaneously, the sunspot cycle experiences a minimum, see Figure 5.21. Such a minimum can cause further cooling in our records and possibly counter the effect of the negative IOD phase.

The 1946 event

This events shows again a similar variation in $\delta^{18}O$ and Sr/Ca values: $\delta^{18}O$ increases with around 0.5‰ and Sr/Ca values simultaneously increase with around 0.1 mmol/mol. Thus again a SST cooling of 2°C. In the wavelet transform of Sr/Ca (Figure 5.17) the power is relatively strong between the periods of around 3 till 7.5 year around 1965 AD. Furthermore, the wavelet transforms of $\delta^{18}O$ (Figure 5.18) and $\delta^{18}O_{SW}$ (Figure 5.19) show relatively high power at a 5 year period around the year 1965 AD. In Figure 5.25 can be seen that at this time the IOD is in a positive phase with values of around 0.75°C SST and that there is no strong ENSO present. Since this figure indicates that there is no ENSO signal present it would be unlikely that the periods present in the wavelet transforms are caused by ENSO, but these periods might be explained by the IOD. Furthermore, there is also a minimum in the TSI record which indicates the sunspot cycle, see Figure 5.21.
During the year 1946 some nuclear testing was carried out underwater at the Bikini atoll located in the Pacific Ocean. The influence of nuclear testing on oxygen isotope compositions of the ocean is not known, but might be of some influence. To research whether this nuclear testing could have contributed to the deviation in our data record, the effect of nuclear testing on ocean oxygen isotope composition should be researched.

The 1965-1970 event

The last event occurring around 1965 till 1970 is the strongest event with the sharpest peak present in the data records. The peak in $\delta^{18}O$ is present at the beginning of the event around 1965 AD, but the large peak in Sr/Ca values is occurring later in time, roughly around 1968 AD. During this event $\delta^{18}O$ values increased by 1-1.5‰ and Sr/Ca values increased with around 0.15-0.2 mmol/mol. These deviations in $\delta^{18}O$ and Sr/Ca values are around twice as high as the other three events and represent a SST warming of around 4°C.
Interesting to see is that the $\delta^{18}O_{SW}$ record shows a relatively very sharp peak towards more positive values (Figure 5.5), such a peak in $\delta^{18}O_{SW}$ values is not present during the other events. This peak is present at the beginning of the event. The wavelet transform of $\delta^{18}O_{SW}$ shows relatively strong power around 1965 AD between the periods of around 1-5 years, with the strongest period being around 2 years. The IOD also influences the precipitation pattern over the Indian Ocean, with less precipitation in the eastern Indian Ocean during a positive phase of the IOD. Variations in $\delta^{18}O_{SW}$ are thought to be caused by salinity changes and thus partly by changes in precipitation. At 1965 AD the $\delta^{18}O_{SW}$ record shows a sharp peak towards more positive values, this means that relatively less ^{16}O is present in the ocean water. Since precipitation is thought to be enriched in ^{16}O compared to ^{18}O (however only slightly at these tropical latitudes), precipitation decreased. This matches with a positive phase of the IOD. According to Figure 5.25, a relatively strong positive phase of the IOD occurred just before 1965 AD exceeding values of 0.75°C in SST, but is followed by a negative phase of the IOD at 1965 AD, so influence of the IOD is not very convincing. The ENSO does also not show convincing variability to be of influence (Figure 5.25). We consider an enormous amount of precipitation to cause the peak in

$\delta^{18}O_{SW}$, but the precipitation data from Cocos does not show any changes in precipitation around this time (Figure 2.5). Also no destructive tropical cyclones occurred at Cocos (Keeling) island. Maybe salinity changes were caused by another mechanism, such as changes in ocean advection. It could be possible that transport of ITF increased substantially, bringing ocean waters with more positive $\delta^{18}O_{SW}$ values to the Indian Ocean. Unfortunately, this theory cannot be supported by literature.
As discussed in the Introduction, large changes occur at the Chagos Archipelago around 1970 AD, since SST reaches a threshold value of 28.5°C turning on deep convection and changing the ocean-atmosphere system at this location. The timing of this event is around the same time, but at Cocos (Keeling) island we experience a strong cooling event of around 4°C. These are two opposite signals, which is a characteristic of an IOD event (Figure 2.4). But still the IOD is not very convincing in strength around this time, so it is difficult to say whether the IOD was capable of changing the climate so drastically.
Finally, the sunspot cycle experienced a minimum at 1965 AD, but afterwards the TSI increases from 1965 to 1970 event (Figure 5.21). So the sunspot cycle might be of influence triggering the event and causing the sharp peaks, but cannot explain the relative long length of the event. In Figure 5.22 the filtered sunspot cycle is displayed and this graph shows that the filtered sunspot cycle from $\delta^{18}O_{SW}$ matches perfectly with the sharp peak of 1965 AD. At this time the sunspot cycle is in a very strong negative phase.

Figure 5.25. Signals of the IOD and the ENSO. The grey rectangles indicate the timing of the specified events.

5.6.1. Tropical cyclones at Cocos (Keeling) island

Cocos (Keeling) island is located in an area frequently struck by tropical cyclones. In the time period of 1870 to present, the island is struck by six destructive cyclones. The timing of these cyclones are: January 28, 1876; February 4, 1893; March 4, 1902; November 27, 1909; January 1986 (called Doreen); February 1992 (called Harriet) (Bureau of Meteorology cyclone webpage, 2015). In the $\delta^{18}O$ record cyclones can cause negative excursions and deviations between the $\delta^{18}O$ and Sr/Ca record, since precipitation of these cyclones is thought to be enriched in ^{16}O causing the $^{18}O/^{16}O$ ratio to become more negative. The timing of the cyclones that are listed above are marked in the $\delta^{18}O$ record in order to study if these cyclones affected the $\delta^{18}O$ composition on site, see Figure 5.26. At the time of these cyclones, no sharp excursions are found and cyclones cannot be (easily) recognized in our record. Only the last occurring cyclone, in February 1992, occurred simultaneously with a relatively very negative value in the $\delta^{18}O$ record of -5.11‰. The cyclone events are also traced in the $\delta^{18}O_{SW}$ record since this records should represent salinity and thus also track precipitation variations, see Figure 5.27. Also the $\delta^{18}O_{SW}$ record shows no sharp excursions at times of cyclone events.

It must be noted that it is difficult to exactly link the timing of these cyclone events to the data records. The timing is dependent on the constructed age model and since the age model contains errors, this can influence the results by not assigning the correct age.

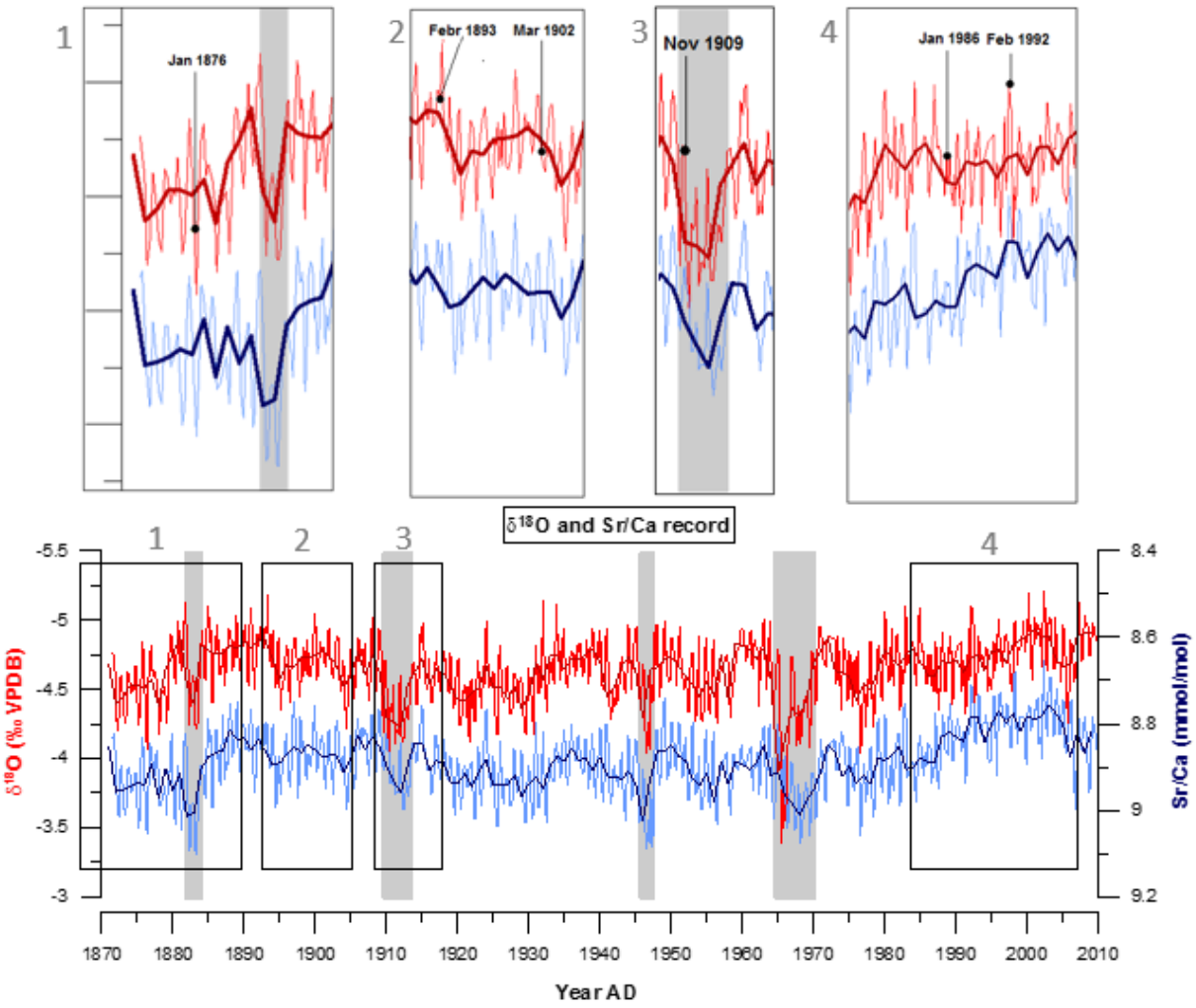

Figure 5.26. Relating destructive tropical cyclones at Cocos (Keeling) island to the $\delta^{18}O$ record. In the upper panels six major tropical cyclones that struck Cocos (Keeling) island are marked in the $\delta^{18}O$ record. These cyclones occurred in Jan 1876, Feb 1893, Mar 1902, Nov 1909, Jan 1986 and Feb 1992. These are more detailed cut-out regions of the lower panel, which shows the $\delta^{18}O$ and Sr/Ca records.

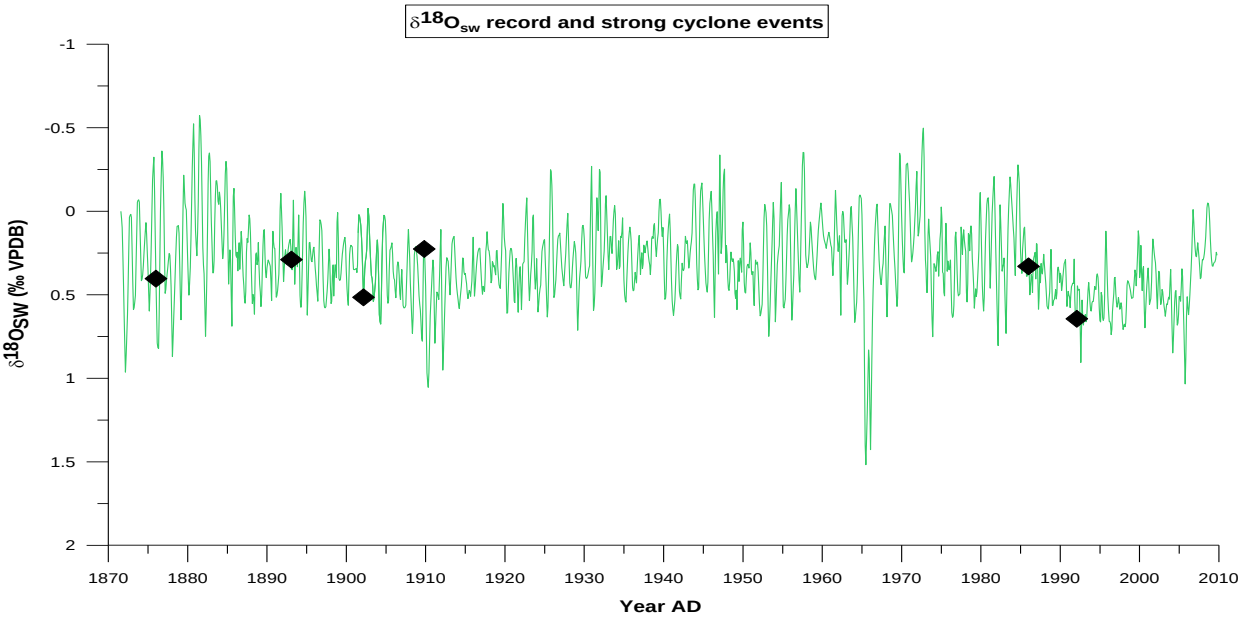

Figure 5.27. Relating destructive tropical cyclones at Cocos (Keeling) island to the $\delta^{18}O_{sw}$ record. The black symbols indicate the six strong cyclone events of Jan 1876, Feb 1893, Mar 1902, Nov 1909, Jan 1986 and Feb 1992.

5.7. Other proxy records: $\delta^{13}C$ and G/B ratio

Besides $\delta^{18}O$ and Sr/Ca we also constructed $\delta^{13}C$ and G/B ratio records in order to examine if the established frequencies can also be recognized in other proxy data. Both records are displayed in the Results, see Figures 4.2 and 4.3.

Although the $\delta^{13}C$ shows some correspondence to the $\delta^{18}O$ record, the correlation between the two is relatively low (R^2=0.15). Primarily the seasonal cycle shows high correspondence between the two records. In Figure 4.2 it can be seen that the $\delta^{13}C$ record shows much more large variations and that the record is not as constant/stable through time as the $\delta^{18}O$ and Sr/Ca records. In the $\delta^{18}O$ and Sr/Ca records we identified some deviating events which are very striking in these records. The $\delta^{13}C$ record also shows some sharp peaks during these events, but beside these events the $\delta^{13}C$ record is composed of many more sharp peaks. In the $\delta^{18}O$ and Sr/Ca records we could also see a gradual trend towards more negative values starting at around 1970 AD. The $\delta^{13}C$ record reveals a similar trend, but much stronger.
To examine whether the $\delta^{13}C$ record show same frequencies as the $\delta^{18}O$ and Sr/Ca records we applied spectral analysis on the $\delta^{13}C$ record. Figure 5.28 shows the REDFIT analysis on the $\delta^{13}C$ curve and Figure 5.29 shows the REDFIT analysis on the yearly $\delta^{13}C$ record. The cycles that can be identified in the $\delta^{13}C$ record have a period of: 46 years, 13.82 years, 1 year and 0.97 year. This matches quite closely with the cycles identified in the $\delta^{18}O$ and Sr/Ca records which had periods of 46, 10.6 and 1 years. The largest difference is present in the length of the period of which is probably the sunspot cycle. It is still possible that the sunspot cycle is present in the $\delta^{13}C$ record and expressed as a 13.82 year cycle, since the period of the sunspot cycle is thought to lie between 9 and 14 years according to literature. The peaks present in the REDFIT analysis of the yearly $\delta^{13}C$ record are all very close to the 95% significance level and thus only relatively weak. The periods of these cycles are 13.80 years, 9.20 years, 7.26 years and 4.31 years. This power spectrum looks quite different than the power spectra of the yearly $\delta^{18}O$ and Sr/Ca records. The periods of $\delta^{18}O$ were 11.50, 9.20 and 3.94 years and of Sr/Ca there was only one cycle visible with a period of 10.62 years. Again the 13.80 years could be the sunspot cycle, the 9.20 year cycle could also be the sunspot cycle or a period of the PDO. The power spectrum of the PDO (Figure 5.9) revealed a period with a length of 9.17 years. The 4.31 year period might reflect ENSO variability.

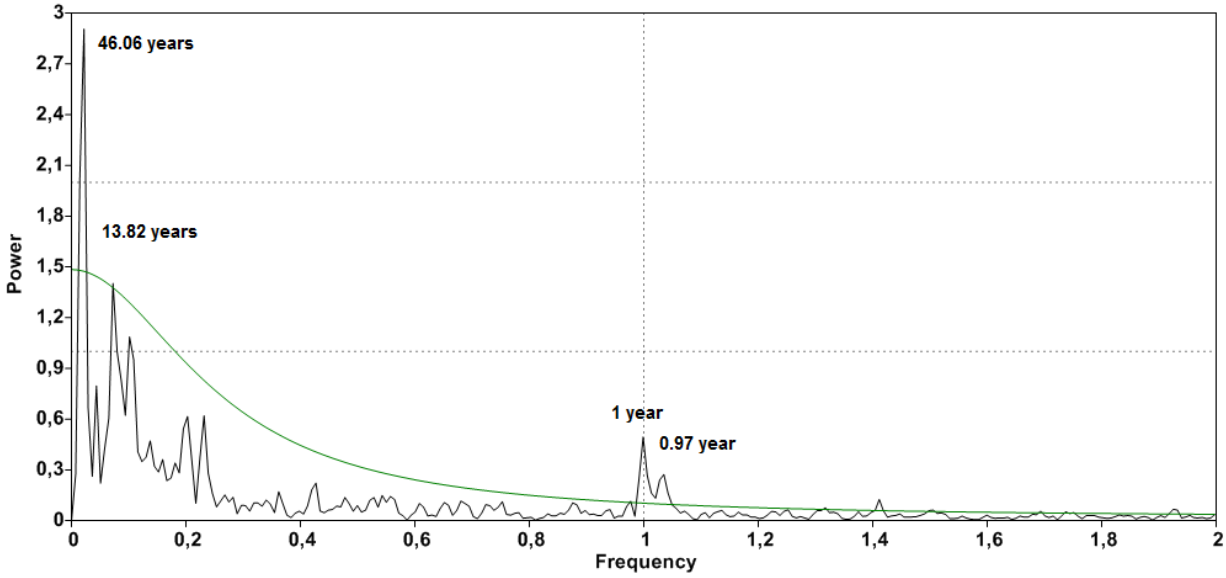

Figure 5.28. Spectral REDFIT analysis of the $\delta^{13}C$ record (not resampled). On the x-axis, the frequency of the cycle is displayed and on the y-axis the power or strength of the cycle is displayed. The green line is the 95% confidence level.

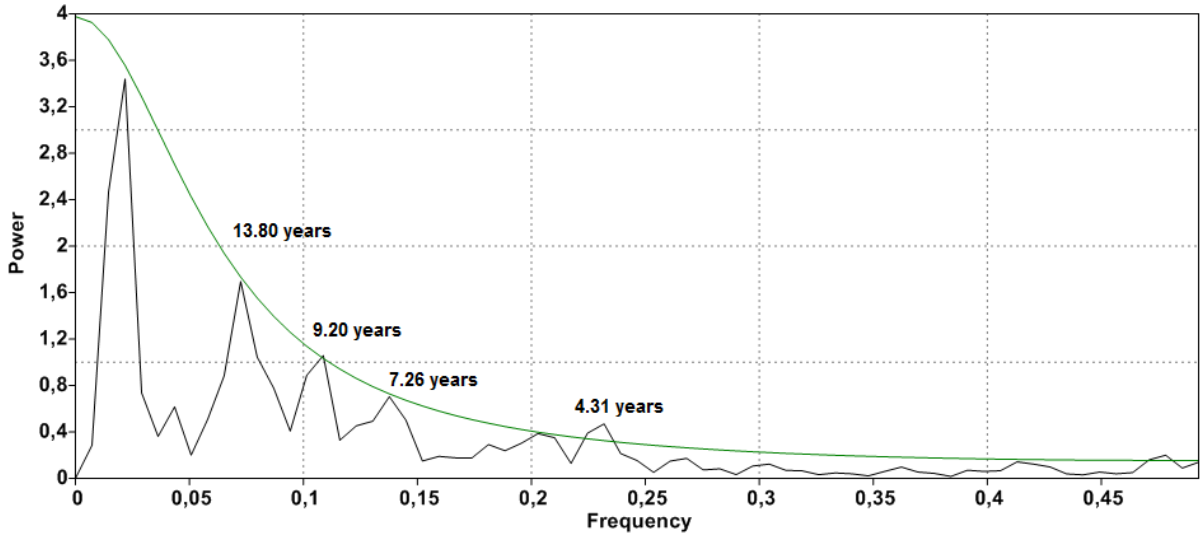

Figure 5.29. Spectral REDFIT analysis of the yearly $\delta^{13}C$ record. On the x-axis, the frequency of the cycle is displayed and on the y-axis the power or strength of the cycle is displayed. The green line is the 95% confidence level.

The differences between the $\delta^{13}C$ and $\delta^{18}O$ and Sr/Ca records and corresponding power spectra are likely caused by the fact that $\delta^{13}C$ recorded in coral tissue is influenced by many factors, while Sr/Ca is only influenced by SST and $\delta^{18}O$ by SST and the $\delta^{18}O$ composition of the seawater. Contrasting, $\delta^{13}C$ of coral aragonite is influenced by the $\delta^{13}C$ composition of the seawater, coral autotrophy (Omata et al., 2008; Reynaud et al., 2007), heterotrophy (Reynaud et al., 2002), riverine DIC (Moyer and Grottoli, 2011) and productivity of the water column.

The G/B ratios show the presence of humic acids, since humic acids have longer wavelengths than the coral aragonite (Grove et al., 2010). The G/B ratio is well correlated to Ba/Ca and is a geochemical coral proxy for sediment runoff and precipitation.
The G/B ratio record is fairly constant over time and only has only one sharp peak towards lower G/B values and a gradual decreasing trend over the whole record from average values of around 0.82

towards around 0.78. We do not have an age model for the G/B ratio record, since the age model constructed for $\delta^{18}O$ and Sr/Ca was based on the calibration of Sr/Ca to an SST record. We only know the position and corresponding age of the first and last sample of the coral core. Since we do not have an age model of the G/B ratio record we cannot do REDFIT spectral analysis. But since the record is relatively very stable and do not show many variations the records seems to have no clear cyclicity. The sharp peak towards lower G/B values in the data record is located around position 159 mm. When we consider the average growth rate of the coral (1.1 cm/year) this peak was occurring roughly around the year 1995. A decrease in G/B values might suggest less rainfall/sediment runoff than compared to the rest of the record. It is strange how a dry time period could create such a sharp event, so possibly there is something changing in the local environment of the atoll. The gradual trend suggest that rainfall/sediment runoff is gradually decreasing through time around Cocos (Keeling) island.

5.8. Limitations and further research

Despite the fact that this research is carried out with maximum precision and care, there are still some limitations and uncertainties present. Uncertainties in the data record originates from measuring errors and the reliability of the constructed age model (during project WOTRO-EKP). Also cumulative errors occur during calculations carried out to determine SST and $\delta^{18}O_{SW}$. Determining the regression coefficient and the next calculations inhibit cumulative error.

Further research on this coral core is recommended. First thing is to extend the $\delta^{18}O$ dataset to the year 1809 AD. Charles Darwin visited Cocos (Keeling) island in one of this expeditions in the 1836 AD, this year can be traced in the complete data record and examined into more detail. A longer dataset also makes it possible to better study present cycles in the data. For example, the uncertainty in the origin of a present 46 year cycle, which could be PDO or it could be resonant frequency from the dataset.
Some research is also required to decrease errors and uncertainties in this record. To identify the robustness of the age model, the age model should be checked by recounting the seasonal layering in the original coral core. It is also good to include another coral core from Cocos (Keeling) island. The coral core Dar 3 is suitable for this purpose, which is taken close to the location of the coral Darwin Long and is smaller in length, but overlaps the Darwin Long core in time. The advantage of multiple cores is that a composite record can be reconstructed to account for inter/intra colony differences. Also more research can be done about the origin of the clear sunspot cycle in this dataset. It is not completely clear how this solar cycle can be so distinctly visible in the data records, and through which processes. Furthermore the origin of the established four events in the Chapter Results can be studied more thoroughly. There is especially a lot uncertainty about the cause triggering and sustaining the event centered around 1965-1970 AD. Also the influence of some systems can be researched into more detail, for example the contribution of the ITF in the region of Cocos (Keeling) island.
The $\delta^{13}C$ and spectral luminescence profile of the coral core Darwin Long can also be studied more thoroughly. For the luminescence data an age model should be constructed, this new age model could be used to check the liability of the established age model.

Chapter 6 Conclusion

Aim of this study was to study the link between SST's, atmospheric convection, precipitation patterns, and cyclones in the eastern Indian Ocean. We expected to recognize ENSO and IOD events in our data and we wanted to study how these two different ocean-atmosphere systems are linked. We used coupled Sr/Ca and $\delta^{18}O$ records in order to construct SST and $\delta^{18}O_{SW}$. The $\delta^{18}O$ record seems to be mainly driven in SST variations and less by salinity changes. Main periodicities found in the data records are a very strong annual seasonal cycle and an eleven year sunspot cycle. Other periodicities found (especially pronounced in the wavelet transforms) have a length of around 46, 20, 7.5 and 5 years. The 46 year period could be resonant frequency or a multidecadal period of the PDO, a longer record is needed to study the origin of this period. The origin of the 20 year period is also uncertain, it could be both an interdecadal oscillation of the PDO (established around 17-28 years; Meehl and Hu, 2006) or an interdecadal period of the sunspot cycle (established around 18-25 years; Cayan and Dettinger, 1997). The 7.5 and 5 year periods that are only weakly pronounced in our data records could be related to ENSO and/or IOD. The 7.5 year period is more likely to be linked to ENSO, since literature established the period of the ENSO to be around 2-7 years (McPhaden et al., 2006), while the period of the IOD is more centered around 2-5 years (Saji et al., 1999). However, ENSO and IOD data from the Cocos region show less clear established periodicities, with especially the IOD being chaotic. The 5 year period can be both explained by ENSO or IOD influences.

Our data contains some very distinct peaks towards more positive values (both in Sr/Ca and in $\delta^{18}O$), these are identified as four events centered around the years: 1883 (1), 1910-1915 (2), 1946 (3) and 1965-1970 AD (4). During these events SST cooled by around 2°C (1, 2 and 3) to around 4°C (4). The main triggers or causes of this events are briefly described below. (1) The 1883 event coincides largely in timing with the volcanic eruption of the Krakatoa (Indonesia). A massive volcanic eruption thought to have influenced global climate. Since Cocos (Keeling) island is located relatively close, it is very likely that this natural disaster influenced local climate, and thus perhaps could have caused this distinct event. (2) The event centered around 1910-1915 AD is likely to be caused by a strong La Niña event simultaneously with a minimum in solar activity, both cooling the eastern Indian Ocean. (3) The 1946 AD event occurs simultaneously with a positive phase of the IOD, cooling the eastern Indian Ocean and a minimum in solar activity. (4) The long lasting event around 1965-1970 AD is the strongest event, but the cause is difficult to discern. Strong influences with periods of around 2-5 years are distinguished which possibly indicate influences of IOD and/or ENSO, although the phases of IOD and ENSO are not exceptionally distinct in this period. At 1965 AD there is also a minimum in solar activity. We also expected to find severe tropical cyclones back in our $\delta^{18}O$ record, but known cyclones did not match with sharp negative excursions in our data record.

Summarizing, climate variability at Cocos (Keeling) island is mainly influenced by annual seasonal variability. Also the eleven year sunspot cycle is thought to be of major influence at our site. The coupled ocean-atmosphere systems ENSO and IOD seem to be of minor influence in this region. Possibly the ENSO and IOD are expressed during only short during events. It is also possible that the PDO influences the climate in the Cocos region, but this should be studied in further research. Also the effect of ocean advection should be studied into more detail. Finally, SST's gradually increase from around 1975 to around 2000 AD. However, a shift in influences of different ocean-atmosphere systems found around the Chagos Archipelago due to crossing of a SST threshold value, is not recognized in the Cocos (Keeling) region.

References

Alibert, C., & McCulloch, M. T. (1997). Strontium/calcium ratios in modern Porites corals from the Great Barrier Reef as a proxy for sea surface temperature: calibration of the thermometer and monitoring of ENSO. Paleoceanography, 12(3), 345-363.

Ash, K.D. and Matyas, C.J. (2010). The influences of ENSO and the subtropical Indian Ocean Dipole on tropical cyclone trajectories in the southwestern Indian Ocean. International journal of climatology, volume 32, 41-56.

Australian Institute of Marine Science. (2015). AIMS – temperature loggers, http://maps.aims.gov.au/index.html?intro=false&z=4&ll=142.91883,-17.51872&l0=aims_aims:AIMS%20-%20Temperature%20Loggers,ea_World_NE2-coast-cities-reefs_Baselayer, accessed (May 6, 2015).

Beck, J.W., Edwards, R.W., Ito, E., Taylor, F.W., Recy, J., Rougerie, F., Joannot, P. and Henin, C. (1992). Sea-surface temperature from coral skeletal Strontium/Calcium ratios. Science. Vol. 257, pp. 644-647.

Bureau of Meteorology, Government of Australia. (2015). About ENSO Outlooks. Retrieved from http://www.bom.gov.au/climate/ahead/about-ENSO-outlooks.shtml, at June 11, 2015.

Bureau of Meteorology, Government of Australia. (2015). Climate statistics for Australian locations, Monthly climate statistics, Cocos Island Airport. Retrieved from http://www.bom.gov.au/climate/averages/tables/cw_200284_All.shtml, at June 26, 2015.

Bureau of Meteorology, Government of Australia. (2015). Tropical Cyclones Affecting the Cocos Islands and Christmas Island. Retrieved from http://www.bom.gov.au/cyclone/history/wa/cocos.shtml, at June 26, 2015.

Cahyarini, S.Y., Pfeiffer, M., Timm, O., Dullo, W-C., Schönberg, D.G. (2008). Reconstructing seawater $\delta^{18}O$ from paired coral $\delta^{18}O$ and Sr/Ca ratios: Methods, error analysis and problems, with examples from Tahiti (French Polynesia) and Timor (Indonesia). Geochimica et Cosmochimica Acta. Vol. 72, pp. 2841-2853.

Cane, M. A. (2005). The evolution of El Niño, past and future. Earth and Planetary Science Letters, 230(3), 227-240.

Cayan, D. R., & Dettinger, M. D. (1997). Response of global upper ocean temperature to changing solar irradiance. Journal of Geophysical Research, 102(C2), 3255-3266.

Corrège, T. (2006). Sea surface temperature and salinity reconstruction from coral geochemical tracers. Palaeogeography, Palaeoclimatology, Palaeoecology. Vol, 232, pp. 408-428.

Deser, C., Phillips, A. S., & Hurrell, J. W. (2004). Pacific interdecadal climate variability: Linkages between the tropics and the North Pacific during boreal winter since 1900. Journal of Climate, 17(16), 3109-3124.

Dole, M. (1956). The oxygen isotope cycle in nature, Nat. Acad. Sci. Nat. Res. Counc. Publ. 400, 13-19. Cited by Weber & Woodhead (1972).

Epstein, S., Buchsbaum, R., Lowenstam, H.A. and Urey, H.C. (1951). Carbonate-water isotopic temperature scale. Bulletin of the geological society of America. Vol. 62, pp. 417-426.

Epstein, S., Buchsbaum, R., Lowenstam, H.A. and Urey, H.C. (1953). Revised carbonate-water isotopic temperature scale. Bulletin of the geological society of America. Vol. 64, pp. 1315-1326.

Fairbanks, R.G., Evans, M.N., Rubenstone, J.L., Mortlock, R.A., Broad, K., Moore, M.D. and Charles, C.D. (1997). Evaluating climate indices and their geochemical proxies measured in corals. Coral Reefs. Vol. 16, Suppl. S93-S100.

Gleckler, P. J., Wigley, T. M. L., Santer, B. D., Gregory, J. M., AchutaRao, K., & Taylor, K. E. (2006). Volcanoes and climate: Krakatoa's signature persists in the ocean. Nature, 439(7077), 675-675.

Good, S. A., M. J. Martin and N. A. Rayner, (2013). EN4: quality controlled ocean temperature and salinity profiles and monthly objective analyses with uncertainty estimates, Journal of Geophysical Research: Oceans, 118, 6704-6716.

Graham, N., and Barnett, T.P., (1987). Sea surface temperature, surface wind divergence, and convection over tropical oceans. Science, v. 238, p. 657–659.

Grossman, E. L., & Ku, T. L. (1986). Oxygen and carbon isotope fractionation in biogenic aragonite: temperature effects. Chemical Geology: Isotope Geoscience section, 59, 59-74.

Grove, C. A. (2012). Madagascar s climate history unlocked by giant corals. Doctoral theses, Vrije Universiteit Amsterdam.

Grove, C. A., Nagtegaal, R., Zinke, J., Scheufen, T., Koster, B., Kasper, S., ... & Brummer, G. J. A. (2010). River runoff reconstructions from novel spectral luminescence scanning of massive coral skeletons. Coral Reefs, 29(3), 579-591.

Hammer, Ø., Harper, D. A. T., & Ryan, P. D. (2001). PAST-Palaeontological statistics. www.uv.es/~ pardomv/pe/2001_1/past/pastprog/past. pdf, accessed on July 25, 2009.

IPCC (2013) Climate Change 2013: The physical science basis. Contribution of Working Group I to the Fifth Assessment Report of the Intergovernmental Panel on Climate Change.

Juillet-Leclerc, A., & Schmidt, G. (2001). A calibration of the oxygen isotope paleothermometer of coral aragonite from Porites. Geophysical research letters, 28(21), 4135-4138.

KNMI Climate Explorer. (2015). Monthly Cocos island A.M.O. GHCN v2 precipitation (all). http://climexp.knmi.nl, accessed June 10, 2015.

KNMI Climate Explorer. (2015). Monthly DMI ERSST. http://climexp.knmi.nl, accessed May 19, 2015.

KNMI Climate Explorer. (2015). Monthly EN4 SSS 95-97E/-13—11N Index. Met Office Hadley Centre observations. Good, S. A., M. J. Martin and N. A. Rayner, 2013. EN4: quality controlled ocean temperature and salinity profiles and monthly objective analyses with uncertainty estimates, Journal of Geophysical Research: Oceans, 118, 6704-6716. http://climexp.knmi.nl, accessed May 26, 2015.

KNMI Climate Explorer. (2015). NCDC Extended Reconstructed SST 1854-2015, v3b. http://climexp.knmi.nl, accessed May 13, 2015.

KNMI Climate Explorer. (2015). Monthly Cocos island GHCN v3 mean temperature. http://climexp.knmi.nl, accessed June 30, 2015.

KNMI Climate Explorer. (2015). Monthly Nino3.4. http://climexp.knmi.nl, accessed May 19, 2015.

KNMI Climate Explorer. (2015). Monthly reconstructed solar constant. Lean (2000) and Wang et al. (2005). http://climexp.knmi.nl, accessed July 9, 2015.

Krishnan, R., & Sugi, M. (2003). Pacific decadal oscillation and variability of the Indian summer monsoon rainfall. Climate Dynamics, 21(3-4), 233-242.

Lean, J. (2000). Evolution of the Sun's spectral irradiance since the Maunder Minimum. Geophysical Research Letters, 27(16), 2425-2428.

Mantua, N. J., Hare, S. R., Zhang, Y., Wallace, J. M., & Francis, R. C. (1997). A Pacific interdecadal climate oscillation with impacts on salmon production. Bulletin of the american Meteorological Society, 78(6), 1069-1079.

McConnaughey, T. (1989). 13C and 18O isotopic disequilibrium in biological carbonates: I. Patterns. Geochimica et Cosmochimica Acta. Vol. 53, pp. 151-162.

McPhaden, M. J., Zebiak, S. E., & Glantz, M. H. (2006). ENSO as an integrating concept in earth science. Science, 314(5806), 1740-1745.

Meehl, G. A., & Hu, A. (2006). Megadroughts in the Indian monsoon region and southwest North America and a mechanism for associated multidecadal Pacific sea surface temperature anomalies. Journal of Climate, 19(9), 1605-1623.

Meyers, G., McIntosh, P., Pigot, L., & Pook, M. (2007). The years of El Niño, La Niña, and interactions with the tropical Indian Ocean. Journal of Climate, 20(13), 2872-2880.

Minobe, S. (1997). A 50-70 year climatic oscillation over the North Pacific and North America. Geophysical Research Letters, 24(6), 683-686.

Moreau, M., Corrège, T., Dassié, E.P. and Le Cornec, F. (2015). Evidence of the non-influence of salinity variability on the *Porites* coral Sr/Ca palaeothermometer. Climate of the Past. Vol. 11, pp. 523-532.

Moyer, R. P., & Grottoli, A. G. (2011). Coral skeletal carbon isotopes (δ13C and Δ14C) record the delivery of terrestrial carbon to the coastal waters of Puerto Rico. Coral Reefs, 30(3), 791-802.

Muller-Parker, G., & D'Elia, C. F. (1997). Interactions between corals and their symbiotic algae. Life and death of coral reefs, 96-113.

Nagura, M., & Konda, M. (2007). The seasonal development of an SST anomaly in the Indian Ocean and its relationship to ENSO. Journal of climate, 20(1), 38-52.

National Ocean Service (NOS). (revised: April 9, 2015). Corals. Zooxanthellae…What's that. National Oceanic and Atmospheric Administration (NOAA), United States department of commerce. Retrieved

from http://oceanservice.noaa.gov/education/tutorial_corals/coral02_zooxanthellae.html, on April 14, 2015.

Nurhati, I. S., Cobb, K. M., Charles, C. D., & Dunbar, R. B. (2009). Late 20th century warming and freshening in the central tropical Pacific. Geophysical Research Letters, 36(21).

Nurhati, I.S., Cobb, K.M. and Di Lorenzo, E. (2011). Decadal-scale SST and salinity variations in the central tropical Pacific: signatures of natural and anthropogenic climate change. Journal of Climate, vol. 24, pp.3294-3308.

Omata, T., Suzuki, A., Sato, T., Minoshima, K., Nomaru, E., Murakami, A., Murayama, S., Kawahata, H., Maruyama, T. (2008). Effect of photosynthetic light dosage on carbon isotope composition in the coral skeleton: Long-term culture of Porites spp. Journal of Geophysical Research: Biogeosciences (2005–2012), 113(G2).

Paillard, D., Labeyrie, L., & Yiou, P. (1996). Macintosh program performs time-series analysis. Eos, Transactions American Geophysical Union, 77(39), 379-379.

Pfeiffer, M., Timm, O., Dullo, W. C., & Garbe-Schönberg, D. (2006). Paired coral Sr/Ca and δ18O records from the Chagos Archipelago: Late twentieth century warming affects rainfall variability in the tropical Indian Ocean. Geology, 34(12), 1069-1072.

Rampino, M. R., & Self, S. (1982). Historic eruptions of Tambora (1815), Krakatau (1883), and Agung (1963), their stratospheric aerosols, and climatic impact. Quaternary Research, 18(2), 127-143.

Ren, L., Linsley, B.K., Wellington, G.M., Schrag, D.P. and Hoegh-guldberg, O. (2002). Deconvolving the δ18O seawater component from subseasonal coral δ18O and Sr/Ca at Rarotonga in the southwestern subtropical Pacific for the period 1726 to 1997. Geochimica et Cosmochimica Acta. Vol. 67, Issue 9, pp. 1609-1621.

Reynaud, S., Ferrier-Pagès, C., Meibom, A., Mostefaoui, S., Mortlock, R., Fairbanks, R., & Allemand, D. (2007). Light and temperature effects on Sr/Ca and Mg/Ca ratios in the scleractinian coral Acropora sp. Geochimica et Cosmochimica Acta, 71(2), 354-362.

Reynaud, S., Ferrier-Pages, C., Sambrotto, R., Juillet-Leclerc, A., Jaubert, J., & Gattuso, J. P. (2002). Effect of feeding on the carbon and oxygen isotopic composition in the tissues and skeleton of the zooxanthellate coral Stylophora pistillata. Marine Ecology Progress Series, 238, 81-89.

Saji, N. H., Goswami, B. N., Vinayachandran, P. N., & Yamagata, T. (1999). A dipole mode in the tropical Indian Ocean. Nature, 401(6751), 360-363.

Saji, N. H., & Yamagata, T. (2003). Possible impacts of Indian Ocean dipole mode events on global climate. Climate Research, 25(2), 151-169.

Schott, F. A., Xie, S. P., & McCreary, J. P. (2009). Indian Ocean circulation and climate variability. Reviews of Geophysics, 47(1).

Schulz, M., & Mudelsee, M. (2002). REDFIT: estimating red-noise spectra directly from unevenly spaced paleoclimatic time series. Computers & Geosciences, 28(3), 421-426.

Sebille, E., Sprintall, J., Schwarzkopf, F. U., Sen Gupta, A., Santoso, A., England, M. H., ... & Böning, C. W. (2014). Pacific-to-Indian Ocean connectivity: Tasman leakage, Indonesian Throughflow, and the role of ENSO. Journal of Geophysical Research: Oceans, 119(2), 1365-1382.

Smits, T.M. and Reynolds, R.W. (2004). Improved Extended Reconstruction of SST (1854-1997). Journal of climate. Vol. 17, pp. 2466-2477.

Solow, A.R. and Huppert, A. (2004). A potential bias in coral reconstruction of sea surface temperature. Geophysical Research Letters. Vol. 31.

Sud, Y., Walker, G., and Lau, K., (1999). Mechanisms regulating sea-surface temperatures and deep convection in the tropics: Geophysical Research Letters, v. 26, p. 1019–1022.

Suzuki, A., Hibino, K., Iwase, A. and Kawahata, H. (2005). Intercolony variability of skeletal oxygen and carbon isotope signatures of cultured *Porites* corals: Temperature-controlled experiments. Geochimica et Cosmochimica Acta. Vol. 69, No. 18, pp. 4453-4462.

Vecchi, G. A., & Soden, B. J. (2007). Global warming and the weakening of the tropical circulation. Journal of Climate, 20(17), 4316-4340.

Wang, Y. M., Lean, J. L., & Sheeley Jr, N. R. (2005). Modeling the sun's magnetic field and irradiance since 1713. The Astrophysical Journal, 625(1), 522.

Weber, J.N. and Woodhead, P.M.J. (1970). Carbon and oxygen isotope fractionation in the skeletal carbonate of reef-building corals. Chemical Geology. Vol. 6, pp. 93-117.

Weber, J.N. and Woodhead, P.M.J. (1972). Temperature dependence of oxygen-18 concentration in reef coral carbonates. Journal of geophysical research. Vol. 77, NO. 3, pp. 463-473.

Wellington, G.M., Dunbar, R.B. and Merlen, G. (1996). Calibration of stable isotope signatures in Galápagos corals. Paleoceanography. Vol. 11, pp. 467-480.

Xie, S.P., Annamalai, H., Schott, F. A., & McCreary Jr, J. P. (2002). Structure and mechanisms of south Indian Ocean climate variability*. Journal of Climate, 15(8), 864-878.

Zhang, C., (1993). Large-scale variability of deep convection in relation to sea surface temperature in the tropics: Journal of Climate, v. 6, p. 1898–1913.

Zhang, Y., Wallace, J. M., & Battisti, D. S. (1997). ENSO-like interdecadal variability: 1900-93. Journal of climate, 10(5), 1004-1020.

Zinke, J., Dullo, W. C., Heiss, G. A., & Eisenhauer, A. (2004). ENSO and Indian Ocean subtropical dipole variability is recorded in a coral record off southwest Madagascar for the period 1659 to 1995. Earth and Planetary Science Letters, 228(1), 177-194.

Acknowledgement

I would like to thank everybody from the GCO department at the NIOZ, Texel. I enjoyed my time working at the NIOZ research institute and the working atmosphere in the department was really nice. In addition I would like to thank some people who helped me with the research for this thesis.
My supervisors, Prof. Gert-Jan Reichart and Dr. Rick Hennekam, who helped me very good and were always accessible for advice and feedback. Prof. Geert-Jan Brummer who was always willing to help and special thanks for drilling this beautiful core. Dr. Jens Zinke, the coral specialist, who was always very willing to help with anything considering this research, especially the help considering the calculations was very valuable. And last but not least, Piet van Gaever, who helped me with the stable oxygen isotope measurements using the Mat Kiel device.

Appendix 1

High resolution photograph of coral core Darwin Long

The 1.94 m long Darwin Long coral core. The left image is the most recent part of the coral, right image can be placed visually beneath the left picture. Left image consists of the coral fragments numbers 1-7 and right image consists of coral fragments 6-11, so the images overlap.

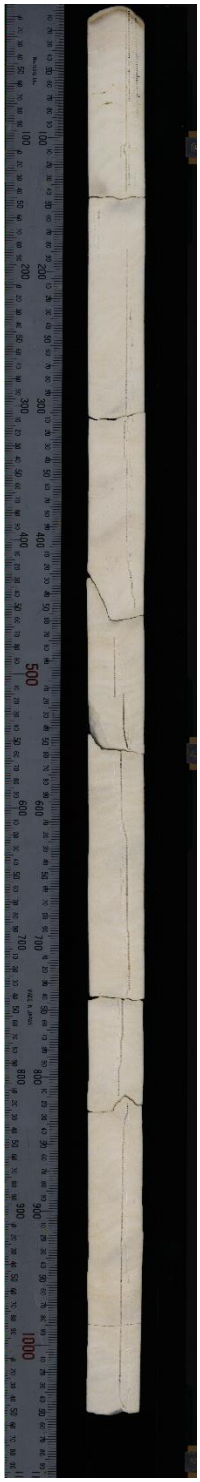

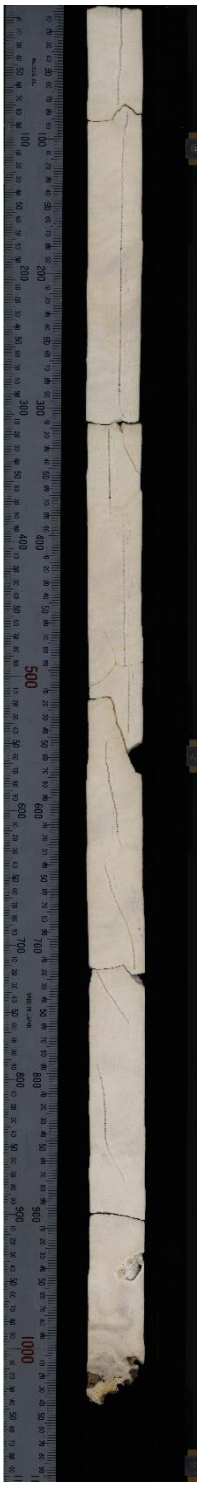

Appendix 2

X-Ray of coral core Darwin Long

The numbers indicate the different drilling fragments of the coral core Darwin Long. Number one is the top layer of the coral and therefore the most recent part of the coral. The X-Ray images are taken with 50 Kv and exposed for 10 seconds.

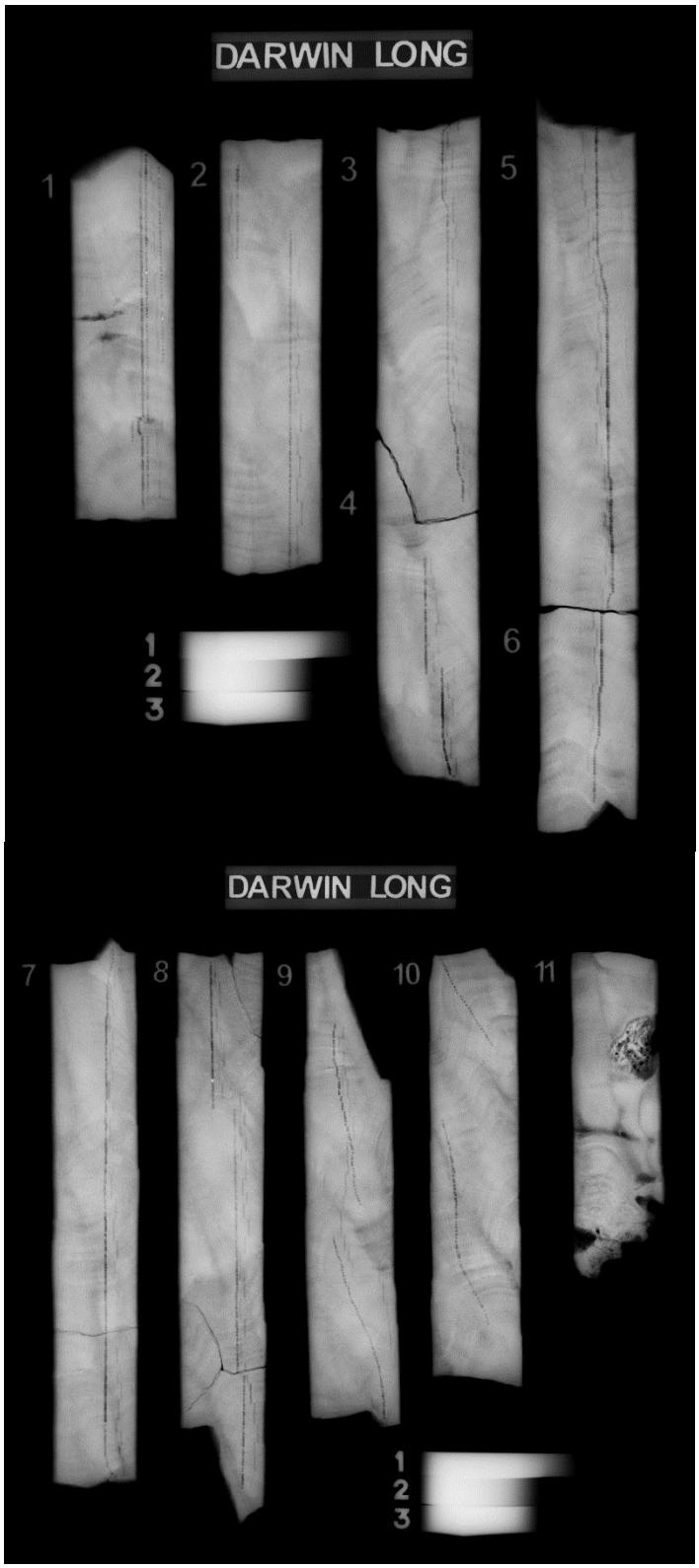

Appendix 3

UV luminescence image of coral core Darwin Long

UV luminescence image of Darwin Long from SLS using the Avaatech core-scanner. The left image is the most recent part of the coral, right image can be placed visually beneath the left picture. Left image consists of the coral fragments numbers 1-7 and right image consists of coral fragments 6-11, so the images overlap.